SANDIA REPORT

SAND2005-3216
Unlimited Release
Printed July 2005

Three Dimensional Simulation for Big Hill Strategic Petroleum Reserve (SPR)

Byoung-Yoon Park, Brian L. Ehgartner, Moo Y Lee, and Steven R. Sobolik

Prepared by Sandia National Laboratories
Albuquerque, New Mexico 87185 and Livermore, California 94550

Sandia is a multiprogram laboratory operated by Sandia Corporation,
a Lockheed Martin Company, for the United States Department of Energy's
National Nuclear Security Administration under Contract DE-AC04-94AL85000.

Issued by Sandia National Laboratories, operated for the United States Department of Energy by Sandia Corporation.

Available to DOE and DOE contractors from
U.S. Department of Energy
Office of Scientific and Technical Information
P.O. Box 62
Oak Ridge, TN 37831

Telephone: (865)576-8401
Facsimile: (865)576-5728
E-Mail: reports@adonis.osti.gov
Online ordering: http://www.osti.gov/bridge

Available to the public from
U.S. Department of Commerce
National Technical Information Service
5285 Port Royal Rd
Springfield, VA 22161

Telephone: (800)553-6847
Facsimile: (703)605-6900
E-Mail: orders@ntis.fedworld.gov
Online order: http://www.ntis.gov/help/ordermethods.asp?loc=7-4-0#online

SAND2005-3216
Unlimited Release
Printed July 2005

Three Dimensional Simulation for Big Hill Strategic Petroleum Reserve (SPR)

Byoung-Yoon Park[1], Brian L. Ehgartner[2], Moo Y. Lee[3], and Steven R. Sobolik[3]

[1]-Performance Assessment & Decision Analysis Department
Sandia National Laboratories
P.O. Box 5800
Albuquerque, NM 87185-1395

[2]-Geotechnology and Engineering Department
Sandia National Laboratories
P.O. Box 5800
Albuquerque, NM 87185-0706

[3]-Geomechanics Department
Sandia National Laboratories
P.O. Box 5800
Albuquerque, NM 87185-0751

Abstract

3-D finite element analyses were performed to evaluate the structural integrity of caverns located at the Strategic Petroleum Reserve's Big Hill site. State-of-art analyses simulated the current site configuration and considered additional caverns. The addition of 5 caverns to account for a full site and a full dome containing 31 caverns were modeled. Operations including both normal and cavern workover pressures and cavern enlargement due to leaching were modeled to account for as many as 5 future oil drawdowns. Under the modeled conditions, caverns were placed very close to the edge of the salt dome. The web of salt separating the caverns and the web of salt between the caverns and edge of the salt dome were reduced due to leaching. The impacts on cavern stability, underground creep closure, surface subsidence and infrastructure, and well integrity were quantified. The analyses included recently derived damage criterion obtained from testing of Big Hill salt cores. The results show that from a structural view point, many additional caverns can be safely added to Big Hill.

Intentionally blank

Acknowledgements

This research is funded by the SPR program administered by the U.S. Department of Energy. The authors would like to acknowledge the valuable contributions to this work provided by Courtney Herrick (SNL, Dept. 6822), David Kessel (SNL, Dept. 6820). Darrell Munson (SNL, Dept. 6113) helped us understand the elastic modulus reduction factor used in West Hackberry analyses.

Sandia is a multiprogram laboratory operated by Sandia Corporation, a Lockheed Martin Company, for the United States Department of Energy under Contract DE-AC04-94Al85000

Intentionally Blank

TABLE OF CONTENTS

LIST OF TABLES

LIST OF FIGURES

ACRONYMS

BH	Big Hill
DOE	U.S. Department of Energy
DILFAC	DILatant damage FACtor
FEM	Finite Element Method
RF	elastic modulus Reduction Factor
SD	Standoff Distance
SMF	Structural Multiplication Factor
SNL	Sandia National Laboratories
SPR	Strategic Petroleum Reserve
TMF	Thermal constant Multiplication Factor
WIPP	Waste Isolation Pilot Plant
WH	West Hackberry

Intentionally Blank

1 INTRODUCTION

1.1 Objective

Solution-mined caverns in salt have provided a means to safely store liquid and gas hydrocarbons over the past 60+ years. In the Gulf Coast, salt domes have become excellent hosts for numerous caverns due to their geologic properties. Over time, the number and size of caverns have progressively increased as there is no means of removing a cavern once it is constructed. Prime real estate locations, typically directly above the central parts of a dome, have been utilized. To develop new caverns, companies are increasingly turning toward marginal locations near the flank of the domes where geologic uncertainty increases. Thus the sizes of cavern fields have expanded towards the edge of dome. This report attempts to model these conditions and addresses the resulting performance and stability issues.

1.2 Background

The US Strategic Petroleum Reserve (SPR) stores crude oil in 62 caverns located at 4 different sites in Texas and Louisiana (Figure 1). The reserve is approaching its capacity of 700 million barrels and is expected to be full by the end of 2005. If authorized, additional capacity will require new caverns. A prime candidate for expansion is the Big Hill (BH) site.

Potential cavern locations at BH have already been identified by Magorian and Neal (1988). It was reported that space for five caverns might exist adjacent to the 14 present locations along the western and southern periphery of the dome and that additional cavern space along the western and southern boundaries cannot be ruled out until further exploration is completed. Other space is available to the north (outside the DOE property boundary), and probably has better potential for expansion. Although modeling by Stein and Rautman (2004) shows the northern edge of the dome to be much less constrained (fewer data points to indicate where the salt is) than the southern portion, both the original site characterizations report (Hart et al., 1981) and its most recent update, which includes a high resolution seismic survey (Neal and Magorian, 1993), suggest that the site is geologically superior for SPR cavern development.

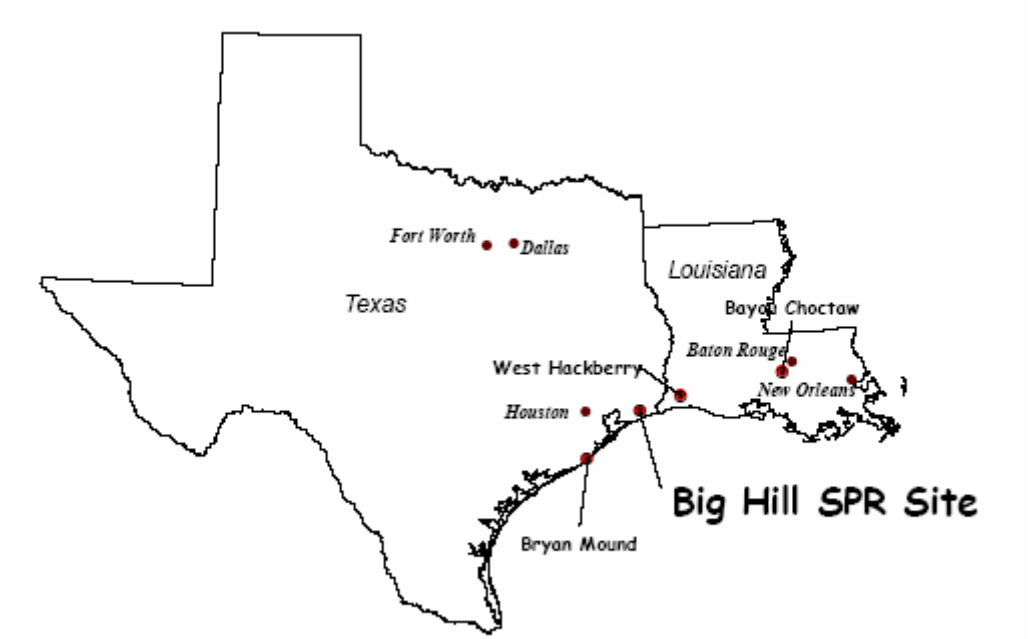

Figure 1: Location of SPR Sites.

1.3 Report Organization

The remainder of this report describes implementation details. Section 2 introduces the Big Hill site description. Section 3 presents an overview of the stratigraphy for modeling, and cavern model including model history and the thermal condition. Section 4 provides the descretized finite-element mesh for 19 cavern array considering 5 leaching. Section 5 presents back-fitting analysis to determine the unmeasured parameters by calibrating those to best match the field data. Section 6 provided the failure criteria for checking the structural stability of salt dome and allowable strains for wells and surface structures. Section 7 lists the computer codes used for this study, including the finite element code, JAS3D. Section 8 describes the results such as cavern deformation, storage loss with time, subsidence, the integrity of cavern wells, checking the cavern stability by dilatant damage criteria and tensile failure criterion, and so on. Section 9 describes the standoff distance effect to estimate how many more caverns can be constructed in the existing salt dome. 31-cavern model is constructed for this study. Finally, Section 10 provides the discussion and concluding remarks.

2 SITE DESCRIPTION

Figure 2 shows a plan view of the BH site with contour lines defining the approximate location of the salt dome's edge. The current 14 cavern (101-114) and five potential expansion cavern (X1-5) locations are included. The figure also shows the undeveloped area north of the DOE property line (Sabine Pass Terminal).

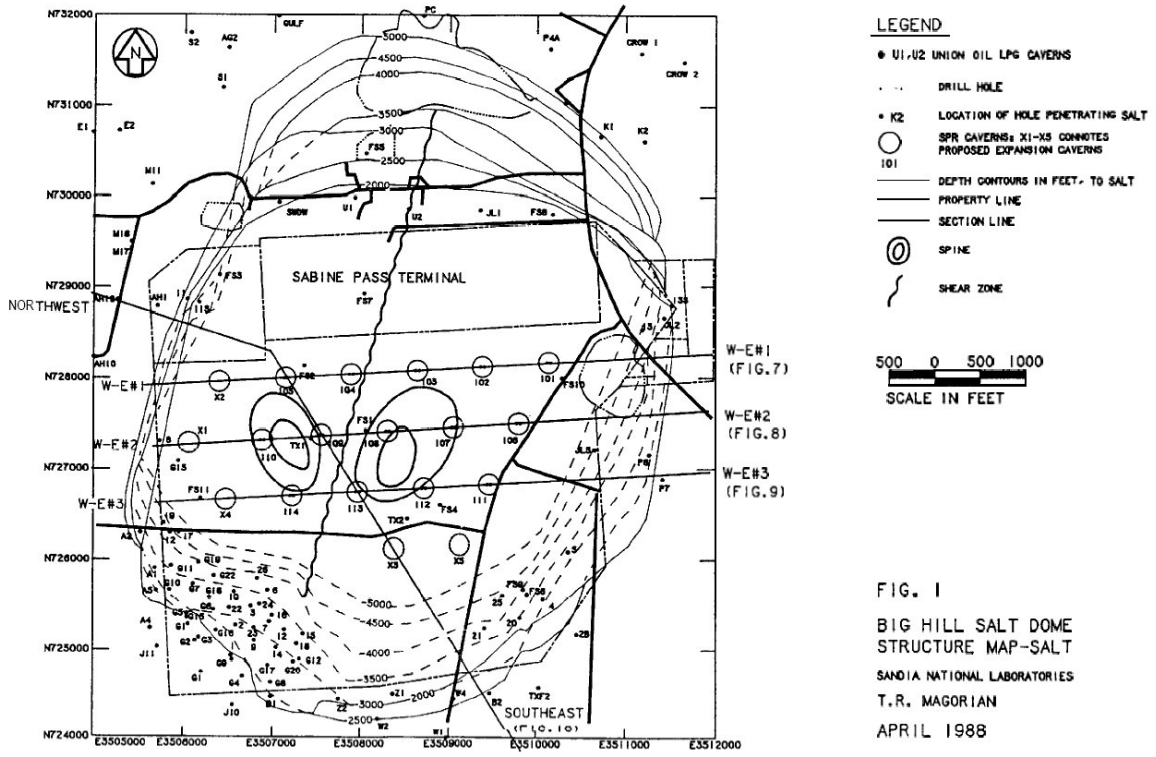

Figure 2: Big Hill site plan view (Magorian and Neal, 1988)

A West-East cross-section #1 through the northern-most row of caverns (Cavern 101-105) provides a geologic representation near the middle of the dome (Figure 3). The site has an exceptionally thick caprock comprised of two layers and faulting occurs in the region. The upper caprock is made of gypsum and limestone, whereas the lower caprock is made of anhydrite. A major fault extends North-South running along the entire distance of the caprock for an unknown distance into the salt. This has a pronounced effect on the subsidence measured above the site and is a consideration for future cavern placement (Ehgartner and Bauer, 2004). Figure 4 shows three dimensional representation of the BH salt dome constructed by digitally sewing together the separate models of the flank and top of salt. Figure 5 and Figure 6 show the salt dome with caprock as viewed from the northeast and southwest, respectively (Rautman et al, 2005).

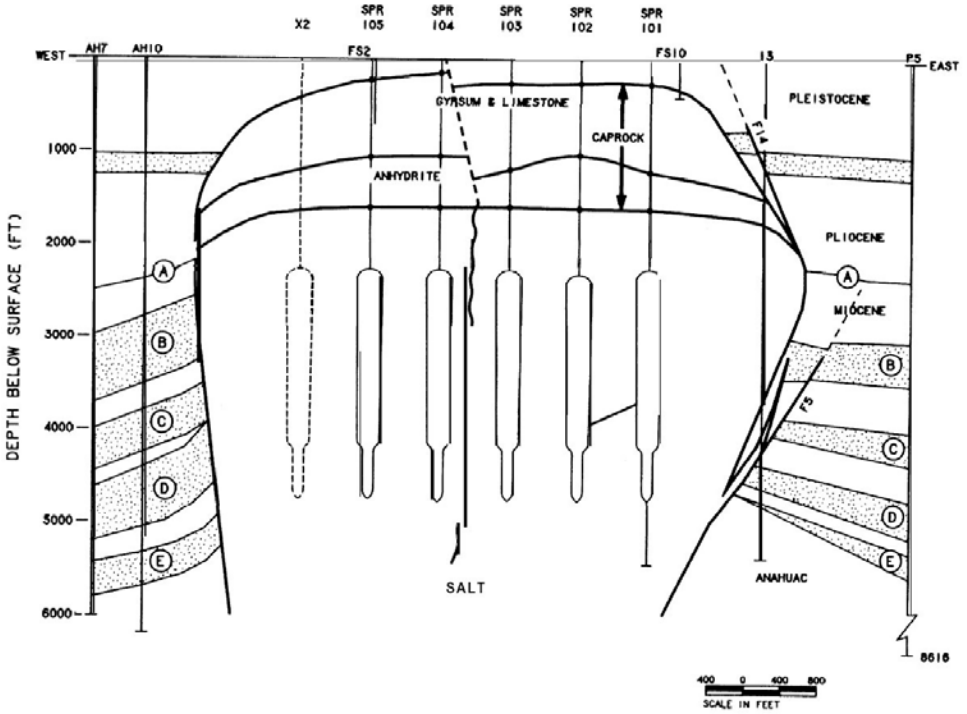

Figure 3: Cross-Section (West-East #1) Near Middle of Dome (Magorian and Neal, 1988)

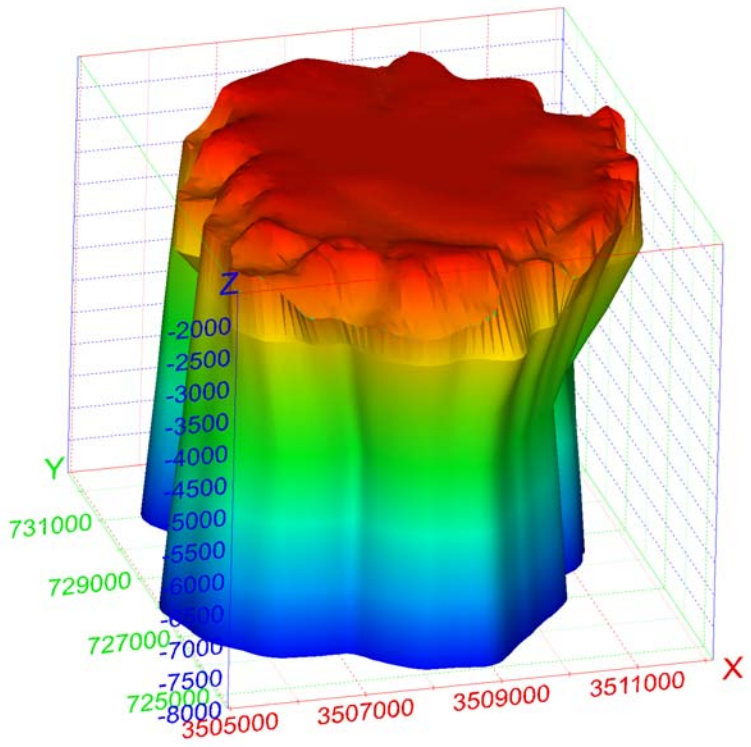

Figure 4: Three dimensional representation of the Big Hill salt dome (Rautman et al, 2005).

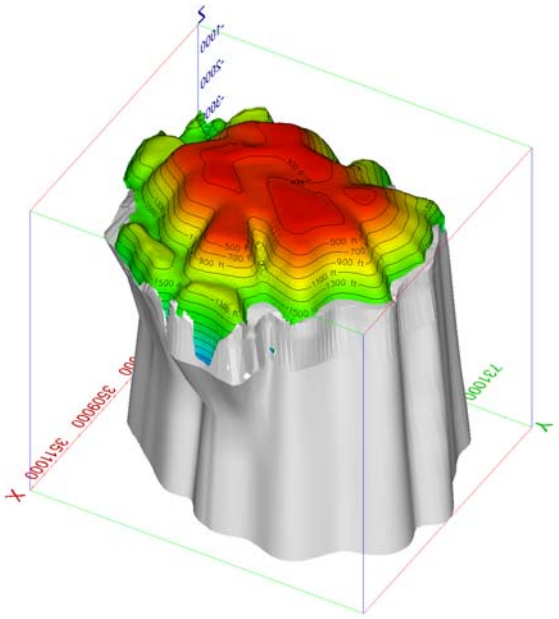

Figure 5: View of the caprock colored by elevation shown with the salt dome (grey). View is from the northeast at an elevation of 40º from the horizontal (Rautman et al, 2005).

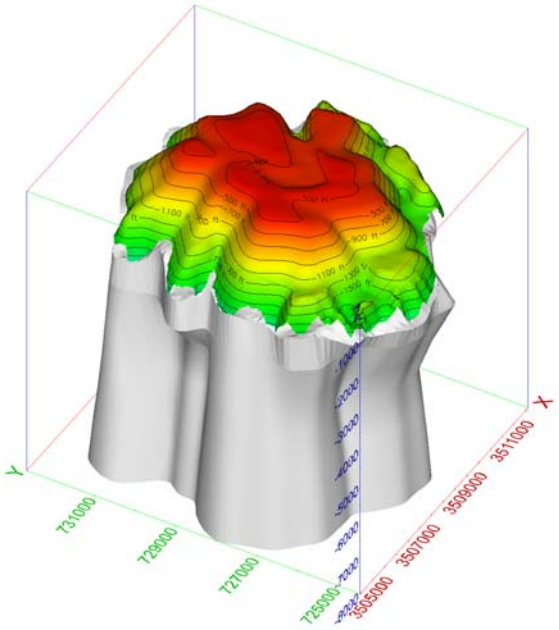

Figure 6: View of the caprock colored by elevation shown with the salt dome (grey). View is from the southwest at an elevation of 40º from the horizontal (Rautman et al, 2005).

3 ANALYSIS MODEL

3.1 Geomechanical Model

3.1.1 Stratigraphy

Two layers of caprock exist over the BH salt dome. The upper caprock, consisting of gypsum and limestone, is 900 ft thick. The lower caprock, consisting of anhydrite is 400 ft thick. The top layer of overburden, which consists of sand and soil, has a thickness of 300 ft. The salt thickness over the caverns is approximately 700 ft. The stratigraphy near the BH salt dome is shown in Figure 7.

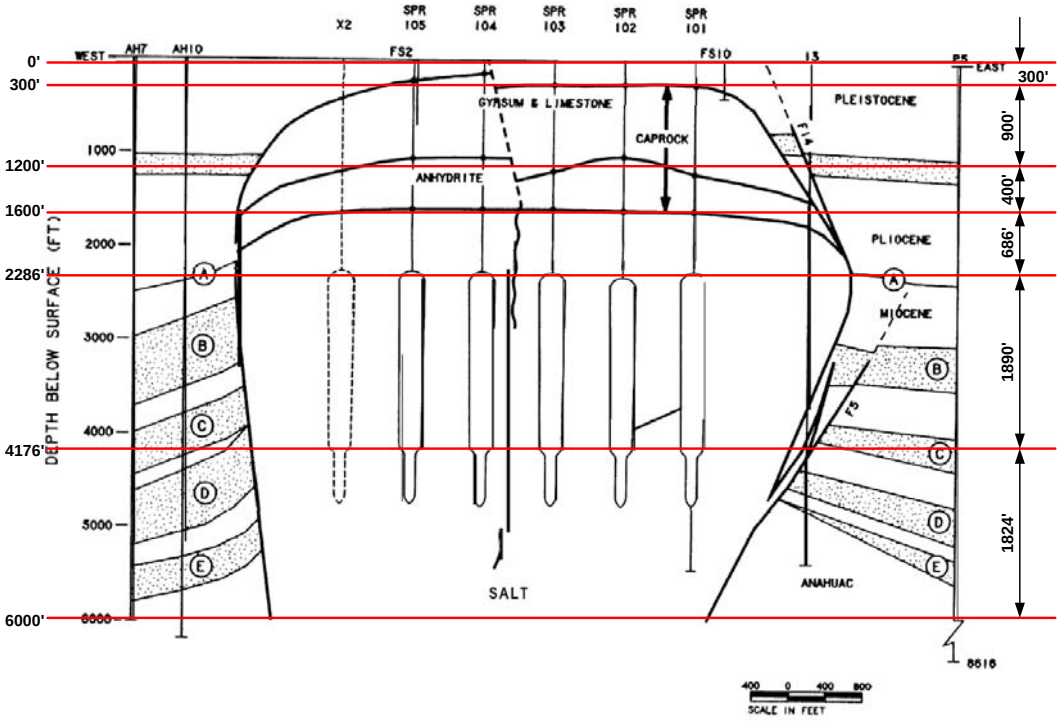

Figure 7: Stratigraphy near the BH salt dome and the thickness of each layer used for modeling

3.1.2 Salt constitutive model

The geomechanical properties for BH salt are not entirely known for modeling. Data for the creep constant, the stress exponent, and the thermal constant for the power law creep model do not exist. Where needed, data from the West Hackberry (WH) site are used because both BH and WH salt are classified as soft salts (Munson, 1998). WH salt data were derived through mechanical property testing of salt cores collected from boreholes (Wawersik and Zeuch, 1984). The creep constitutive model considered only secondary or steady-sate creep. The creep strain rate is determined from the effective stress as follows:

$$\dot{\varepsilon} = A\left(\frac{\sigma}{\mu}\right)^{n} \exp\left(-\frac{Q}{RT}\right) \quad (1)$$

where, $\dot{\varepsilon}$ = creep strain rate,
σ = effective or von Mises stress,
μ = shear modulus, E/2(1+ν),
T = absolute temperature,
A, n = constants determined from fitting the model to creep data,
Q = effective activation energy,
R = universal gas constant.

The elastic and creep constants measured at the WIPP (Waste Isolation Pilot Plant) and WH site are given in Table 1. The properties assume a homogeneous material. The elastic modulus was reduced from the value measured in the laboratory to account for large scale discontinuities and fracturing of the caprocks (Preece and Foley, 1984). Using a reduced modulus has been shown to simulate the transient response of salt around underground excavations (Morgan and Krieg, 1990). The elastic modulus reduction factor (RF) is known to vary for salts (Munson, 1998). Limited creep testing of SPR salts (Wawersik and Zeuch, 1984) showed considerable variability in creep rates (up to an order of magnitude difference). Therefore, the RF and the secondary constants of salt will be determined by calibrating those to best match the measured closure and subsidence rates at BH site through back-fitting analyses. Details are provided in Section 5.

Table 1: Material properties of halite measured at the WIPP and WH site

Parameters		Units	Values	Site	References
Density (ρ)		kg/m^3	2300	WIPP	Krieg, 1984
Young's Modulus (E)		GPa	31.0	WIPP	Krieg, 1984
Poisson's Ratio (ν)		-	0.25	WIPP	Krieg, 1984
Bulk Modulus (K)		GPa	20.7	WIPP	Krieg, 1984
Shear Modulus (μ)		GPa	12.4	WIPP	Krieg, 1984
Secondary Constants	Creep Constant (A)	$Pa^{-4.9}/s$	5.79×10^{-36}	WIPP	Krieg, 1984
	Stress Exponent (n)		4.9	WH	Wawersik and Zeuch, 1984
	Thermal Constant (Q)	Kcal/mol	12.0	WH	Wawersik and Zeuch, 1984

3.1.3 Anhydrite constitutive model

The anhydrite in the lower caprock layer is expected to experience inelastic material behavior. The anhydrite layer is considered isotropic and elastic until yield occurs (Butcher, 1997). However, the material properties of the BH anhydrite were not investigated. So, the behavior of the BH anhydrite is assumed to be the same as the WIPP anhydrite. Once the yield stress is reached, plastic strain begins to accumulate. Yield is assumed to be governed by the Drucker-Prager criterion:

$$\sqrt{J_2} = C - aI_1 \tag{2}$$

where $J_2 =$ the second deviatoric stress invariant

$I_1 =$ the first stress invariant (σ_{kk})

A non-associative flow rule is used to determine the plastic strain components. Drucker-Prager constants, *C* and *a*, for the anhydrite are given in Table 2.

Table 2: Drucker-Prager constants for anhydrite (Butcher, 1997)

Parameters	Units	Values
C	MPa	1.35
a		0.45

The input to the soil and crushable foam model in the JAS3D code requires the analyst to provide TWO MU, 2μ, and the BULK MODULUS, *K*. The conversion from Young's modulus, *E*, and Poisson's ratio, ν, to the JAS3D input parameters is given by the following relationships taken from Fung (1965):

$$2\mu = \frac{E}{(1+\nu)} \tag{3}$$

$$K = \frac{E}{3(1-2\nu)} \tag{4}$$

The JAS3D code requires the input to the material model which describes the anhydrite's nonlinear response to be given in terms of effective stress, $\bar{\sigma} = \sqrt{3J_2}$, and pressure, $p = \frac{I_1}{3}$. Rewriting Equation 2 in terms of $\bar{\sigma}$ and p, the following relationship is obtained:

$$\bar{\sigma} = \sqrt{3}C - 3\sqrt{3}ap \tag{5}$$

The JAS3D input parameters A_0 and A_1 are $\sqrt{3}C$ and $3\sqrt{3}a$, respectively. The JAS3D input parameters for the anhydrite are given in Table 3.

Table 3: Material properties of caprock 2 (anhydrite) (Butcher, 1997)

Parameters		Units	Values
Density (ρ)		kg/m^3	2300
Young's Modulus (E)		GPa	75.1
Poisson's Ratio (v)		-	0.35
Bulk Modulus (K)		GPa	83.4
Shear Modulus (μ)		GPa	27.8
Constants	A0	MPa	2338
	A1	-	2.338
	A2	-	0

3.1.4 Mechanical properties of other rocks around the salt dome

The surface overburden layer, which is mostly comprised of sand, is expected to exhibit elastic material behavior. The sand layer is considered isotropic and elastic, and has no assumed failure criteria. The upper caprock layer, consisting of gypsum and limestone, is also assumed to be elastic. Its properties are assumed to be the same as those used for the WH analyses (Sobolik and Ehgartner, 2001). The rock surrounding the salt dome is assumed to be an isotropic, homogeneous elastic sandstone. Its properties are assumed to to be the same as California mine sandstone (Lama and Vutukuri, 1978). Mechanical properties of each of these rocks used in the present analysis are listed in Table 4, 5, and 6.

Table 4: Material properties of sandy overburden (Sobolik and Ehgartner, 2001)

Parameters	Units	Values
Density	kg/m^3	1874
Young's Modulus	Pa	$0.1x10^9$
Poisson's Ratio		0.33

Table 5: Material properties of gypsum and limestone caprock (Sobolik and Ehgartner, 2001)

Parameters	Units	Values
Density	kg/m^3	2500
Young's Modulus	Pa	$7.0x10^9$
Poisson's Ratio		0.29

Table 6: Material properties of lithologies surrounding the salt dome (sandstone) (Lama and Vutukuri, 1978)

Parameters	Units	Values
Density	kg/m^3	2500
Young's Modulus	Pa	$7.32x10^9$
Poisson's Ratio		0.33

3.2 Cavern Model

3.2.1 Cavern geometry and layout

Table 7 lists the most recent sonar data for the BH caverns (Rautman and Ehgartner, 2004). These data were used to visualize the cavern shapes and define the minimum separation distance between caverns. The average cavern diameter is 221 ft which was calculated from the cavern volume knowing the top and bottom elevations. The average elevations of the top and the bottom of caverns are 2,286 ft and 4,176 ft, respectively (McHenry et al., 2003).

The shear zone shown in Figure 2 is ignored in the analysis. In the present model, we are trying to simulate a general case, and the shear zone presents a more unusual one. In addition, there is no contact surface data such as the friction coefficient or residual normal force applied on the shear zone. And by ignoring the shear zone, we are able to model the caverns using an axisymmetric analysis rather than having to resort to a more complicated 3-D model.

Table 7: Sonar data for BH caverns (Rautman and Ehgartner, 2004)

Cavern	Sonar Date	Nearest Cavern	Min Pillar (P), ft	Cavern Volume, bbls	Top of Cavern ft	Bottom of Cavern, ft	Avg. Diameter (D), ft	P/D Ratio
101	10/12/2000	106	463	12881863	2266	4176	220	2.1
102	2/5/1991	101	474	13011411	2300	4087	228	2.08
103	3/27/2002	108	403	12998974	2200	4054	224	1.8
104	10/1/2002	103	449	12914079	2278	4247	217	2.07
105	3/23/1999	104	456	12909010	2280	4232	217	2.1
106	1/23/1991	111	424	12910388	2284	4108	225	1.88
107	11/28/2000	108	446	13001793	2265	4118	224	1.99
108	3/24/1999	103	403	12918230	2334	4148	226	1.79
109	1/3/1991	114	459	12900201	2300	4273	216	2.12
110	8/28/2000	109	471	12992691	2300	4219	220	2.14
111	8/2/1991	106	424	12922425	2300	4243	218	1.94
112	6/22/1991	113	450	12933453	2300	4228	219	2.05
113	9/6/1991	108	412	12945091	2300	4166	223	1.85
114	9/6/1991	113	452	12869173	2300	4160	222	2.04
Average			442	12936342	**2286**	**4176**	**221**	2.00

As mentioned above, expansion opportunities include the addition of five caverns to the existing 14 caverns. A 19-cavern layout as shown Figure 8 is considered as the basic model. Symmetry planes, with an interior angel of 30°, are invoked to simplify modeling. In order to compare the analysis results to field data, Cavern 108 is regarded as the central cavern, Cavern 106 corresponds to the outmost cavern, and Cavern 101 is ignored. A circle fit roughly through the 2500 ft elevation contour line is taken as the dome's outer edge, and is 800 ft from the center of Cavern 101.

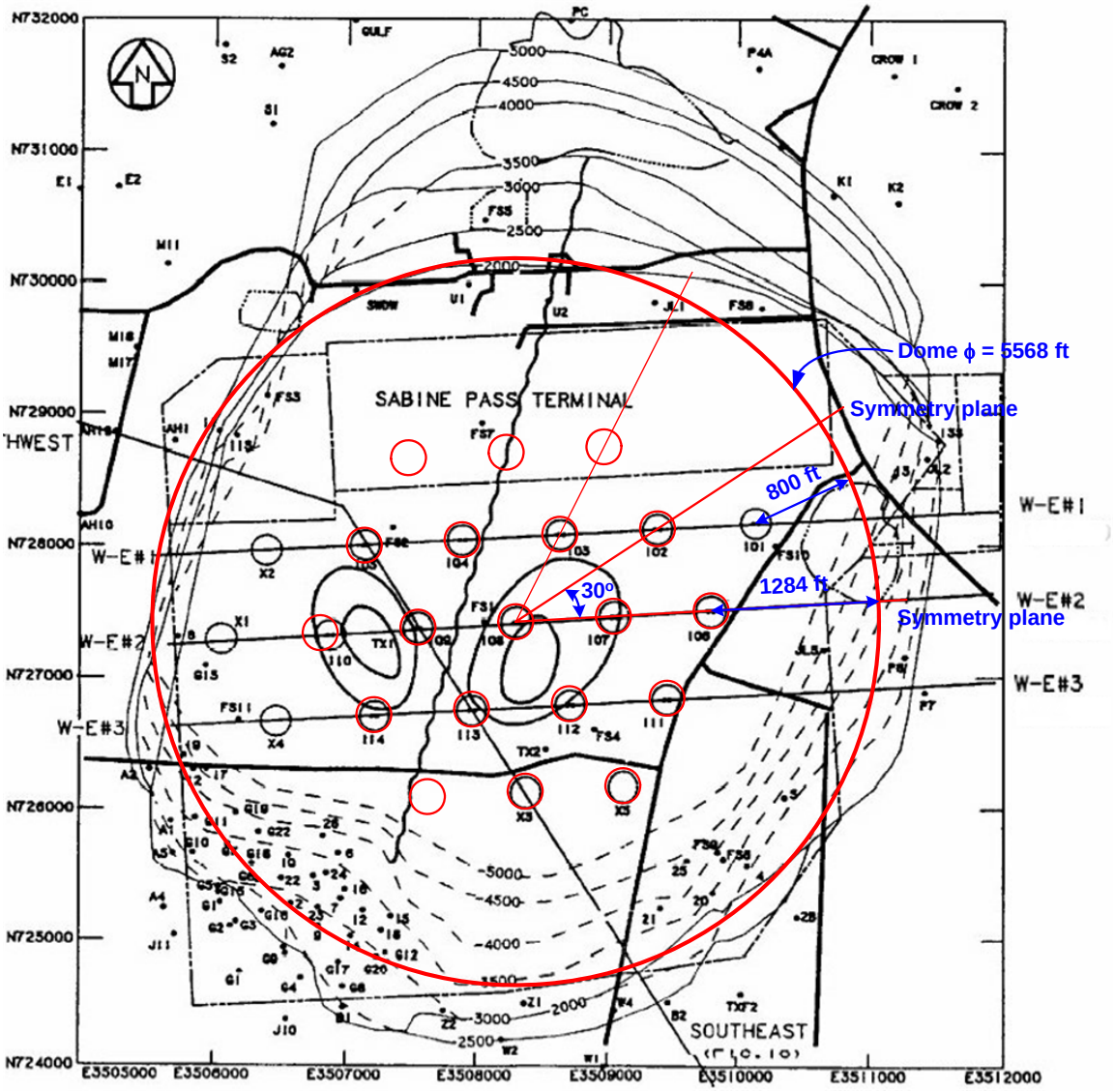

Figure 8: Location of caverns (black circles) and 19-cavern model layout (red circles)

The far-field boundary is 19,685 ft (6,000 m) from the center of the dome, which is approximately 3.5 times the salt dome diameter (1,697 m). A general rule in rock mechanics modeling is that the minimum size of the model should be 3 to 4 times the maximum dimension of the excavation in the model. Thus the dome may be considered to be subjected to a regional far-field stress state acting from an infinite distance away. Caverns can be arrayed geometrically in the dome as shown Figure 8.

Figure 9 shows the schematic diagram including the far-field boundary used for mesh generation. The initial diameter of the caverns is 221 ft. The caverns are spaced approximately 750 ft apart from each other (Magorian and Neal, 1988). Every 5 years, the caverns will be leached for drawdown. The drawdown process causes the volume of caverns to increase by 16 %. Because of this, the final diameter of the caverns is estimated to be 320 ft after 5 drawdowns (Ehgartner, 2004) resulting in a separation distance of 1,284 ft from the center of the outermost cavern to the edge of the dome.

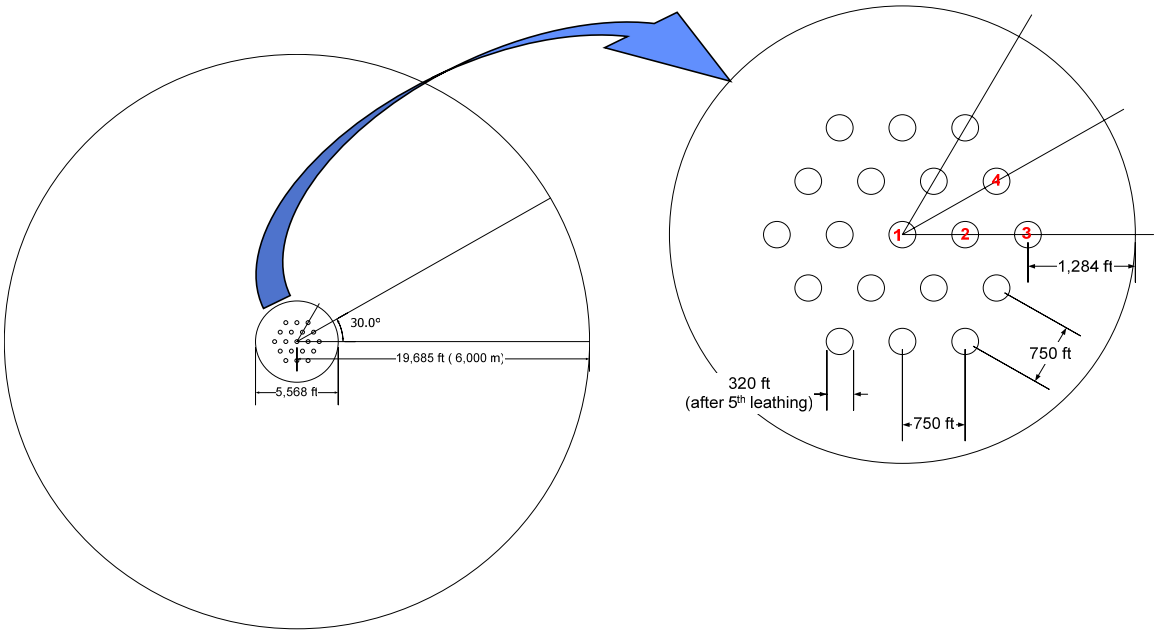

Figure 9: The layout of 19 cavern model in BH salt dome

3.2.2 Model history

The model is the same as was previously used to simulate WH caverns (Sobolik and Ehgartner, 2001). The analysis simulates caverns that were leached to full size over a one year period, filled with oil, and then permitted to creep for 20 years to approximate the current age of the caverns. Modeling of the leaching process of the caverns was accomplished by deleting elements along the walls of the caverns so that the volume increased by 16 percent for each leach, as shown in Table 8. Leaching was assumed to occur uniformly along the entire height of the cavern and not permitted in the floor or roof of the caverns. The 5-year period between each drawdown allows the stress state in the salt to return to a steady-state condition, as will be evidenced in the predicted closure rates. Thus the predicted stress states are not expected to be sensitive to the 5 year leach frequency used in the analyses.

The pressure condition applied to the cavern was based on an average wellhead pressure of 905 psi. The caverns at BH operate over a range of pressures from 850 psi to 960 psi under normal conditions. The caverns start at 850 psi, then, due to creep and thermal expansion of fluids, the pressure gradually rises to 960 psi. At that time the brine is removed from the cavern to reduce pressure down to 850 psi again. Thus, on average, a pressure of 905 psi is used (Ehgartner, 2004b) as typical for BH caverns wellhead pressure operating under normal conditions.

Analysis of cavern pressures at BH from 1990 to 2000 shows that a cavern is pressurized within its normal operating range 90 percent of the time and at lower pressures for 10 percent of the time. Therefore, in these analyses, a constant pressure is applied for the

majority of the time. Pressure drops are periodically included to simulate times when caverns are operated at lower than normal pressures and during workover conditions (0 psi wellhead pressure).

Rather than complicating the analyses, low pressure conditions are simulated at the extreme end of the less than normal range (0 psi wellhead pressure) to account for workover conditions, which occur every 5 years. This abrupt pressure drop will induce the greatest potential for damage. For simulation purposes, the pressure drop to 0 psi for each cavern lasts for 3 months, or 5 percent of time during a 5-year period. The duration of the workover may be slightly longer than is historically encountered in the field, but is chosen to provide an adverse condition and closely simulate actual subsidence measurements.

To simulate actual field conditions, not all caverns are in workover mode at the same time. The central cavern (Cavern 1 in Figure 9) in the field is the first cavern in the workover sequence beginning one year after initial cavern leaching. It is worked over every 5 years until the end of the simulations. The next closest neighboring cavern (Cavern 2 in Figure 9) is due to be worked over the following year. Because of mesh symmetry, workover pressures must be applied to the six caverns that make up this second set of caverns, which contains Cavern 2, at the same time. This results in the 6 caverns closest to Cavern 1 at low pressure starting one year after each workover of the central cavern. This condition enables the web of salt between adjacent caverns in workover mode to be examined for stability. In addition, the webs of salt between caverns in workover mode and those under normal operating pressures can be studied. The workover sequence continues with the outmost cavern along the 0° symmetry plane (Cavern 3 in Figure 9) being subject to workover pressures one year after the second set of caverns. The final set of caverns to undergo work over in the fourth year is those along 30° symmetry plane (Cavern 4 in Figure 9).

Table 8: Drawdown properties

Drawdown	Age of Cavern, years	Cavern volume prior to drawdown, bbls	Cavern height prior to drawdown, ft	Cavern diameter prior to drawdown, ft	Pillar width prior to drawdown, ft	P/D ratio
1	20	12936342*	1890	221	529	2.39
2	25	15006156	1890	238	512	2.15
3	30	17407141	1890	257	493	1.92
4	35	20192284	1890	276	474	1.71
5	40	23423049	1890	298	452	1.52
6	45	27170737	1890	321	429	1.34

* From Table 7

3.2.3 Thermal condition

The finite element model includes a depth-dependent temperature gradient which starts at 76.7 °F (24.84 °C) at the surface and is increased at the rate of 0.0141 °F/ft (0.0257 °C/m). The temperature profile is based on the average temperature data recorded in well logs from BH prior to leaching (Ballard and Ehgartner, 2000). The temperature distribution is important because the creep response of the salt is temperature dependent. Radial temperature gradients due to cavern cooling were not considered in these calculations. Previous 2D cavern studies have shown the predicted cavern deformation to be insensitive to radial thermal gradients developed by cooling effects of the cavern product (Hoffman, 1992).

4 MESH GENERATION

4.1 Construction of Mesh

Figure 10 shows the mesh and boundary condition for the 19-cavern, 5-leach model. Since the caverns are located in the central portion of the dome, symmetry planes can be used in the model. The model simulates 19 caverns in a systematic pattern with equal spacing and uniform cavern size and geometry. The 19-cavern model consists of 67,909 nodes and 60,552 elements.

The thicknesses of each layer are determined from the stratigraphy of the BH site shown in Figure 7. The radius of the salt dome is 2,784 ft (Figure 8). The diameter of the initial cavern is 221 ft and this will be increased by 7.7 % per drawdown. The SD from the edge of the dome to the center of outmost cavern is 1,284 ft.

Five material blocks are used in the model such as overburden, caprock 1, caprock 2, salt dome, and the lithologies surrounding the salt dome. The overburden is made of sand, the caprock 1 is made of gypsum or limestone, the caprock 2 is made of anhydrite. The surrounding rock is actually sedimentary rock that consists of sandstone and shale. For simplifying the mesh, the surrounding lithologies are assumed to be made of sandstone because the mechanical properties of them are similar.

An example input file to the mesh generation code FASTQ used to generate the mesh for 19-cavern model is provided in Appendix A. An example of a JAS3D input file used to simulate the salt dome behavior using 19-cavern mesh is provided in Appendix B, and a listing of the subroutine file to provide the pressure boundary condition on caverns is shown in Appendix C.

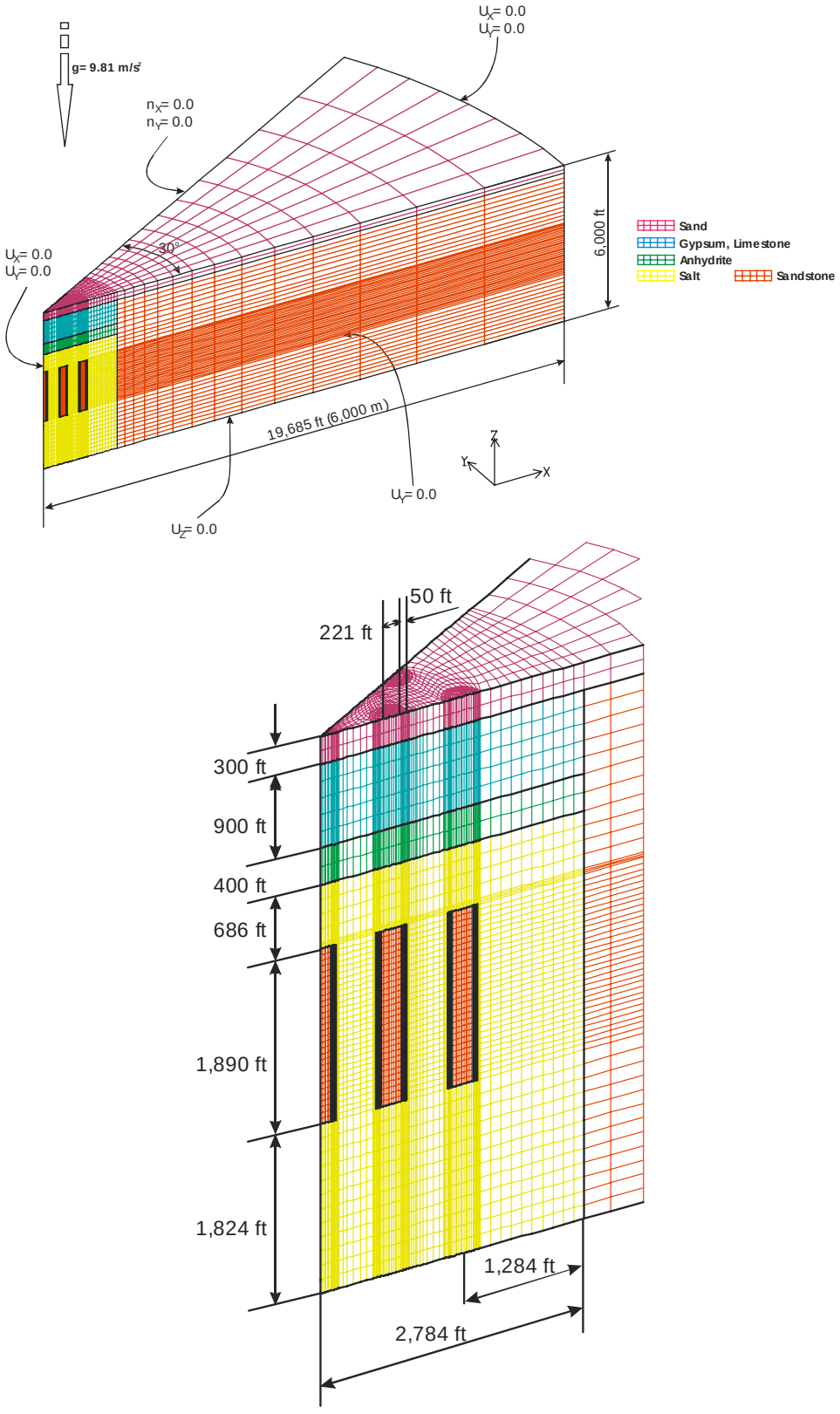

Figure 10: Mesh discretization and boundary conditions for 19 caverns and 5 leaching

4.2 Verification of Mesh

Figure 11 shows the mesh for the BH site and one from the previous WH analysis (Sobolik and Ehgartner, 2001). To verify the new mesh for the BH site, the results from the new mesh are compared with the published result from the WH mesh. For comparative purposes, the material properties of the overburden and caprock in WH mesh were assigned to those in the new mesh. Also, the sandstone in the new mesh was assigned WH salt properties since the WH analysis did not model the edge of the dome. Thus, the new mesh becomes similar to the WH mesh except for the thickness of each layer and the slightly deeper caverns at WH.

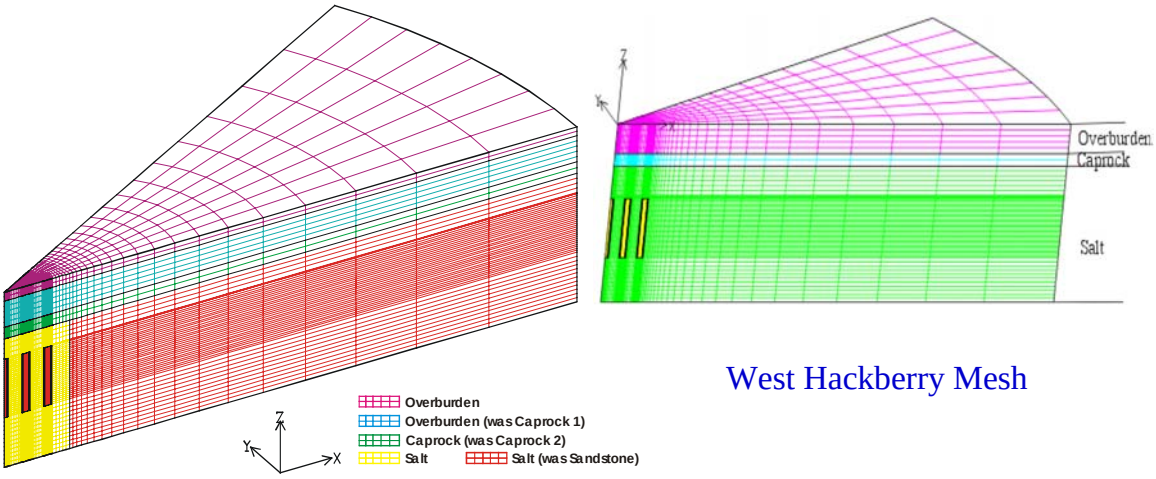

Figure 11: Mesh comparison between for the BH site and the WH site

Figure 12 and Figure 13 show the result of the minimum compressive stress and minimum safety factor for dilatancy using the adjusted BH mesh and the WH mesh (Sobolik and Ehgartner, 2001), respectively for the 45 year life cycle of the caverns. The results for the two meshes are very similar in both magnitude and tendency. Therefore, the new mesh appears to be reasonable for use in the BH analyses.

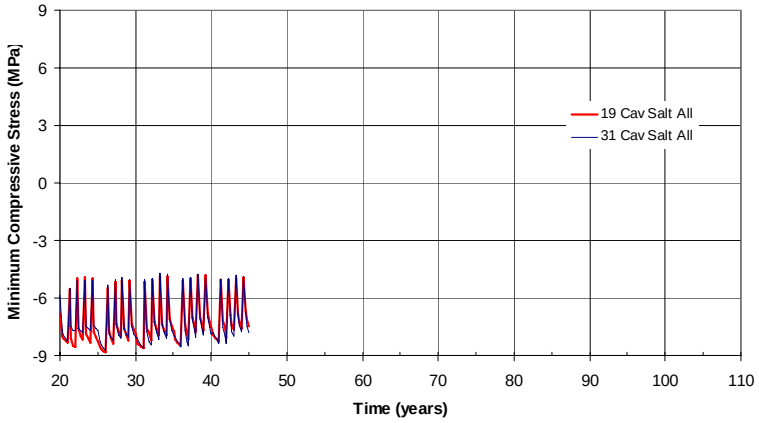

Big Hill

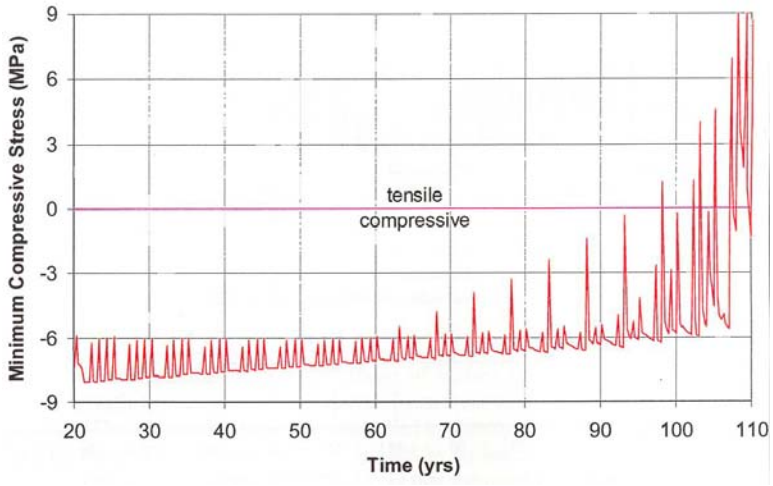

West Hackberry

Figure 12: The minimum compressive stress by the adjusted BH mesh compared with the WH mesh (Sobolik and Ehgartner, 2001).

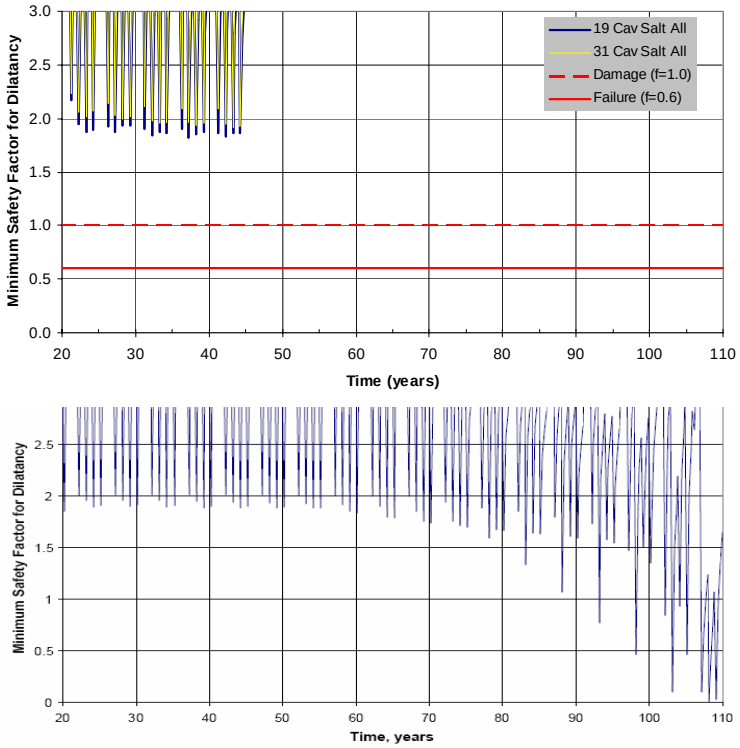

Figure 13: The minimum safety factor for dilatancy by the adjusted BH mesh compared with the WH mesh (Sobolik and Ehgartner, 2001).

5 BACK-FITTING ANALYSIS

5.1 Field Data

Two types of data have been collected for the SPR: subsidence measurements, and cavern pressures at the wellhead. Through the back-fitting analysis using the field data, the RF and the secondary constants of the salt and the Young's modulus of the rock surrounding the salt dome can be determined.

BH subsidence data exist back to April 1989, about the time when many of the caverns in the field were being developed. The subsidence surveys were performed on an approximately yearly basis. The surveys measure surface elevations above the caverns and at other selected locations of interest to the SPR. Subsidence is calculated as the difference or change between survey elevations. Table 9 lists the measured subsidence at the BH site and in Figure 14 the average value for each cavern is plotted.

The subsidence data is plotted in Figure 15 as a function of distance from Cavern 101 (located in the extreme NE corner of the cavern field as shown Figure 8). The data are divided for the first and last 5 years of the 10-year period, with the total also shown. A linear trend line is fit through the data for each planar feature showing a uniform subsidence in the western half of the field. There is a change in the rate of subsidence starting at a location 1800 ft west of cavern 101, and ending at 800 ft east of cavern 101. This is approximately the edge of the dome. The intersection of the planar features coincides with the active shear zone and faults shown in Figure 2 and Figure 3 and supports the association of subsidence with the East and West spines of the dome (Ehgartner and Bauer, 2004).

Table 9: Elevation data (ft) at well head measured at Big Hill (Ehgartner, 2004c)

	Apr-89	Jan-90	Jan-91	Jan-92	Oct-92	May-94	Feb-95	Dec-96	Jan-99
BH101A	94.24	94.25	94.22	94.13	94.16	94.17	94.16	94.11	94.13
BH101B	94.17	94.18	94.14	94.06	94.1	94.1	94.1	94.05	94.07
BH102A	95.73	95.71	95.63	95.57	95.6	95.59	95.58	95.52	95.52
BH102B	95.67	95.67	95.59	95.52	95.56	95.55	95.53	95.47	95.47
BH103A	96.15	96.11	96.04	95.97	96	95.98	95.96	95.89	95.89
BH103B	96.16	96.12	96.06	95.98	96	95.99	95.97	95.9	95.88
BH104A	97.02	96.96	96.89	96.79	96.83	96.8	96.77	96.7	96.69
BH104B	97.14	97.09	97	96.91	96.96	96.92	96.9	96.83	96.79
BH105A	98.66	98.6	98.53	98.44	98.45	98.45	98.42	98.35	98.35
BH105B	98.67	98.62	98.55	98.45	98.47	98.46	98.46	98.37	98.36
BH106A	91.21	91.18	91.12	91.05	91.09	91.09	91.07	91.01	91
BH106B	91.23	91.2	91.14	91.07	91.08	91.09	91.07	91.01	91.02
BH107A	97.67	97.61	97.54	97.47	97.49	97.48	97.47	#N/A	97.39
BH107B	97.66	97.62	97.55	97.46	97.49	97.48	97.45	97.37	97.36
BH108A	94.69	94.63	94.54	94.44	94.49	94.47	94.42	94.34	94.3
BH108B	94.68	94.66	94.57	94.46	94.47	94.48	94.47	94.36	94.4
BH109A	96.59	96.54	96.47	96.35	96.38	96.36	96.34	96.24	96.25
BH109B	96.65	96.6	96.52	96.41	96.44	96.44	96.39	96.31	96.31
BH110A	96.13	96.1	96.03	95.93	95.96	95.94	95.92	95.82	95.81
BH110B	96.16	96.1	96.02	95.9	95.94	95.92	95.88	95.8	95.79
BH111A	91.17	91.13	91.06	90.97	91.01	91	91.02	90.92	90.88
BH111B	91.24	91.2	91.15	91.04	91.06	91.06	91.09	90.98	90.95
BH112A	91.68	91.64	91.57	91.46	91.47	91.47	91.47	91.38	91.34
BH112B	91.7	91.64	91.58	91.47	91.48	91.48	91.49	91.39	91.35
BH113A	92.18	92.12	92.07	91.94	91.96	91.96	91.94	91.85	91.82
BH113B	92.11	92.06	92.01	91.86	91.88	91.88	91.86	91.77	91.75
BH114A	88.37	88.3	88.24	88.11	88.16	88.14	88.1	88.01	88
BH114B	88.53	88.47	88.42	88.3	88.35	88.33	88.28	88.2	88.19

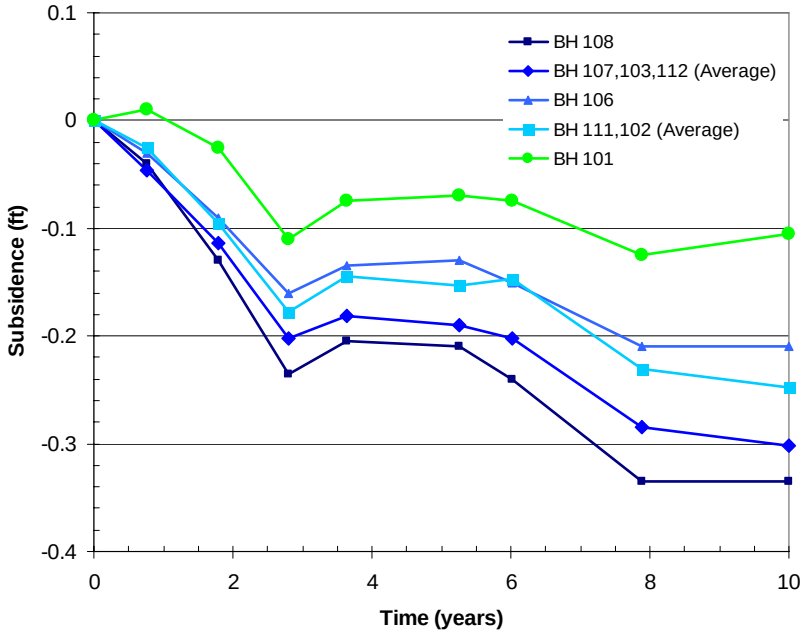

Figure 14: The measured average subsidence over each cavern

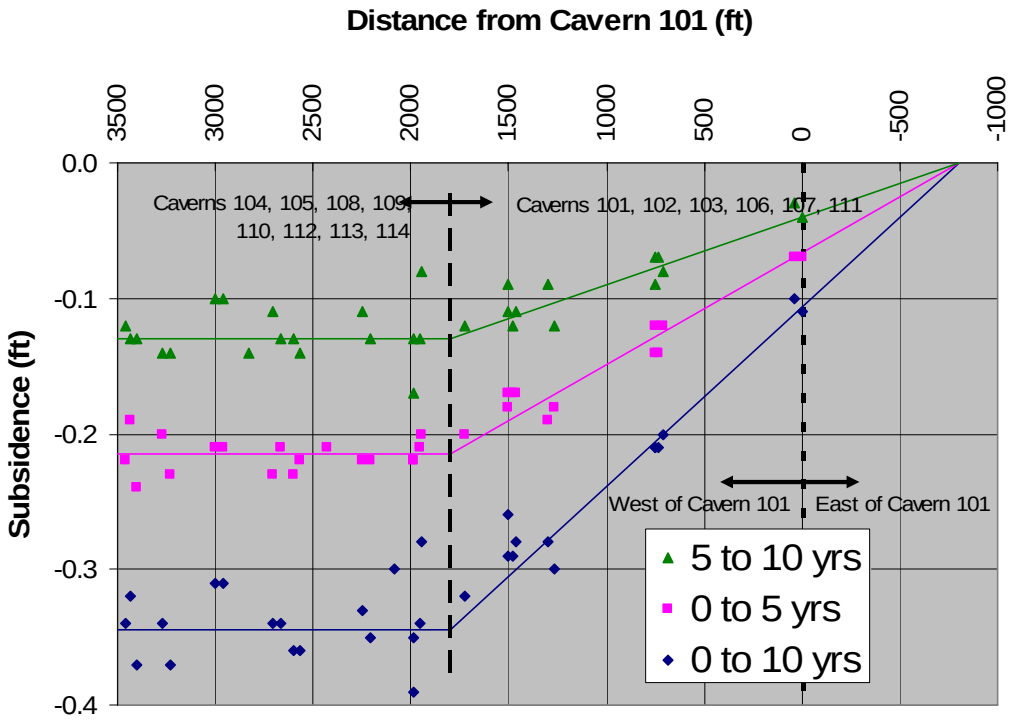

Figure 15: Subsidence data as a function of distance from Cavern 101 suggesting uniform subsidence associated with west spine and tilted subsidence for east spine (Ehgartner and Bauer, 2004).

Figure 16 shows the average cavern closure of 14 caverns from the analysis using the latest version of CAVEMAN, which is the code for SPR cavern pressure analysis (Ballard and Ehgartner, 2000). The average volumetric closure in the field was calculated to be 0.26% per year (Ehgartner, 2004d). This result is based on the measured cavern pressures at the wellhead over the last 14 years. Knowing this number, the compressibility of the cavern (oil/brine/salt), and the change in fluid temperatures, it is possible to account for the measured pressures each day.

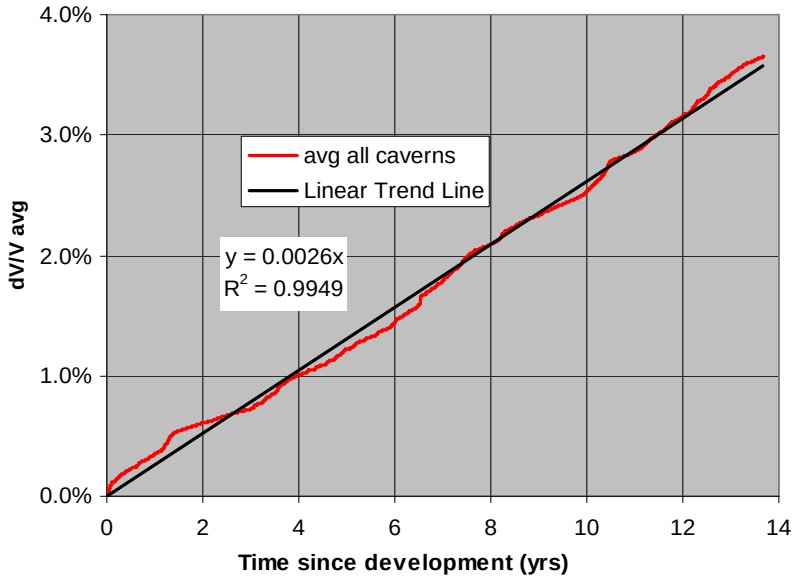

Figure 16: Average decrease in storage volume of 14 caverns in the BH salt dome (Ehgartner, 2004d)

5.2 Selection of Model

In order to determine the values of the unmeasured parameters of the salt and lithologies around the salt dome, the 19-cavern model is used as a back-fitting analysis. Because subsidence is a function of the number of caverns underground, the number also affects the closure rates. Fourteen caverns exist at the site right now, so to obtain the values of analysis parameter through back-fitting analysis using the field data such as subsidence and volume change of caverns with time, 19-cavern model is reasonable.

As mentioned in Section 3.2.1, Cavern 108 is regarded as the central cavern of the model. Then the relationship between the caverns in the model and the field is set up as shown Figure 8 and Figure 9. Cavern 1 in the model corresponds to Cavern 108 in the field; Cavern 2 in the model corresponds to Caverns 107, 103, and 112 in the field. Similarly, Cavern 3 in the model corresponds to Cavern 106; Cavern 4 in the model corresponds to Cavern 102 and 111. Cavern 101 in the field is ignored on the model.

5.3 Selection of Parameters to Calibrate

As mentioned in Section 3.1.2, RF and the secondary constants of salt are determined by calibrating those to best match the measured closure and subsidence. RF is defined as follows:

$$E_C = E_{WIPP} / RF \tag{6}$$

where, E_C = Calibrated Young's modulus of salt

E_{WIPP} = Measured Young's modulus of salt at WIPP site

Earlier versions of the JAS3D code, SANCHO code, which has been used to simulate the salt behavior, has a great difficulty in treating stiff equations, such as those used to describe transient creep response. In the solution method used in this code, the finite element advancement of the calculation can produce considerable error causing the code to fail. In an attempt to obtain a solution, typically, the time step is reduced. However, time step reduction results in extremely long run times, often without a result or a satisfactory solution. As a result, Morgan and Krieg (1988) introduced an artifact into the code as an approximation to transient response, in addition this facilitated the code calculations significantly. The approximation uses a reduction of the elastic modulus by an arbitrary amount, 12.5, which was chosen by back-fitting to match the WIPP South Drift data (Munson, 2004). RF of WH salt and BH salt is based on the WIPP salt (Munson, 1998). Thus the value of 12.5 is also used for the RF in this analysis.

The secondary constants of salt creep are controlled by a structural multiplication factor (SMF) and a thermal constant multiplication factor (TMF), which are related to the creep constant and the thermal constant, respectively. TMF of WH salt was derived to be 0.503 by Ehgartner and Sobolik (2002). This TMF value is used for this analysis because the thermal characteristic of BH salt is similar to WH. The salt at BH has 9.6 % impurities in it (Ehgartner, 2004), so the creep closure rate is expected to be different from that of WH. SMF also can be adjusted to match the volume closure of caverns.

In a manner similar to determining the RF of salt, the Young's modulus of the rock around the salt dome is can be adjusted to match the field data. Young's modulus of anhydrite was measured to be 75.1 GPa at the WIPP site (Krieg, 1984). This value is much larger than that given in handbooks (Table 10). The modulus of anhydrite is fixed as 75.1 GPa for simplifying the parameter sensitivity study. Overburden made of sand is assumed the same as that found at WH. It is assumed to be too thin to have an effect on the subsidence. Therefore Young's modulus of caprock 1 (Limestone) and surrounding rock (sandstone) can be treated as adjustable parameters for the back analysis.

Table 10: Young's moduli of rocks from handbooks (unit: GPa)

Rocks	Carmichael (1984)	Touloukian and Ho (1981)
Anhydrite	-	1 to 20
Dolomite	10 to 80	2 to 71
Gypsum	-	2
Limestone	3 to 100	2 to 81
Sandstone	0.4 to 70	4 to 52
Shale	0.4 to 70	2 to 52

5.4 Results of Back-fitting Analysis

As discussed above, the adjustable parameters are SMF of salt, Young's modulus of caprock 1 and the surrounding rock. These parameters were estimated from iterative back-fitting analyses to fit the measurements such as the subsidence and the volume change of caverns due to salt creep. According to the experience from a number of back-fitting analyses to match the field data, SMF has a strong relationship with the volumetric closure of caverns in salt dome, Young's modulus of caprock 1 is strongly related to the subsidence around the center of the dome, and Young's modulus of surrounding rock is strongly related to the subsidence around the edge of the dome.

Young's modulus of limestone (caprock 1) is determined to be 21 GPa. The rock surrounding the dome is a sedimentary rock that consists of sandstone and shale. The Young's modulus of the layered surrounding rock has large uncertainty. To match well the field data, the surrounding rock should be rigid to impede the subsidence around the dome edge. Thus, maximum value of the modulus of sandstone as listed in Table 10, 70 GPa, is used for the surrounding rock.

Figure 17 shows the predicted surface subsidence troughs from the back analyses with the measured subsidence as a function of distance from Cavern 108 at 5 years, 10 years, and between 5 and 10 years. The material properties including calibrated values (bold font) in Table 11 and Table 12 are used as input data. The influence of subsidence is predicted to extend beyond the edge of the salt dome, to over 5,000 ft from the center of the cavern field. The analysis results match well with the field data within 1,000 ft distance.

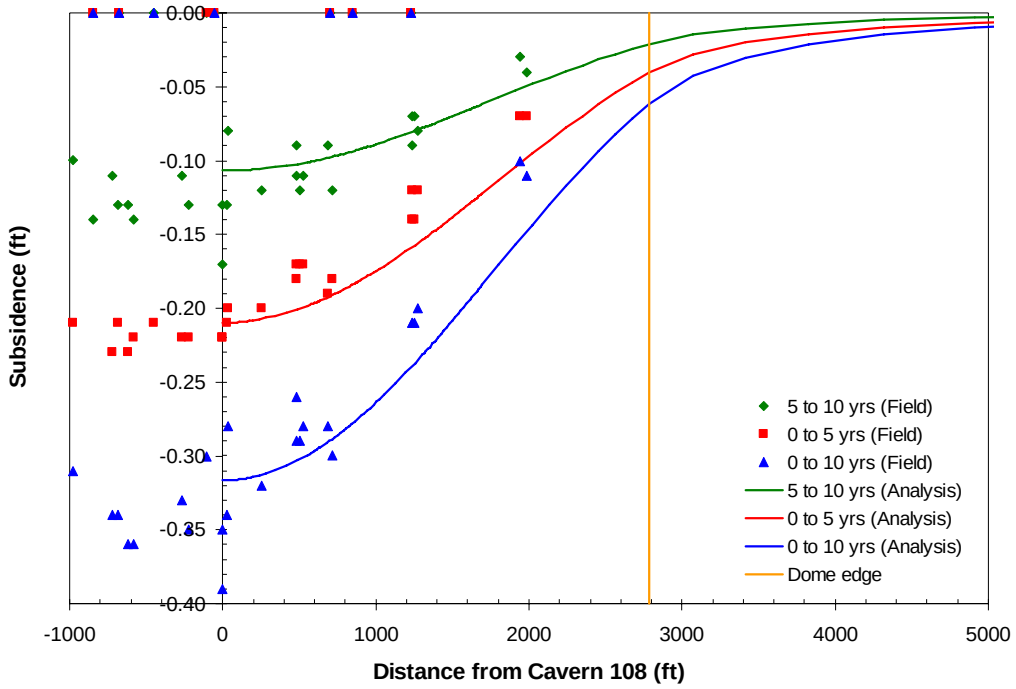

Figure 17: Predicted surface subsidence (solid line) using the 19-cavern model with the measured subsidence (symbols) (Ehgartner and Bauer, 2004) as a function of distance from Cavern 108 at 5 years, 10 years, and between 5 and 10 years (SMF is 1.5, Young's moduli of the caprock 1 and the surrounding rock are 21 GPa, and 70 GPa respectively).

Table 11: Material properties of BH salt used in the analyses

	Units	Salt Dome		References
		Big Hill Salt	West Hackberry Salt	
Young's modulus (E)	GPa	31	31	Krieg, 1984
Density (ρ)	kg/m^3	2300	2300	Krieg, 1984
Poisson's ratio (v)		0.25	0.25	Krieg, 1984
Elastic modulus reduction factor (RF)		12.5	12.5	Morgan and Krieg, 1988
Bulk modulus (K)	GPa	1.653	1.653	Calculated using E and v
Two mu (2μ)	GPa	1.984	1.984	Calculated using E and v
Creep constant (A)	Pa$^{-4.9}$/s	5.79×10^{-36}	5.79×10^{-36}	Krieg, 1984
Structure multiplication factor (SMF)		1.5	7.5	Back analysis
Calibrated creep constant	Pa$^{-4.9}$/s	8.69×10^{-36}	43.4×10^{-36}	Back analysis
Stress exponent (n)		4.9	4.9	Krieg, 1984
Thermal constant (Q)	cal/mol	12000	12000	Krieg, 1984
Thermal constant multiplication factor (TMF)		0.503	0.503	Ehgartner and Sobolik, 2002
Calibrated thermal constant	cal/mol	6036	6036	Ehgartner and Sobolik, 2002

Table 12: Material properties of lithologies around salt dome used in the analyses

	Units	Overburden (Sand)	Caprock 1 (Limestone)	Caprock 2 (Anhydrite)	Surrounding Rock (Sandstone)
Young's modulus	GPa	0.1	21	75.1	70
Density	kg/m^3	1874	2500	2300	2500
Poisson's ratio	0.25	0.33	0.29	0.35	0.33
Bulk modulus	GPa	N/A	N/A	83.44	N/A
Two mu	GPa	N/A	N/A	55.63	N/A
A_0	MPa	N/A	N/A	2338	N/A
A_1		N/A	N/A	2.338	N/A
A_2		N/A	N/A	0	N/A

Figure 18 compares the predicted subsidence at the center of four caverns on the surface by the present analysis with measured field data. Figure 19 compares the average predicted subsidence with the average measured data of the selected seven caverns. The predicted subsidence agrees closely to the measured values.

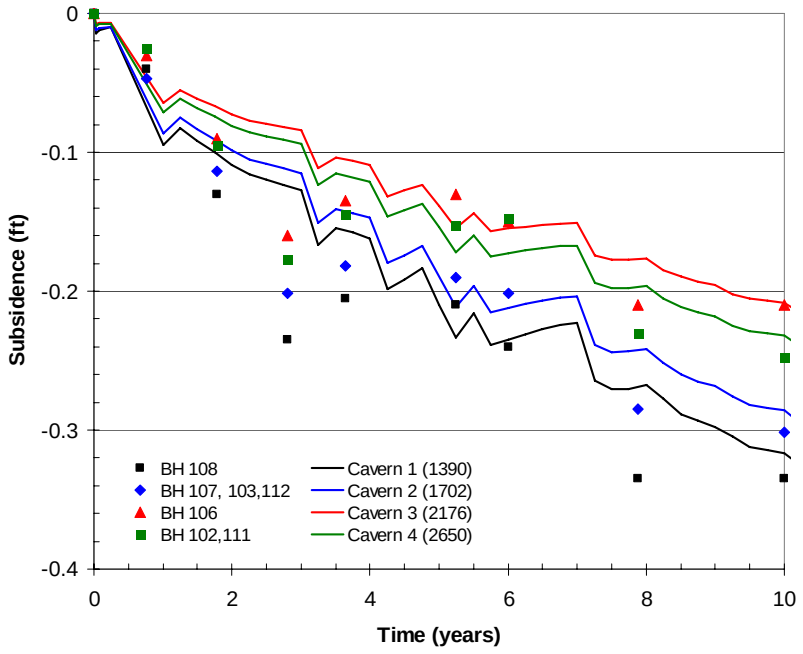

Figure 18: Predicted response (solid lines) by the 19-cavern and 5-leaching model with measured data (symbols); ( ) indicates the node numbers of the center of each cavern on the surface.

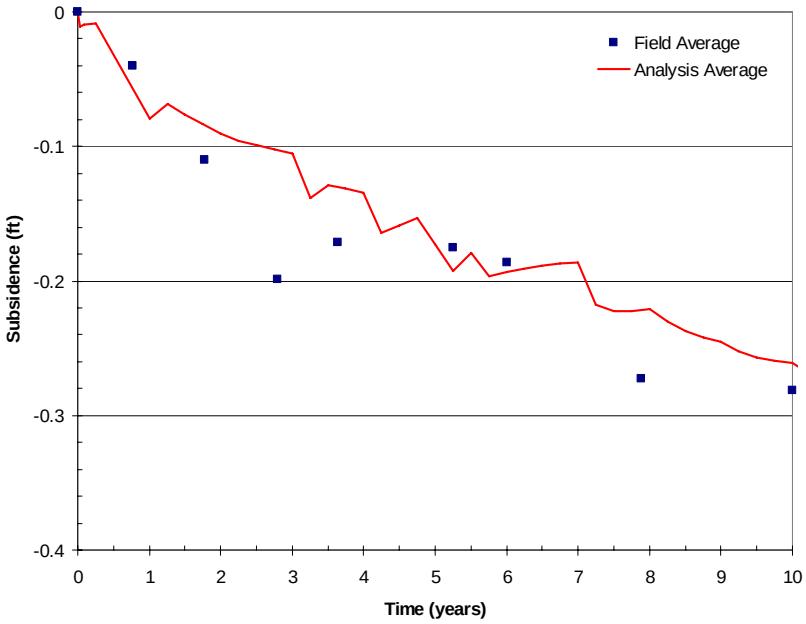

Figure 19: Average predicted response of four caverns with the average measured data of the selected seven caverns (19-cavern 5-leaching model).

Figure 20 shows the predicted decrease in storage volume of 19 caverns along with field data for 14 years since initial cavern leaching started. The average volumetric closure was measured to be 0.26% per year as discussed in Section 5.1. To match the field volumetric closure, SMF of salt is calibrated by a number of back-fitting analyses. Finally, SMF was determined to be 1.5. Therefore the creep constant is calculated to be 8.69×10^{-36}. The predicted closure rate agrees closely to the measured values. In the case of WH site, SMF was determined to be 7.5 (Creep constant = 43.4×10^{-36}) (Ehgartner and Sobolik, 2002). In other words, the creep rate of BH salt appears slower than WH salt.

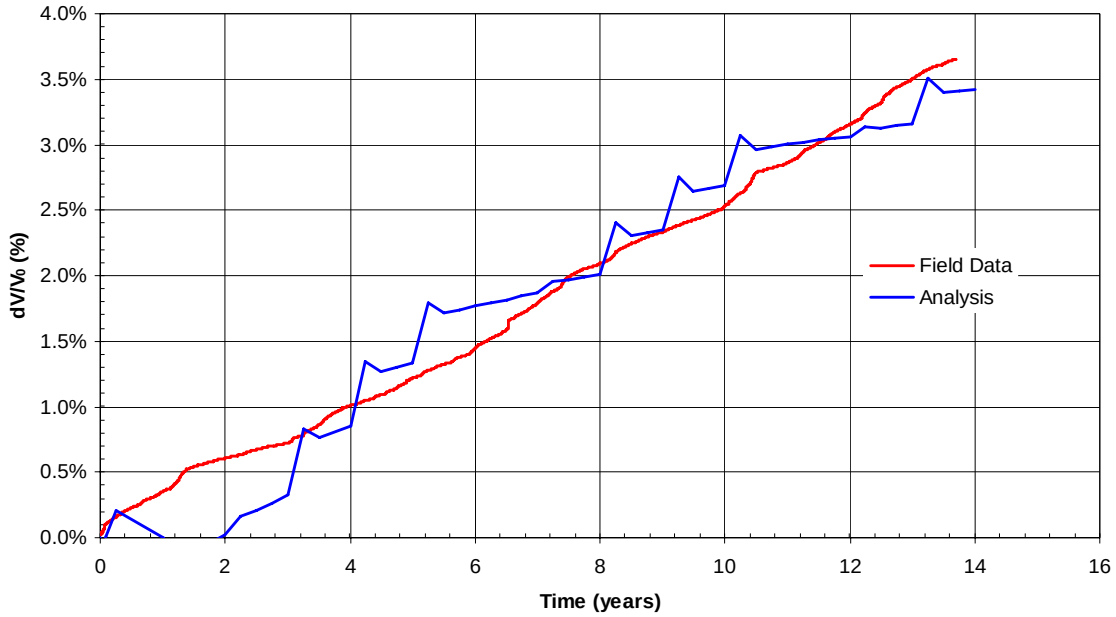

Figure 20: Predicted volumetric closure normalized by cavern volume immediately following each leach with the field data at BH site

5.5 Necessity of Contact Surface in the Model

If the salt dome pulls away from the surrounding rock due to salt creep closure, the concept model of contact surface between them should be considered. The stress changes with time are checked at the several elements expected to split apart as shown in Figure 21. Figure 22 through Figure 26 show the change of stresses over time at the considered elements. All stresses appear negative, which means the elements are contently in a compressive stress state. Thus, splitting will not occur over time at the dome boundary. Therefore, it is not necessary to consider the contact surface in the model.

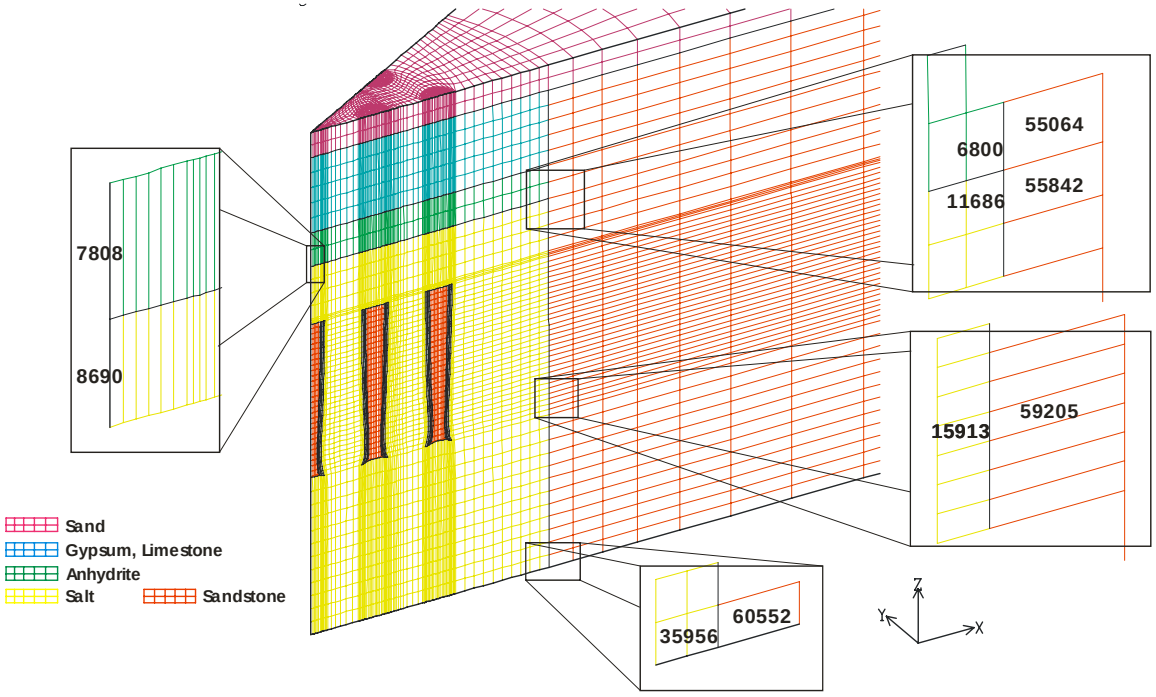

Figure 21: Number of elements expected to be split between the salt dome and the around rock

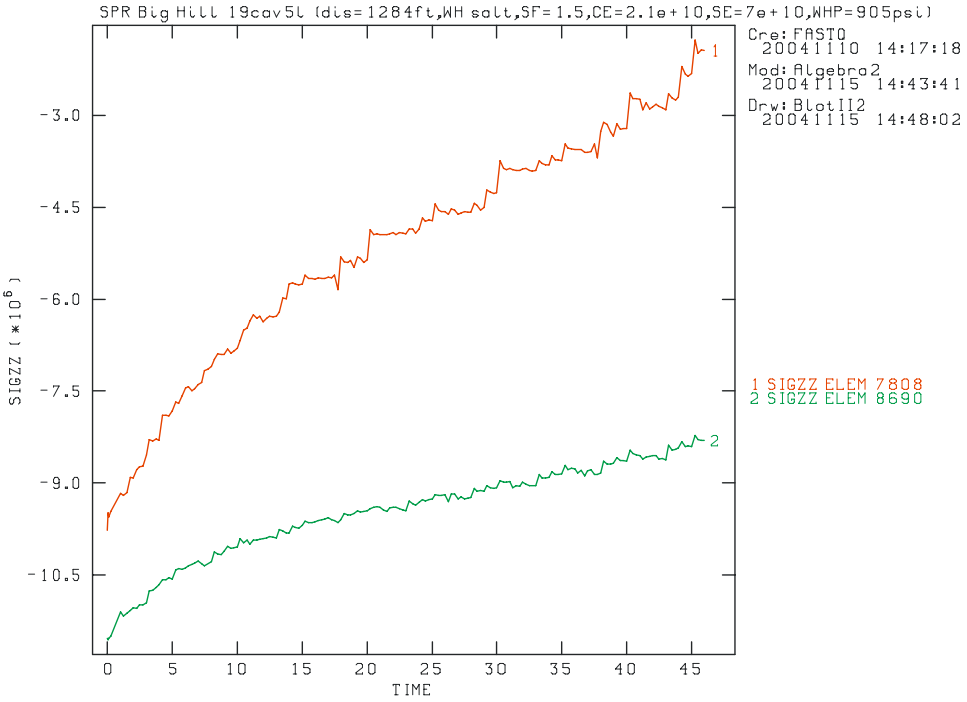

Figure 22: Stress change with time in z-direction at Element 7808 and 8690 (Unit: Pa, Years)

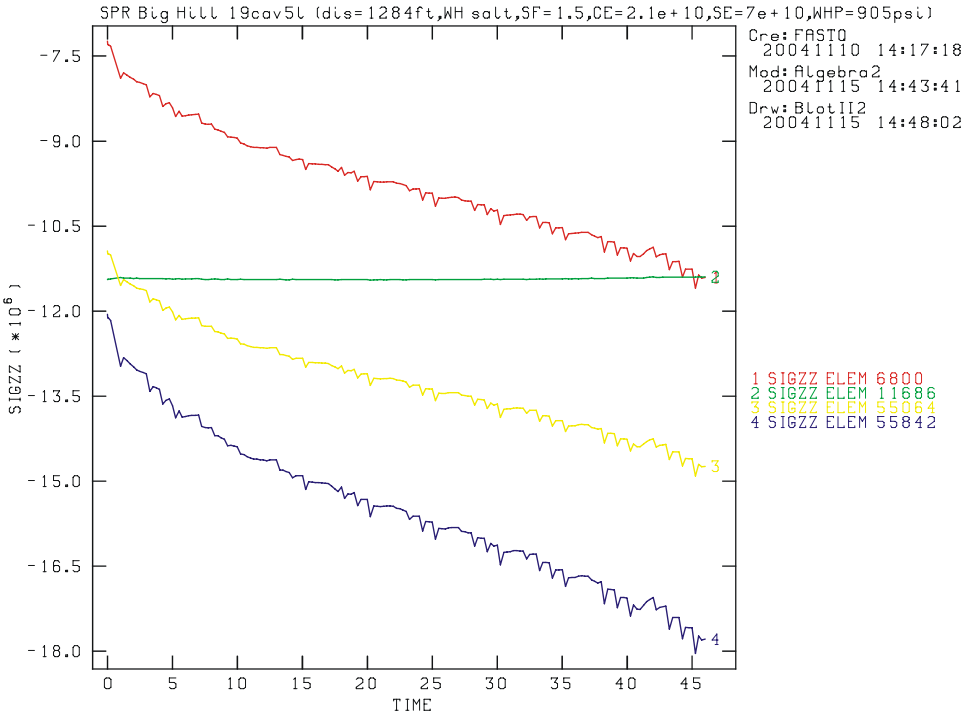

Figure 23: Stress change with time in z-direction at Element 6800, 11686, 55064, and 55842 (Unit: Pa, Years)

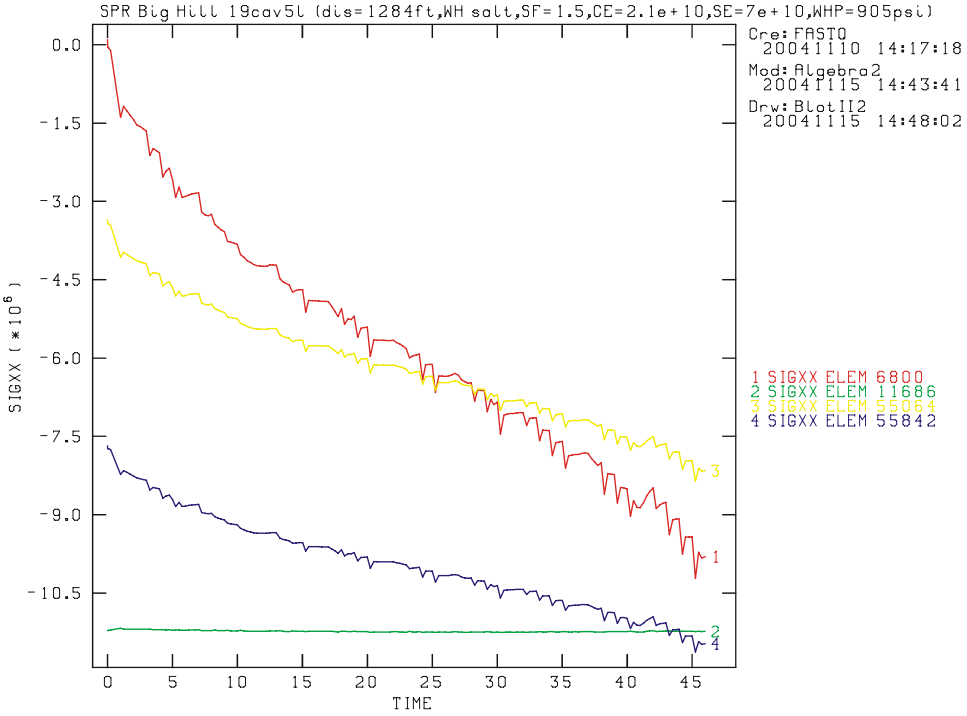

Figure 24: Stress change with time in x-direction at Element 6800, 11686, 55064, and 55842 (Unit: Pa, Years)

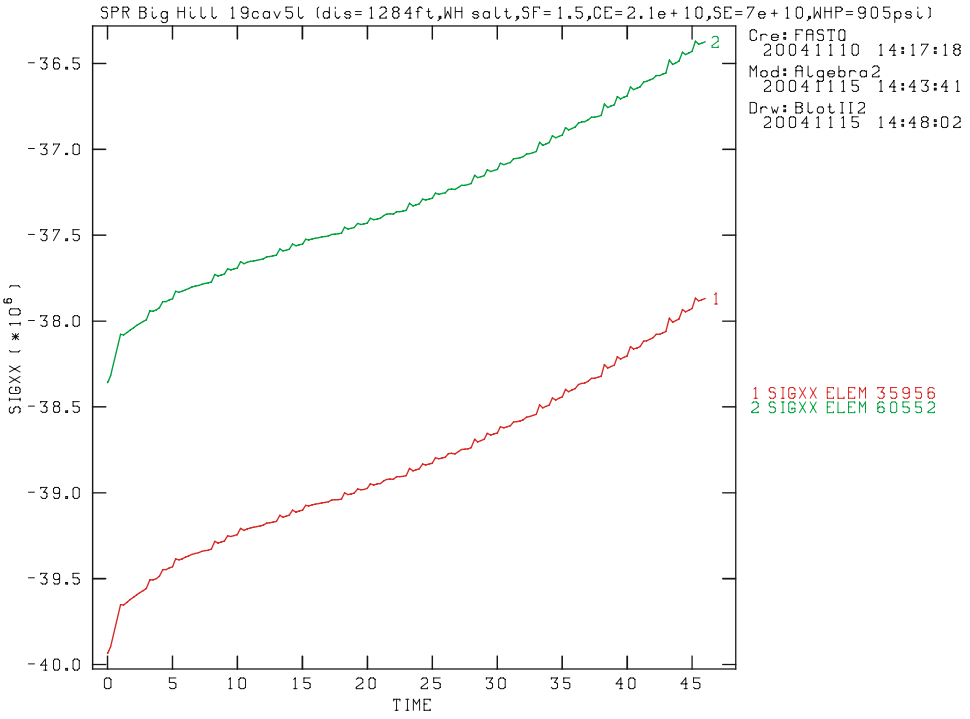

Figure 25: Stress change with time in x-direction at Element 35956 and 60552 (Unit: Pa, Years)

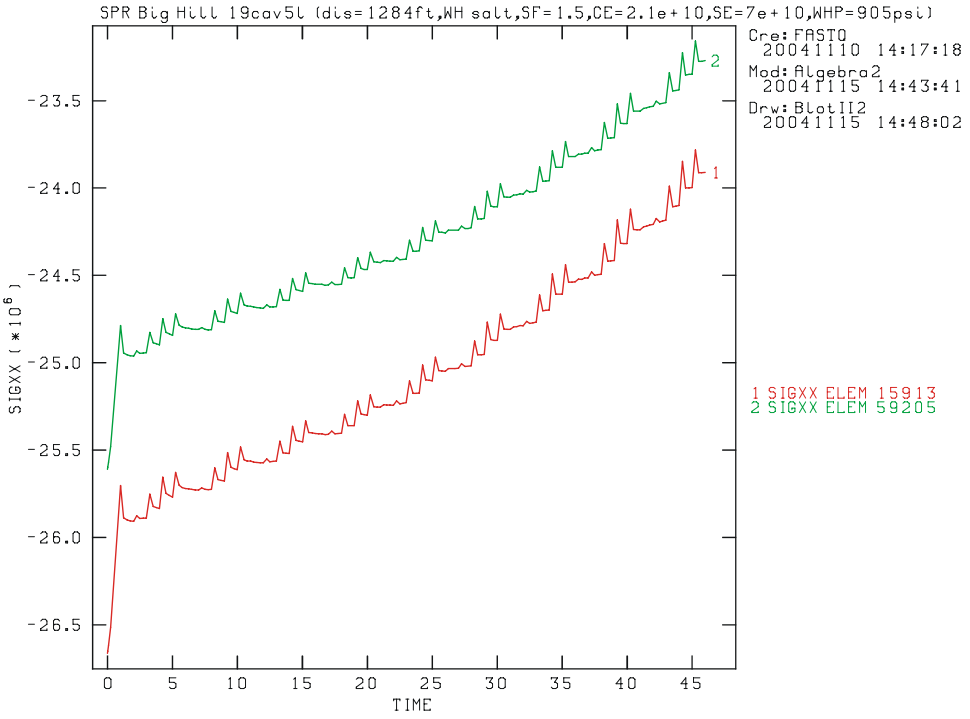

Figure 26: Stress change with time in x-direction at Element 15913 and 59205 (Unit: Pa, Years)

6 FAILURE CRITERIA

6.1 Structural Stability of Salt Dome

This study evaluated the potential for damage to or around SPR caverns based on two criteria: dilatant damage and tensile failure. Dilatancy is considered the onset of damage to the salt resulting in potentially large increases in permeability.

A dilatant damage criterion is used to delineate potential zones of dilatancy in the salt formation surrounding the storage facility. Dilatancy is attributed to micro-fracturing or changes in the pore structure of the salt, resulting in an increase in permeability. In this study, two dilatancy criteria are used for checking the structural stability. One was taken from the literature which shows a very consistent ratio of 0.25 between the second invariant of the deviatoric stress and the first invariant of stress. The other was taken from a laboratory evaluation of damage criteria and permeability of BH salt (Lee et al., 2004).

The potential for dilatant damage is defined by a "damage" safety factor (D) which is expressed as follows:

$$D = \frac{I_1}{4\sqrt{J_2}} \tag{7}$$

where, $J_2 =$ the second invariant of the deviatoric stress tensor,

$I_1 =$ the first invariant of the stress tensor ($I_1 = \sigma_m$, where σ_m is the mean stress).

When *D* is equal to or less than one, the shear stresses in the salt are large compared to the mean stress and the potential for dilatant behavior is high (Speirs, 1988; Van Sambeek 1993). Hunsche (1992) suggests that dilatancy is linked to creep rupture in that because as the rock salt dilates, it looses structure and may fail after some time due to creep rupture. A summary of laboratory tests on SPR and other rock salts along with failure and damage criteria are compiled in Tavares (1994). Based on an evaluation of the SPR test data in terms of the above criteria, failure occurs when the damage safety factor is less than 0.6.

Lee et al. (2004) suggested the following strength criterion of BH salt based on a series of quasi-static triaxial compression tests:

$$\sqrt{J_2}(\text{psi}) = 1746 - 1320.5e^{-0.00034 I_1(\text{psi})} \tag{8}$$

J_2, I_1 are the stress invariants as in Equation (7).

The comparison of different damage strength criteria are provided in Appendix D. To calculate the dilatancy damage potential in salt, the post-processing code ALGEBRA is used with the JAS3D output file to determine spatial locations of dilatancy damage. An ALEGRA input file used to compute dilatancy per Equations (7) and (8) is shown in Appendix E.

For the purposes of these analyses, the tensile strength of the salt was conservatively assumed to be zero. Tensile cracking in rock salt tends to initiate perpendicular to the largest tensile stress in the rock. The potential for tensile failure exists if the maximum principal stress is tensile or numerically positive.

It should be emphasized that the above dilatation criterion is not used in the present study to quantify damage, but merely to identify regions with a high potential for damage even though the estimates are considered conservative for the reasons stated above. This criterion identifies regions where the deviatoric stress is high and the mean stress is low, a stress state conducive to dilation. No comprehensive constitutive model exists at this time which can predict damage evolution in a reasonable computation time for a 3D problem of this size. Hence, the post-processed dilatation criteria were used as a conservative engineering approach to estimate possible regions of salt dilation. Much can be inferred from this approach. For example, if the dilatant damage safety factor is decreasing with time, it can be concluded that the potential for damage is increasing. Hence, salt healing (a reduction in dilatancy) is not likely to be occurring. Second, if the predicted damage is growing in both size and magnitude, then the damaged region (fracture or dilation) will continue to grow. Similarly, if a tensile region is predicted to be growing in both size and magnitude, the resulting fractures, although not explicitly modeled, should also grow.

6.2 Allowable Strains for Well and Surface Structures

The physical presence of wells and surface structures is not included in the finite element model, but the potential for ground deformation to damage these structures can be conservatively estimated by assuming that they will deform according to the predicted ground strains. At wells locations, subsidence will primarily induce elongation of the axis of the well. Under these conditions, the cemented annulus of the wells may crack forming a horizontal tensile fracture that may extend around the wellbore. This may not result in vertical fluid migration along the casing, but could permit horizontal flow. This could cause problems, especially in the caprock, where acidic ground waters may gain access to the steel casing and corrode it. More extensive damage could heavily fracture the cement which could result in a loss of well integrity in that leakage could occur from the cavern along the outside of the casing.

The allowable strain for purposes of this study is assumed to be 2 millistrains in compression and 0.2 millistrains in tension. This would be typical of cement with a compressive strength in the range from 2,500 to 5,000 psi (Thorton and Lew, 1983). The benefit of the steel casings in reinforcing the strength of the cement, especially under elongation, is not accounted for in this simplistic evaluation.

Structural damage on the surface is typically caused by large accumulated surface strains resulting from surface subsidence. These strains can cause distortion, cracking, and failure of buildings, pipelines, roads, bridges, and other infrastructure. Surface strains will accumulate in structures over time, which increases the possibility of damage in older facilities. Subsidence strains tend to be compressive in the central portion of the subsided area and become tensile in nature for areas farther removed. Some guidance and solutions

are available to evaluate the predicted surface strains. These criteria vary from country to country, possibly due to different building codes and structural materials (Peng, 1985).

The criteria vary in some countries depending on application and criteria for shear strains have not been found, perhaps because they are a minor influence. For purposes of this study, the allowable strain is taken to be 1 millistrain for both compression and tension. In practice, allowable strain limits for a structure are design specific and should be examined on a case-by-case basis.

7 COMPUTER CODES

The finite element code used in the present calculations, JAS3D (Blandford, 1998), uses an eight-node hexahedral Lagrangian uniform strain element with hourglass stiffness to control zero energy modes. A nonlinear conjugate gradient method is used to solve the nonlinear system of equations. This efficient solution scheme is considerably faster than the direct solvers which are used in most commercial codes and is a product of decades of research and development into nonlinear large strain finite element analyses. JAS3D includes at least 30 different material models. Three material models were chosen for use in the model described in this report: an elastic model for the overburden, upper caprock, and sandstone; a crushable soil and foams model for the anhydrite caprock layer; and a power law creep model for the salt. Related preprocessing, mesh generation, and post-processing codes were used in conjunction with JAS3D. Applicable software and version number used in this analysis are listed in Table 13.

Table 13: Applicable software and version number

Code Name	Version	Uses
APREPRO	1.71	Preprocessor
FASTQ	3.12	Mesh Generation
GEN3D	1.20	Mesh Generation
GJOIN	1.42	Mesh Generation
EMERGE	1.50	Mesh Generation
JAS3D	2.0.F	Solver
ALGEBRA2	1.22	Postprocessor
BLOT II2	1.39	Postprocessor

8 ANALYSES RESULTS

8.1 Cavern Deformation

Creep closure is known to decrease cavern volume over time and is more pronounced near the bottom of the caverns. The flow of salt can be illustrated by displacements vectors at each node. The deformed cavern shapes and displacement vectors are shown in Figure 27 at 46 years, immediately before the 6th leach. The salt flows are primarily downward near the roofs of the caverns, upward near the floors, and laterally in the pillars of salt. The greatest displacements occur in the floors of the caverns. The predicted displacements in the center of the floor are approximately twice those predicted in the edge of the floor. This produces an upward curvature in the floor. The lateral salt deformation causes the outer cavern walls to shift inward over time.

The vertical displacements are quantified in Figure 28, immediately following the 5th leach. Positive displacements are directed upward.

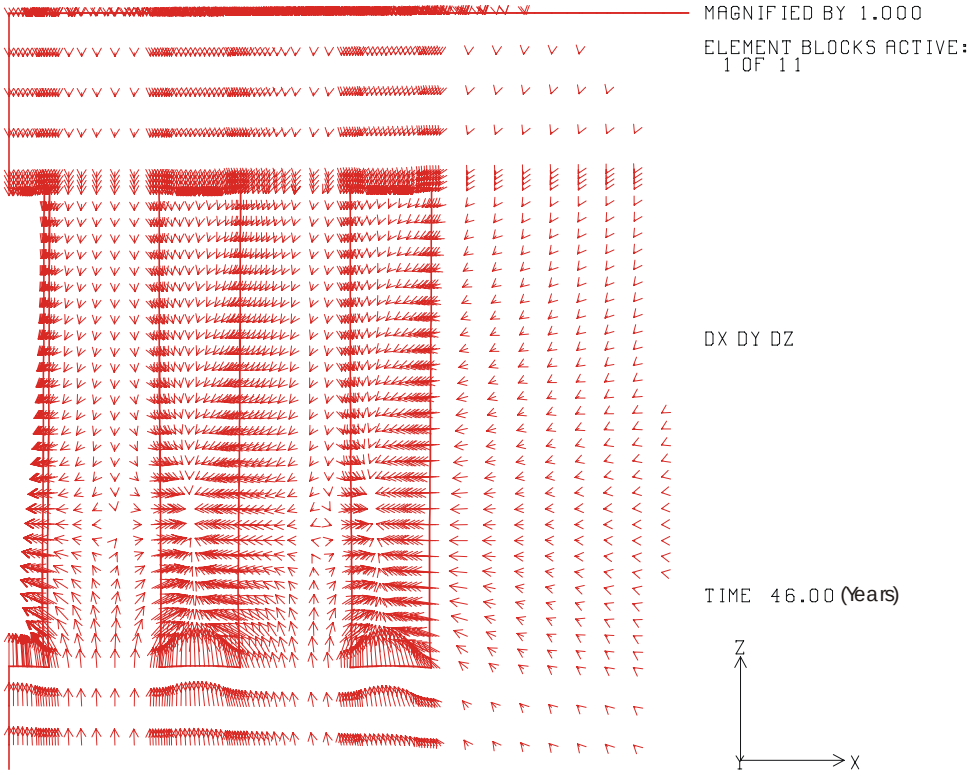

Figure 27: Displacement vectors at 46 years, immediately before the 6th leaching

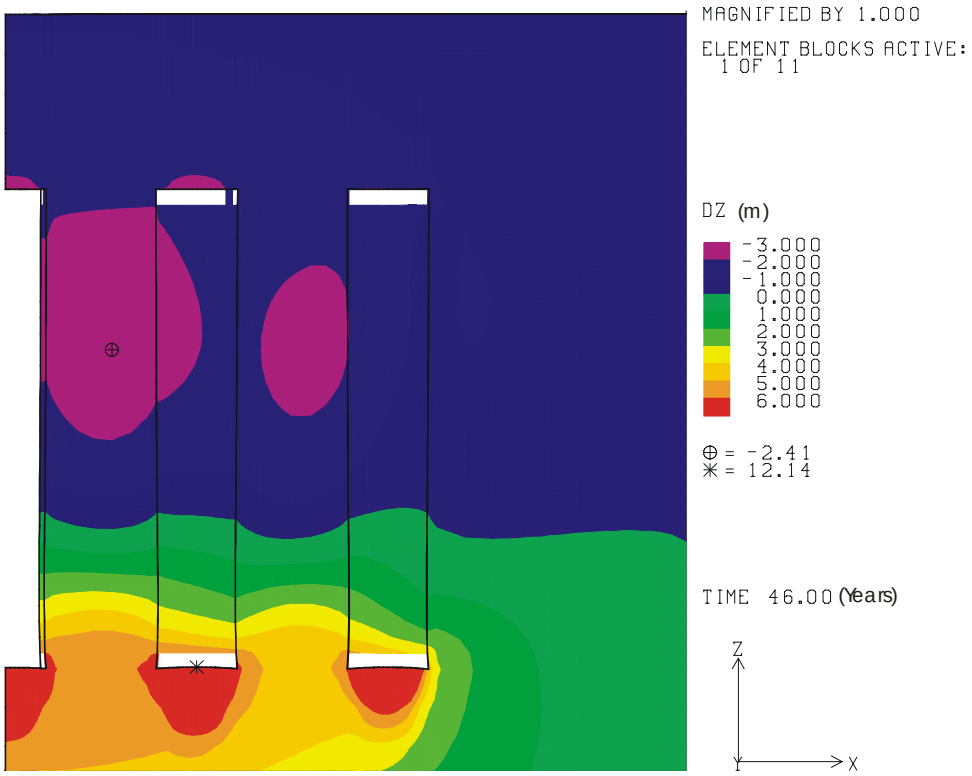

Figure 28: Vertical displacement at 46 years, immediately before the 6th leaching

8.2 Storage Loss

Figure 29 shows the decrease in overall storage volume of the cavern field over time. Because the caverns are initially leached at the beginning of the analysis, then again at 21 years, and then every 5 years thereafter, the percentage of closure is normalized by the volume immediately following each leach. The overall storage volume decreases by about 1% every 5 years. The analysis predicts that all caverns in the field close at about the same rate and the normalized rate is largely unchanged regardless of the cavern size. This suggests that the stresses controlling salt creep are similar. As discussed in Section 3.2.2, the changes in stress due to leaching quickly relax to a steady-state condition. The stress state is a strong function of the difference between the lithostatic salt stress and cavern pressure and, to a much lesser degree, by adjacent caverns since similar closure rates are predicted. The impact of workover pressures is also evident in Figure 29 by the abrupt change in normalized volumetric closure that occur each year following leaching.

Figure 30 shows the volumetric closure of each cavern normalized by the cavern volume immediately following each leach. Up until 21 years, the closure rate of cavern 3 is largest and the rates decrease in order of cavern 4, cavern 2, and cavern 1, respectively. After 21 years, the closure rates for all caverns are similar. Figure 31 shows the volume change of each cavern due to leaching and salt creep closure over time. The gold line indicates the reference value when the volume increase due to leaching only and the salt creep is not considered, as calculated in Table 8. The volume change of each cavern over time is

similar. This implies the location of cavern has little affect on the volume change due to creep closure.

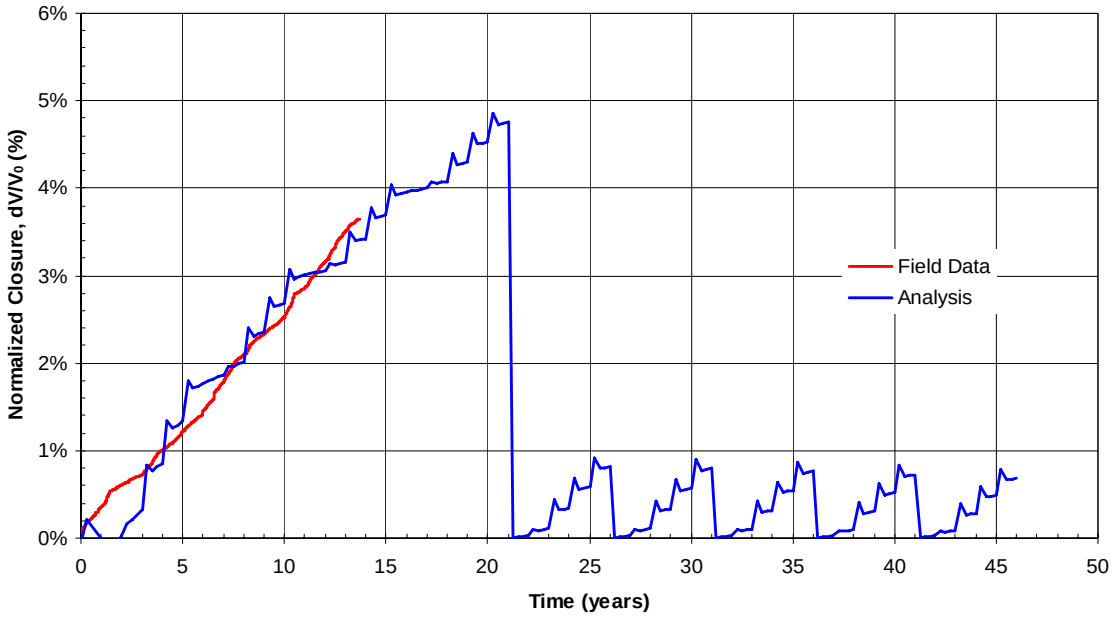

Figure 29: Overall volumetric closure normalized to overall storage volume immediately following each leach.

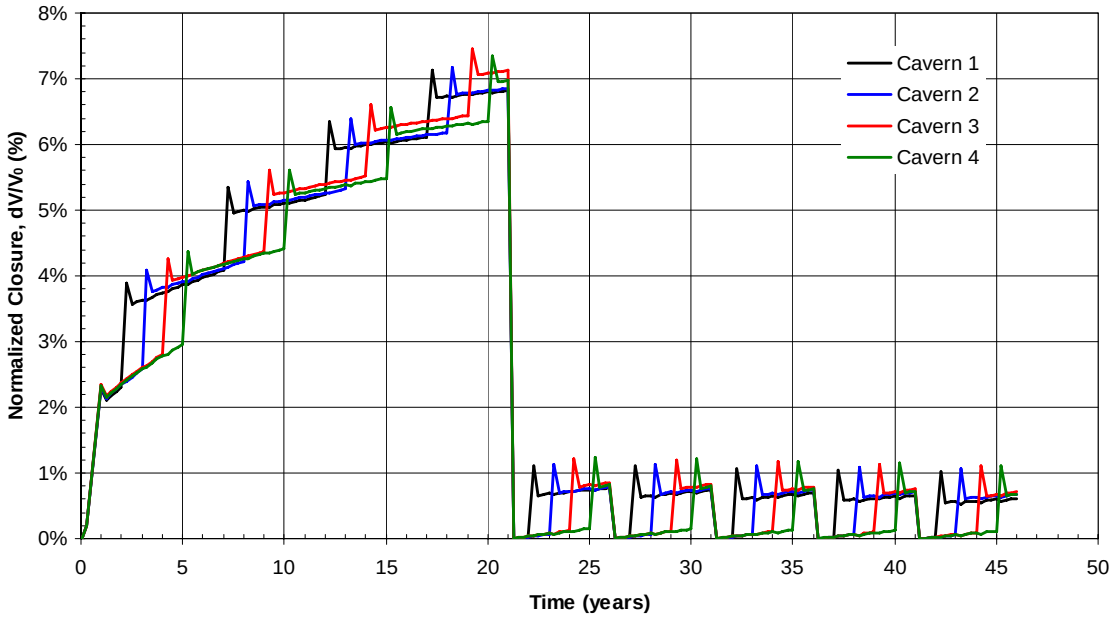

Figure 30: Volumetric closure normalized to each cavern volume immediately following each leach.

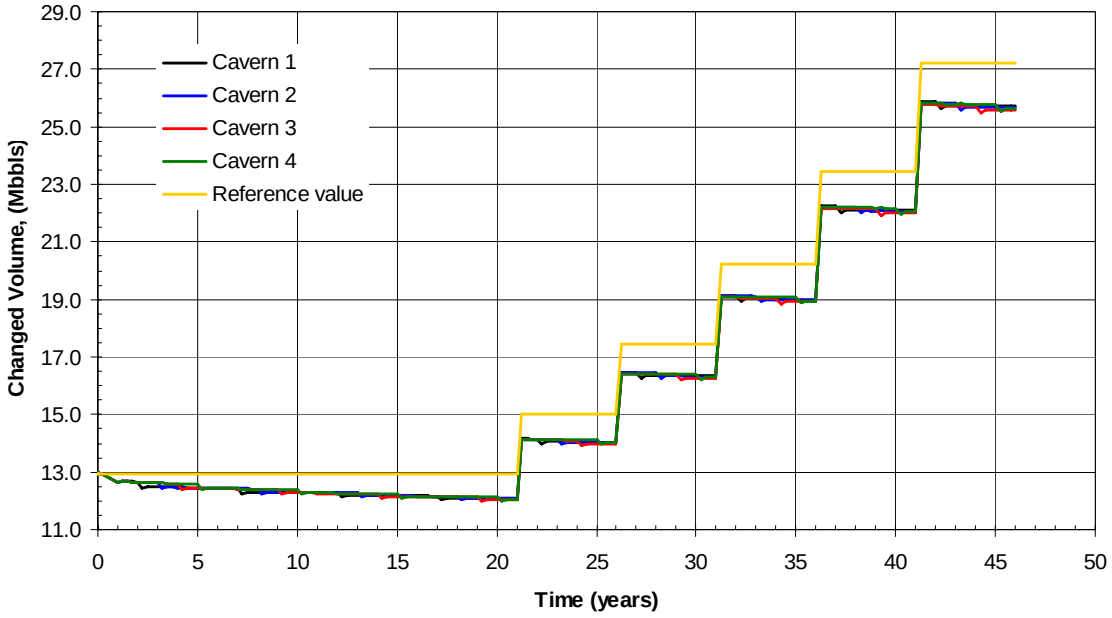

Figure 31: Volume change of each cavern due to leach and salt creep closure over time (Gold line indicates when creep closure does not occur)

8.3 Subsidence

The subsidence above the caverns is plotted as a function of time in Figure 32. The magnitude of subsidence slowly increases with time as a result of creep and cavern size. Overall, however, the subsidence rate appears to decrease slightly with time.

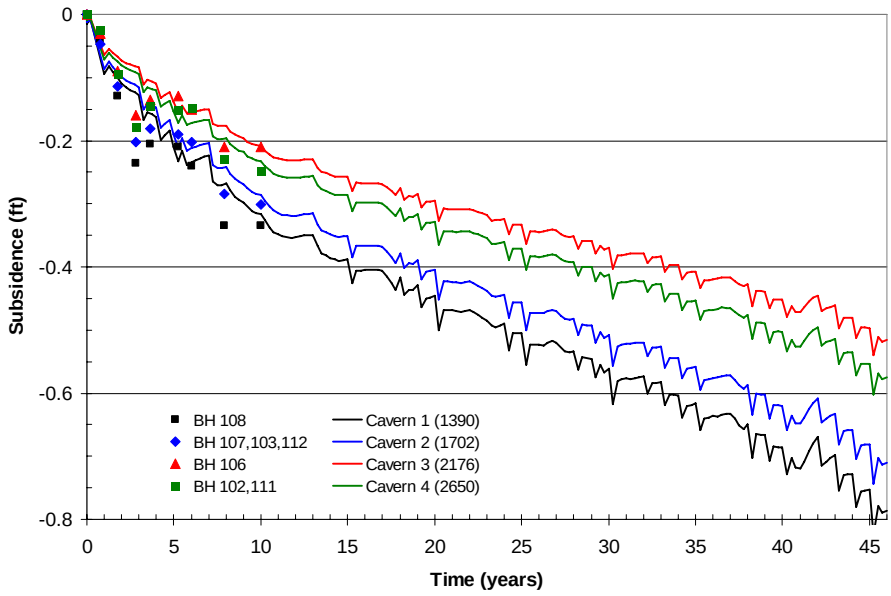

Figure 32: Predicted response (solid lines) with measured data (symbols); ( ) indicates the node numbers of the center of each cavern on the surface

Figure 33 shows the vertical ground displacements immediately before the first and after the 5th leach. The region of subsidence influence is predicted to extend to greater distances over time. The surface subsidence is similar in magnitude to that at the top of salt subsidence, but a disparity occurs near the center of the cavern field. The difference between surface and top of salt subsidence results in well strains, which are discussed in the next section, but are predicted here to be greater over the central portions of the cavern field.

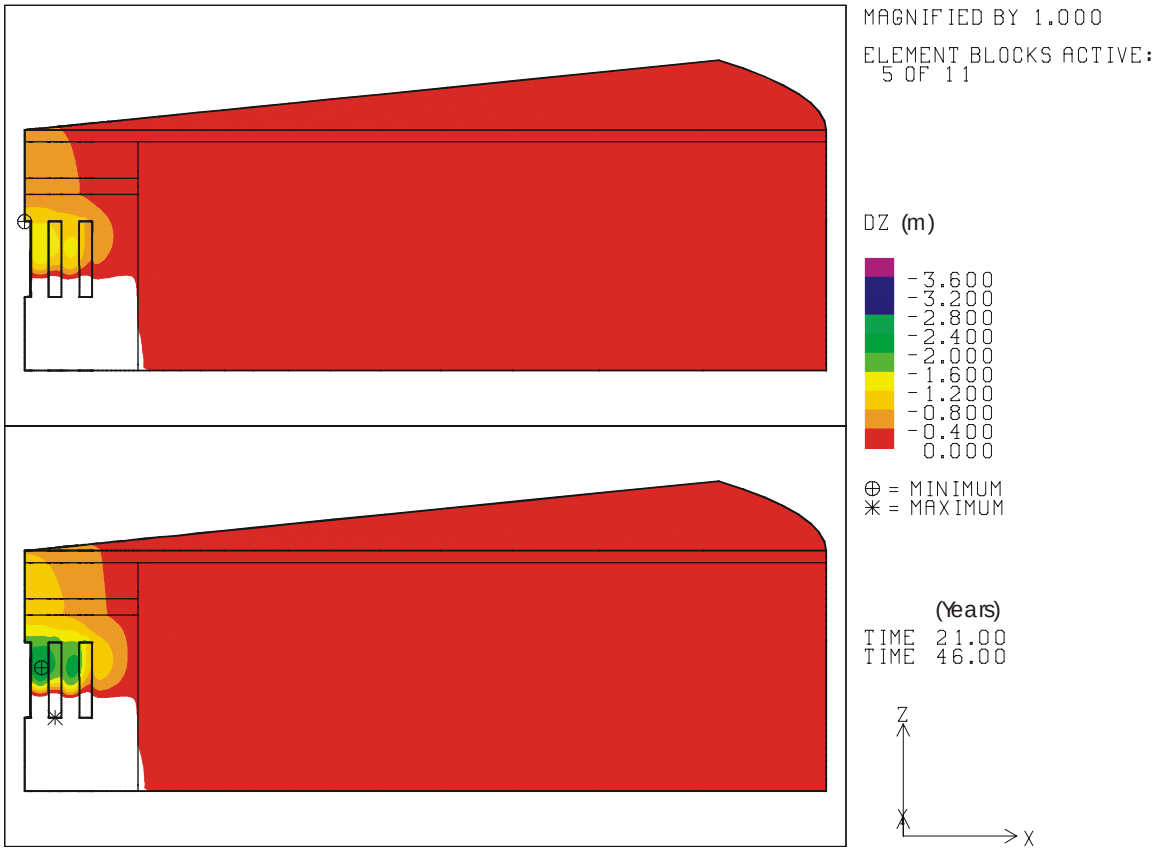

Figure 33: Vertical displacements prior to leaching (upper) and immediately before 6th leach (lower)

The calculated surface strains from the 19-cavern model at 21 years and 46 years are shown in Figure 34 for prior to the initial leach and then after the 5th leach. In comparison to the allowable 1 millistrain identified in Section 6.2, the current day accumulated strain is below the limiting value and thus preventing structural damage. After the 5th leach, the strain is also below 1 millistrain. There is not a marked increase in surface strains due to cavern enlargement. This is owed to the massive caprock above the dome. In addition, tensile strains, which can be characteristic of surface subsidence, are not predicted directly above the caverns.

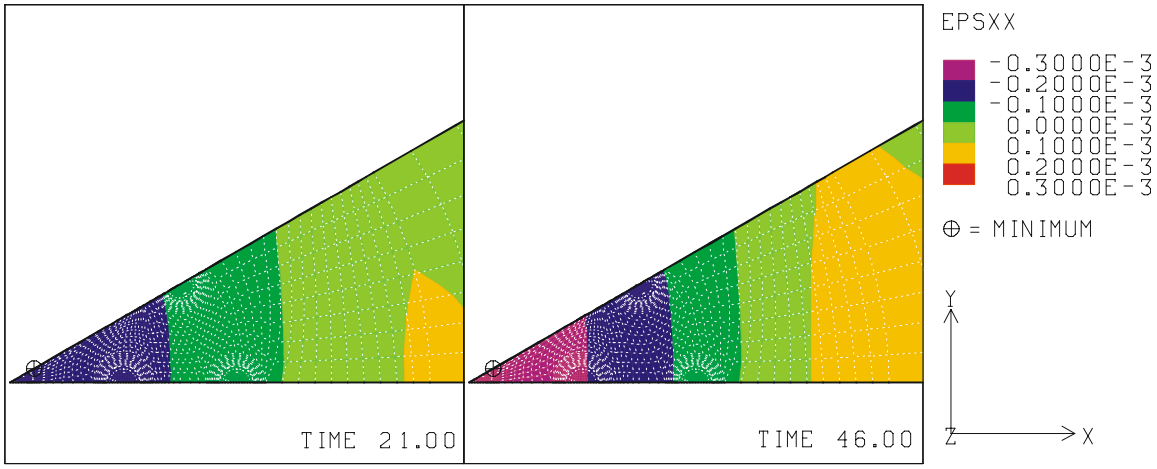

Figure 34: Predicted radial surface strains prior to leaching (left) and after the 5th leaching (right) (Time units: years)

Figure 35 shows the predicted displacement between the top of the central cavern (Cavern 1) and the surface above the cavern as a function of time. As mentioned in Section 3.2.2, the central cavern in the field is the first cavern in the workover sequence starting at one year after initial cavern leaching and continuing every 5 years until the end of the simulation. The peaks of the graph reflect the workover sequence. The subsidence rate of the top of the cavern is faster than that of the surface.

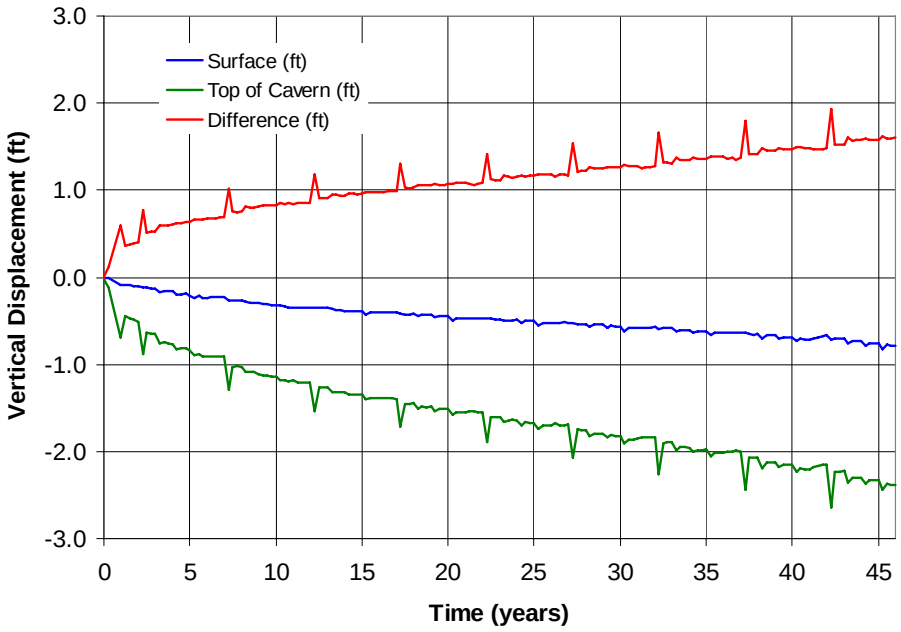

Figure 35: Predicted displacement history between surface and top of the central cavern

8.4 Cavern Wells

The calculated vertical ground strains are shown in Figure 36 at 21 years (prior to any leaching) and after the 5th leach. Of interest are the magnitudes in the location of the cav-

ern wells. As discussed in Section 6.2, axial strains in the well will reduce the collapse pressure of the casing(s) and yielding is predicted after 2 millistrains. The predicted strain at 21 years is less than yield, with a possible exception near the bottom of the deepest cemented casing. This is typically about 100 ft above the cavern roof. Yielding of the casing in the salt may be of little consequence since creep of salt will control the deformation. The creep rate will be very small and less than that in the cavern due to the backpressure the casing exerts on the salt and the relatively shallow depth of the casing in salt. Higher strains are found after 5 cavern leaches when subsidence at the surface above the central cavern is predicted at approximately 0.8 ft.

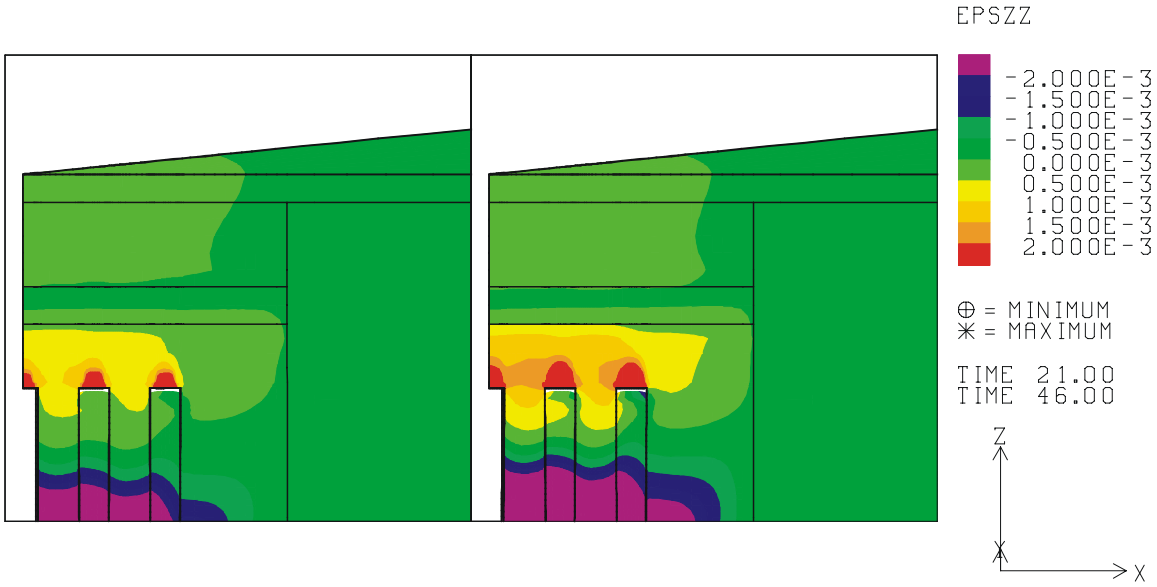

Figure 36: Vertical ground strains near cavern wells prior to leaching (left) and after the 5th leaching (right) (Time units: years)

8.5 Cavern Stability

As discussed in Section 6.1, the stability of the caverns was evaluated by examination for any tensile stresses and calculation of the safety factor against dilatant damage.

8.5.1 Minimum compressive stress

The minimum compressive stress that was found after 5 leaches is 5.56 MPa, as shown in Figure 37. The most critical location was calculated in the roof of the caverns at 44.25 years and 45.25 years. Figure 38 shows the minimum compressive stress history. The minimum compressive stress is calculated to be 4.83 MPa at 4.25 years which is before 1st leach. All stresses are lower than the tension limit, 0 MPa. Thus the caverns are structurally stable against tensile failure throughout the entire simulation time.

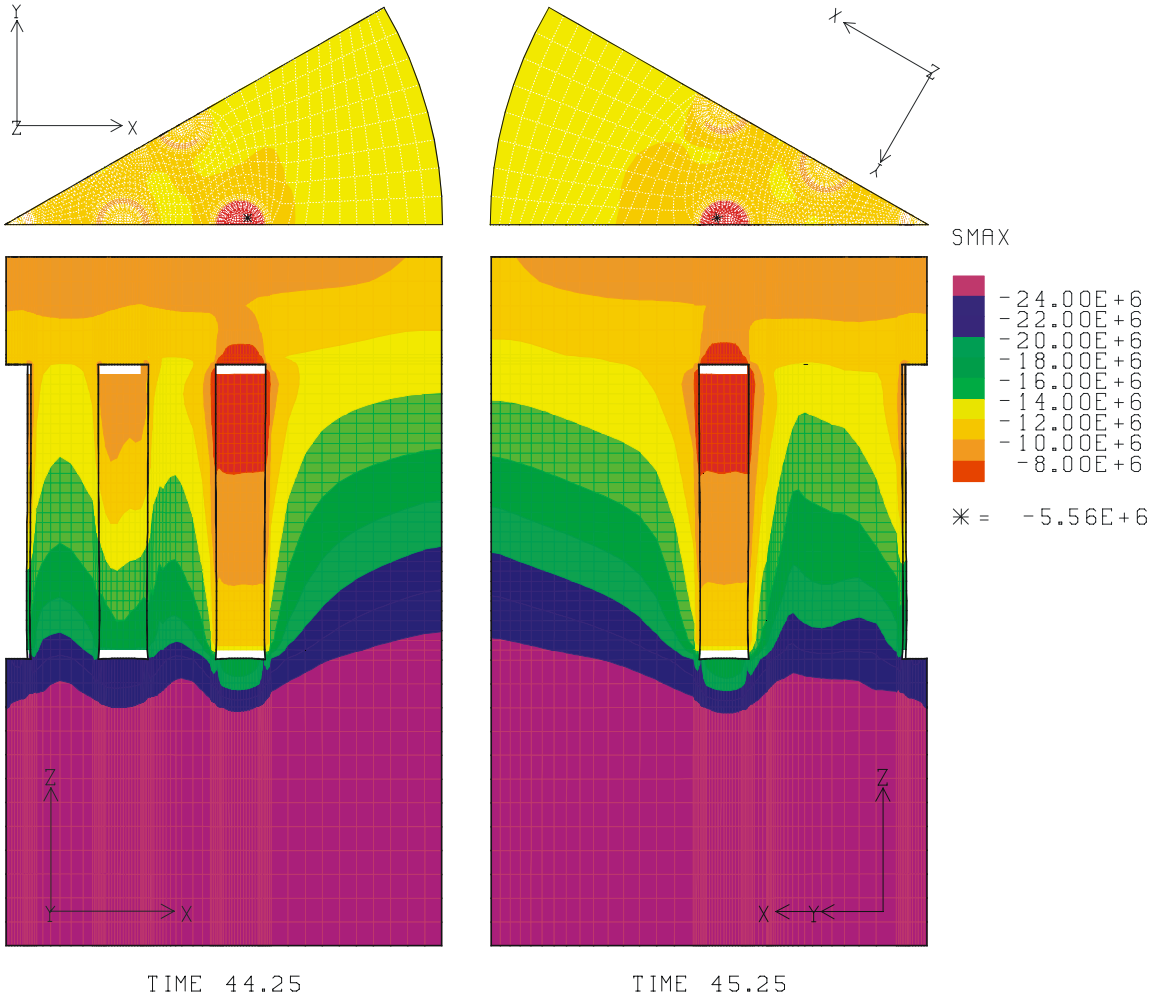

Figure 37: Least compressive stress contour at 44.25 years and 45.25 years (horizontal cross-section at the roof elevation) (units: Pa, years)

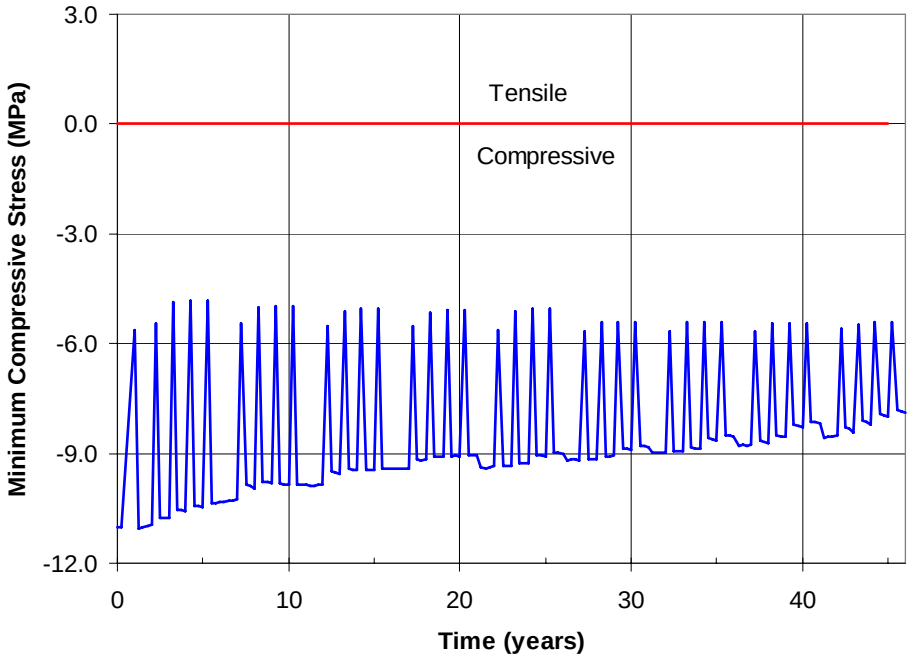

Figure 38: Minimum compressive stress as a function of time

8.5.2 Minimum safety factor against dilatant damage

Examinations of a typical safety factor distribution for dilatant damage over the cavern surface are provided in Figure 39, Figure 40, and Figure 41 for various times in the caverns along the two symmetry planes at 0° and 30° before the 6th leaching. These figures show effects of workovers as discussed in Section 3.2.2.

The conventional dilatancy criterion of Equation (7) in Section 6.1 is used. The dilatant failure potentially occurs in the contour where DILFAC (dilatant damage factor) is less than 0.6. Areas where DILFAC is less than 0.6 do not exist, thus the dilatant failure is not expected to occur. The lowest safety factor is predicted at the wall of the caverns, near the roof.

The lowest safety factor for dilatancy is plotted in Figure 42 over time. The influence of workovers is noted by the drops in safety factor from 5.5 to approximately 1.7. Similar to the tensile damage, all dilatancy safe factors are higher than failure limit, 0.6, thus all caverns are structurally stable against dilatant failure over time up through the 5th leaching. An interesting observation is the lowest safety factor, and hence the greatest potential for damage, occurs near the roof of the cavern.

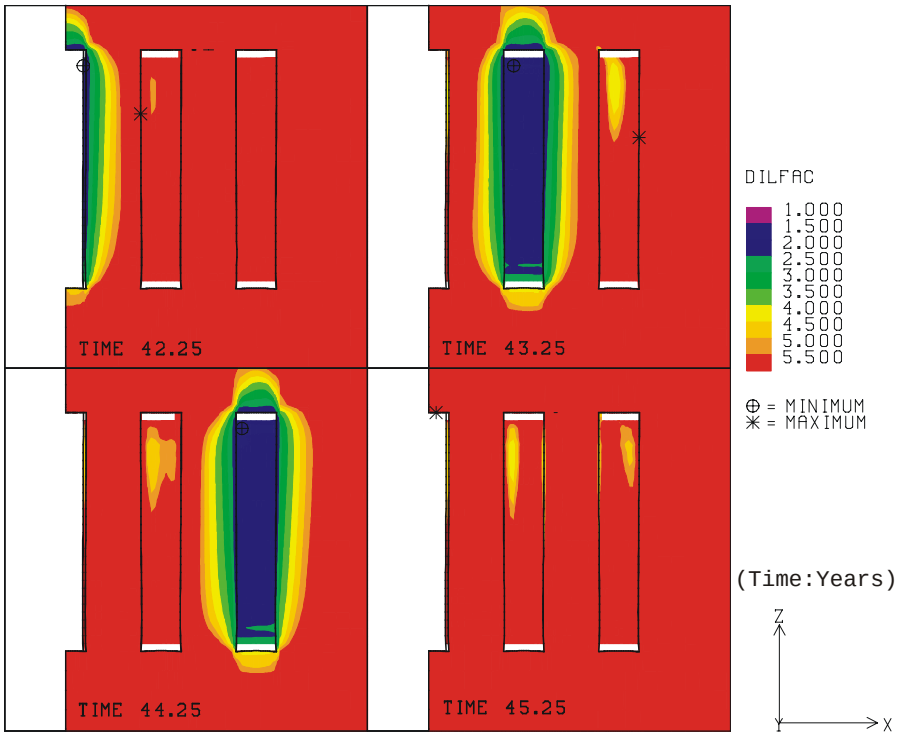

Figure 39: Safety factor contours against dilatant damage during workover of each cavern before the 6th leaching by conventional criterion (Cavern 1, 2, and 3)

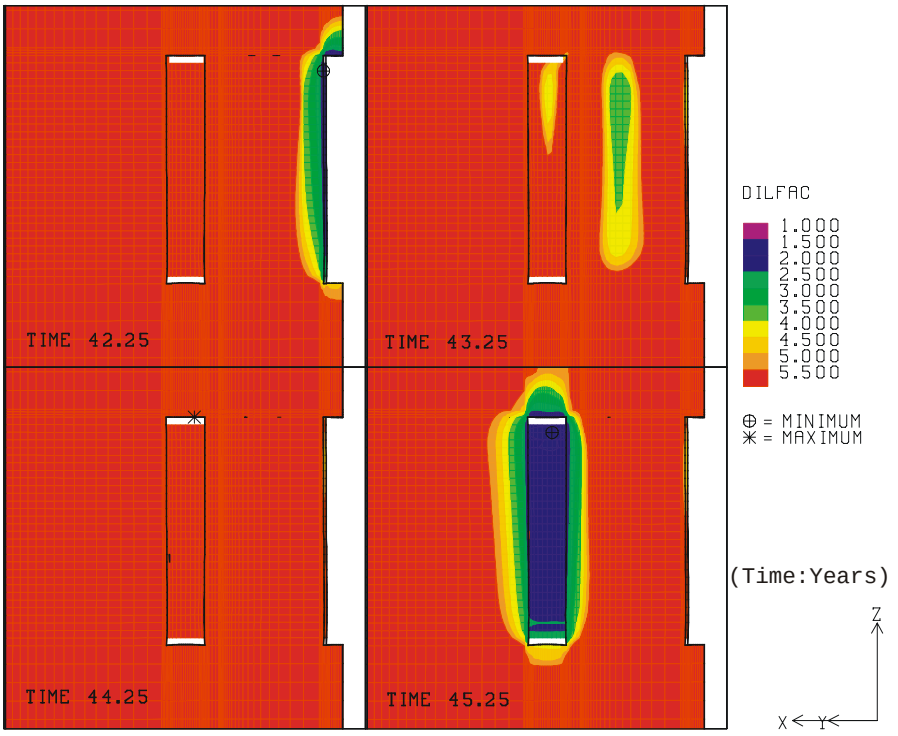

Figure 40: Safety factor contours against dilatant damage during workover of each cavern before the 6th leaching by conventional criterion (Cavern 1, 4)

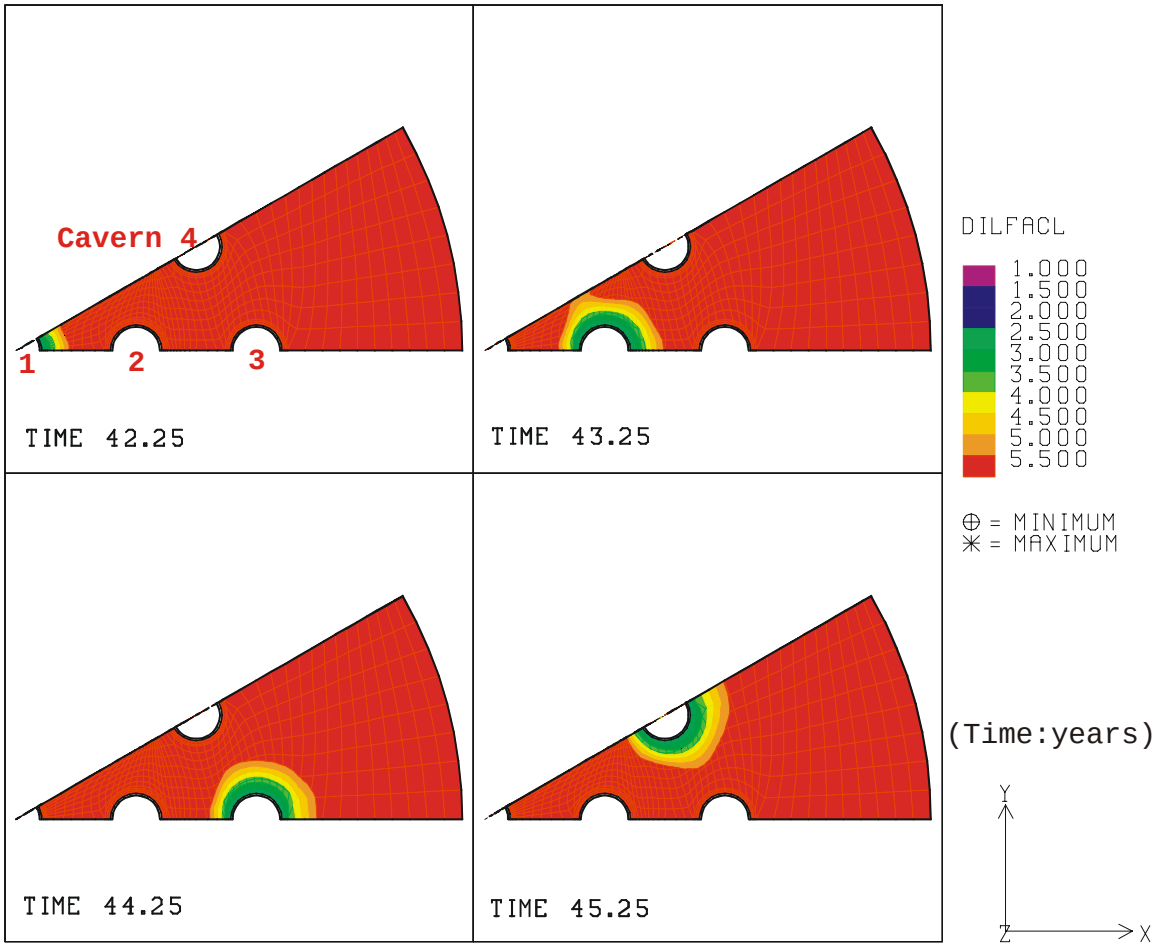

Figure 41: Safety factor contours against dilatant damage during workover of each cavern before the 6th leaching by conventional criterion (Plan view at the level of cavern roof)

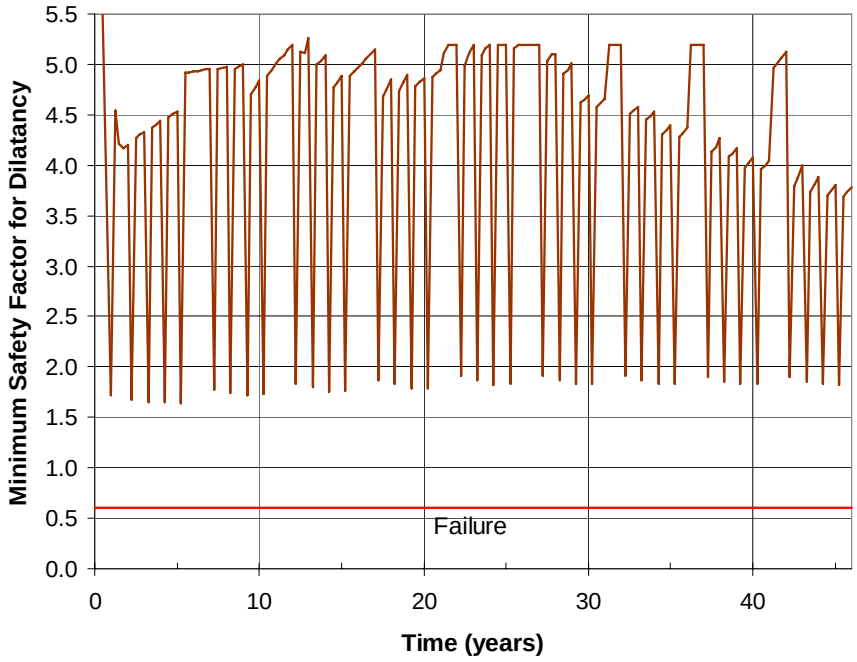

Figure 42: Minimum safety factor against dilatant damage by conventional criterion

8.5.3 Dilatant safety factors by Lee's criterion

Figure 43, Figure 44, and Figure 45 show the contours of dilation safety factor in the modeled cavern walls according to Lee's criterion, Equation (8) in Section 6.1. In comparison to Figure 39, Figure 40 and Figure 41, the contour area appears broader, especially near the floor of the caverns. The lowest safety factor by Lee's criterion is predicted at the wall of the caverns, also near the floor, rather than the roof in the case of the conventional criterion.

The lowest safety factor for damage by Lee's criterion is plotted in Figure 46 as a function of time. All dilatancy safety factors given by Lee's criterion are higher than failure limit, 1.0, thus all caverns are structurally stable against dilatant failure over time up through 5th leaching.

In comparison to Figure 42, the safety factors according to Lee's criterion are larger than the failure limit, 1.0. However, considering failure limit by the conventional criterion is 0.6, the differences between the limit and the lowest safety factor for the conventional and Lee's criterion are almost the same. In other words, the dilatant potentials predicted by both criteria are similar.

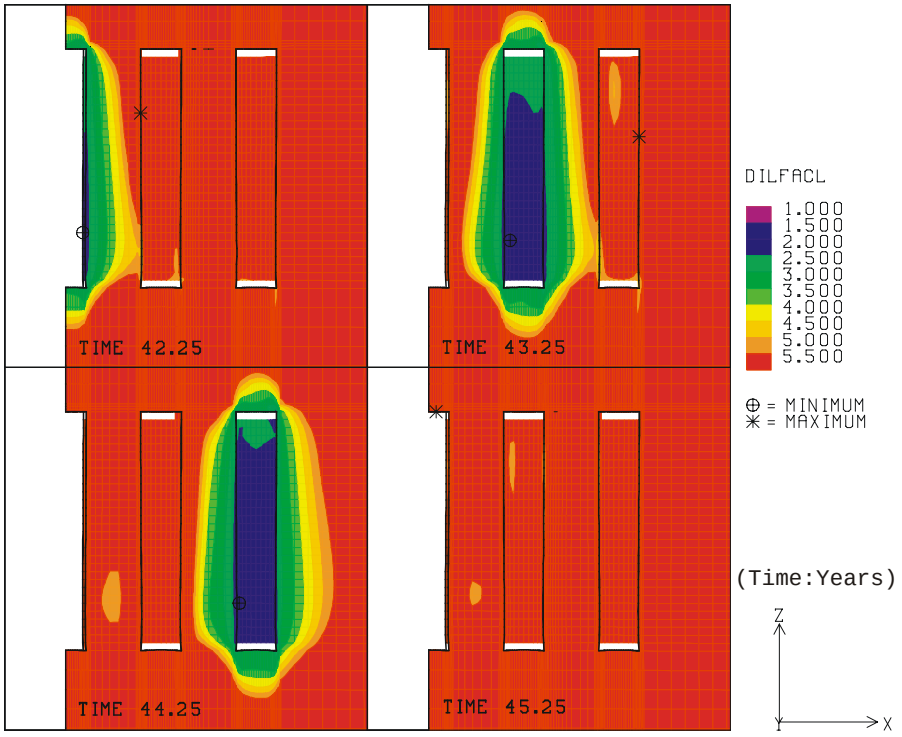

Figure 43: Safety factor contours against dilatant damage during workover of each cavern before the 6th leaching by Lee's criterion (Cavern 1, 2, and 3)

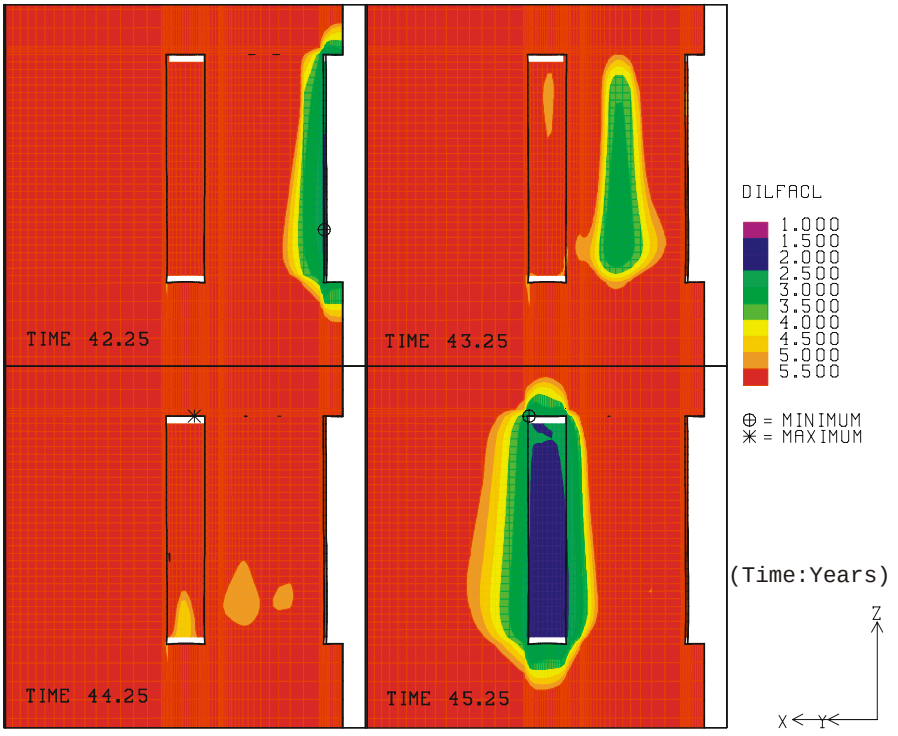

Figure 44: Safety factor contours against dilatant damage during workover of each cavern before the 6th leaching by Lee's criterion (Cavern 1 and 4)

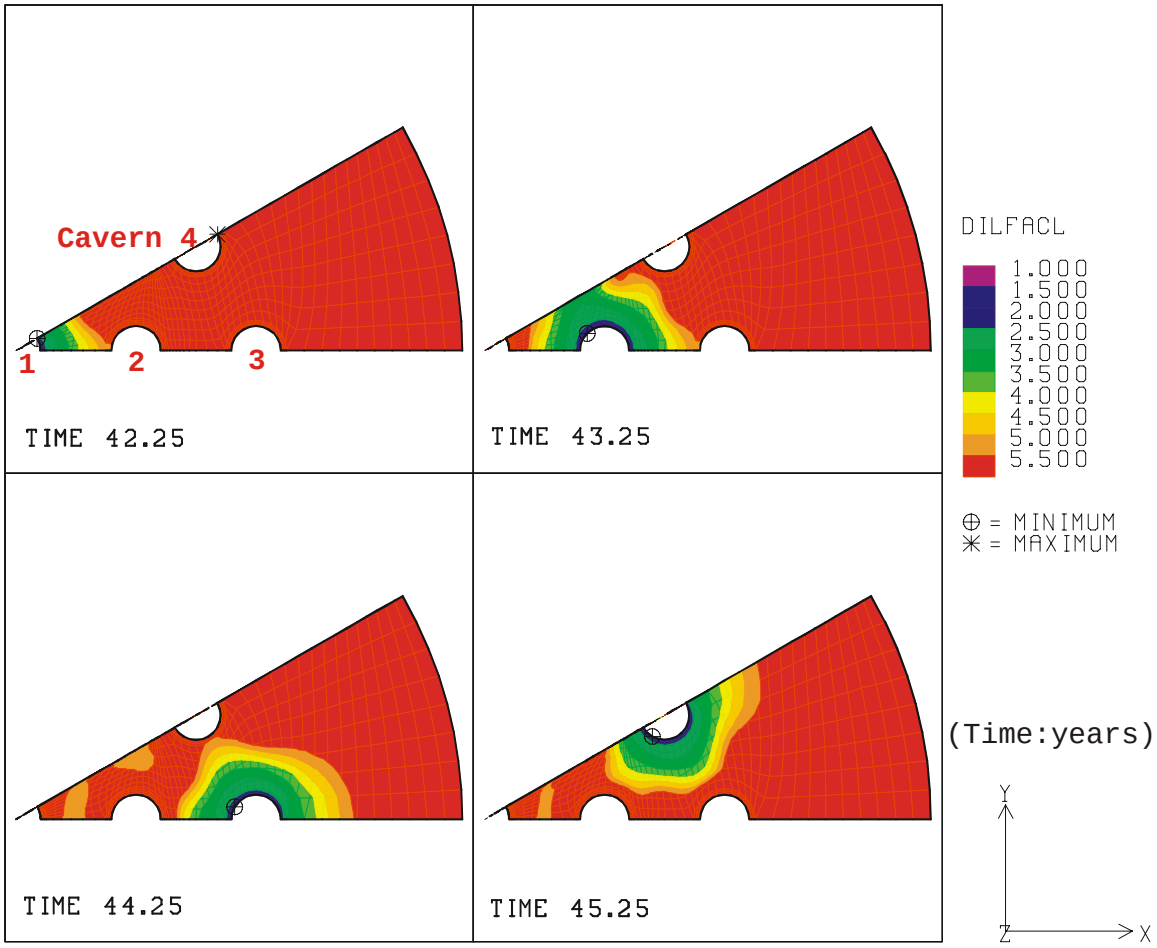

Figure 45: Safety factor contours against dilatant damage during workover of each cavern before the 6th leaching by Lee's criterion (Plan view at the level of minimum SF, -3734 ft)

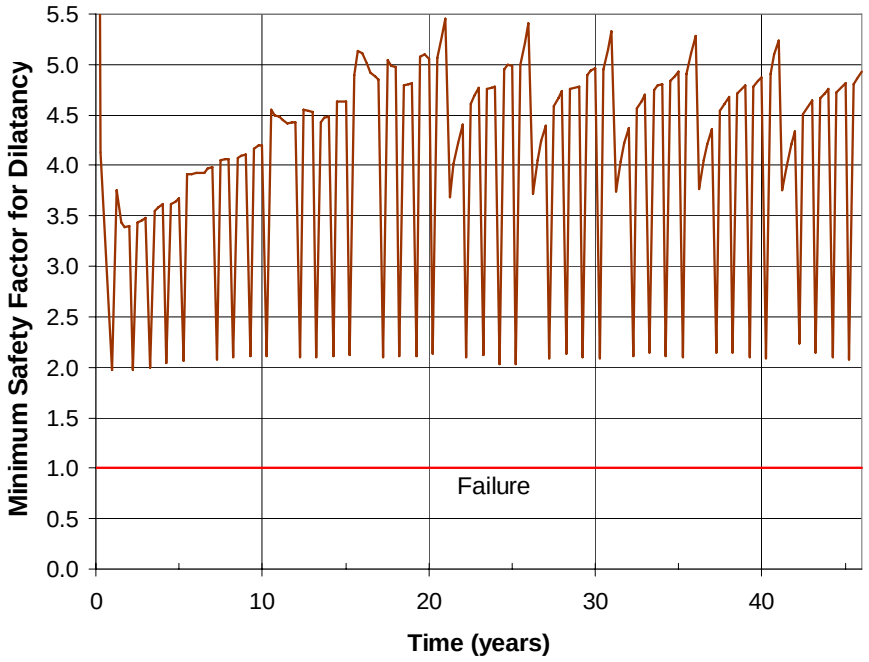

Figure 46: Minimum safety factor against dilatant damage by Lee's dilation criterion

9 STANDOFF DISTANCE EFFECT

9.1 Objectives

The standoff distance (SD) is the key parameter for checking the structural integrity of the caverns in the dome. If the salt forms cracks or fractures due to unstable stresses, the oil might be released to the porous sandstone. The formation of these cracks is defined as the failure. To estimate how many more caverns can be constructed in the existing salt dome, it is necessary to define the allowable SD for a cavern to the edge of the dome based on mechanical integrity of the salt and cavern. From this analysis, it is possible to evaluate whether of not some of the existing caverns are at risk or already have been compromised, and the criteria for SD will be heavily weighed in future decisions by DOE.

9.2 Cavern Layout

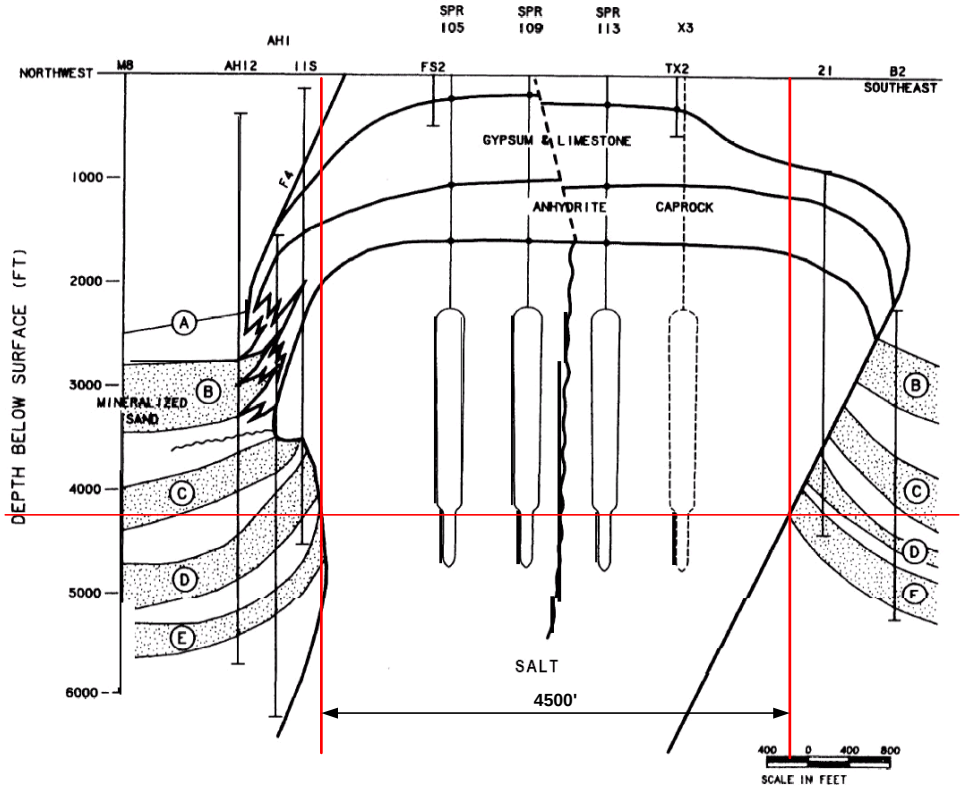

Figure 47: Determination of the minimum diameter of salt dome for modeling

Figure 47 shows a Northwest-Southeast cross section view from which the minimum diameter of the dome in the model is determined. This cross section is the smallest width of the dome, and is selected for the conservative analysis. The minimum diameter used to model the dome in the Finite Element Method (FEM) analysis is 4,500 ft.

As discussed in Section 3.2.1, expansion opportunities consider the addition of five caverns to the existing 14 cavern field, and potentially more if land is acquired in the northern portion of the dome. Therefore two meshes are defined; one that contains 19 caverns and another that contains 31 caverns. Because symmetry is invoked to simplify modeling, both meshes are approximations of any future cavern field geometry. As described in Section 5, the 19-cavern model is used to determine the values of unmeasured parameters in the field. The results from the 19-cavern model are used as the reference to compare with the results from the 31-cavern model with various SDs.

Figure 48 and Figure 49 show the 31-cavern model layout with various dome sizes to determine the effect of SD. The SD is defined as the distance from the center of an outmost cavern to the dome edge. The structural integrity will be checked for SDs of 266 ft, 500 ft, 800 ft, and 1200 ft for the 31-cavern model. This corresponds to dome diameters of 4500 ft, 4969 ft, 5569 ft, and 6369 ft respectively. The 266 ft SD is determined from the minimum dome diameter as indicated in Figure 47.

This model is for generalized cases including BH. Thus the actual size of salt dome at BH is ignored. In other words, in the case of SD=1200 ft, the diameter of the dome is larger than that actually at BH. However, because the BH salt dome is not an exact circle but variable, the simulation results may be applicable where a cavern may have a local SD of 1200 ft. Also, this simulation results could be applied to other sites which have similar lithologies and larger dome sizes than BH. The 19-cavern model, which SD is 1284 ft, is used as the reference.

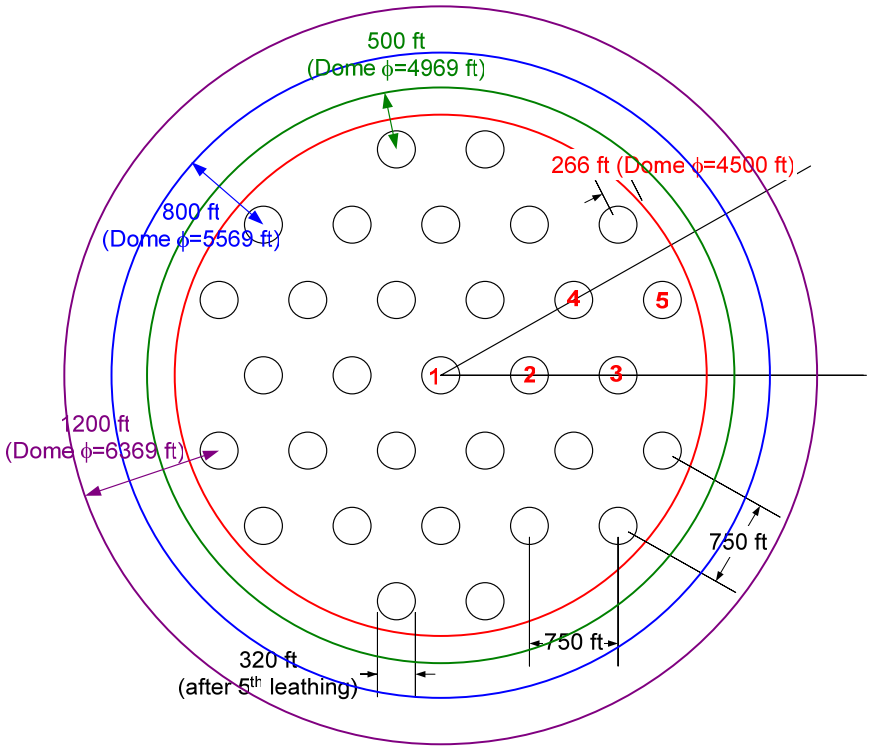

Figure 48: 31-Cavern model layout with various dome size

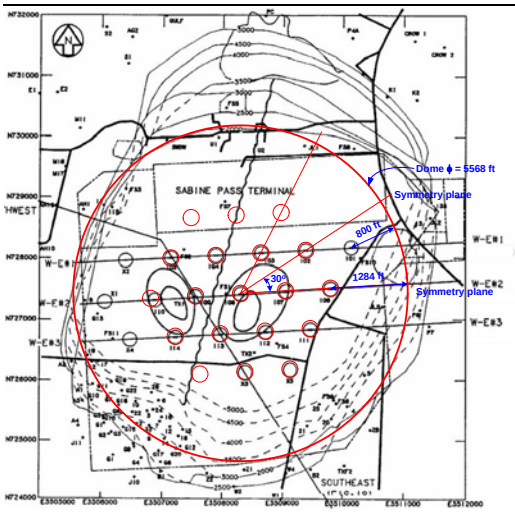

(a) 19-cavern, SD=1284 ft

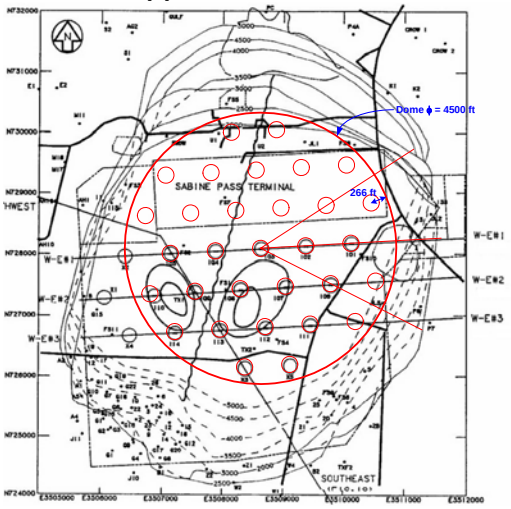

(b) 31-cavern, SD=266 ft

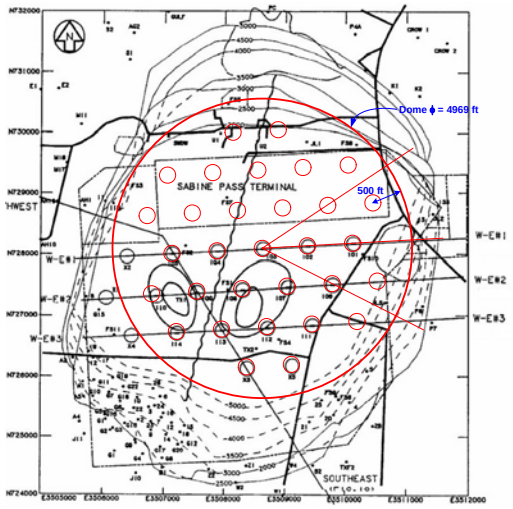

(c) 31-cavern, SD=500 ft

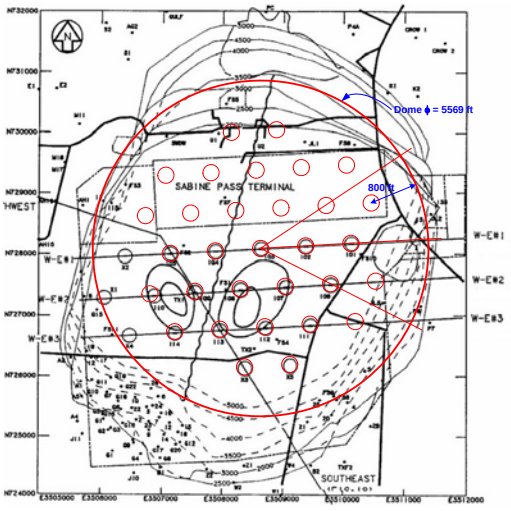

(d) 31-cavern, SD=800 ft

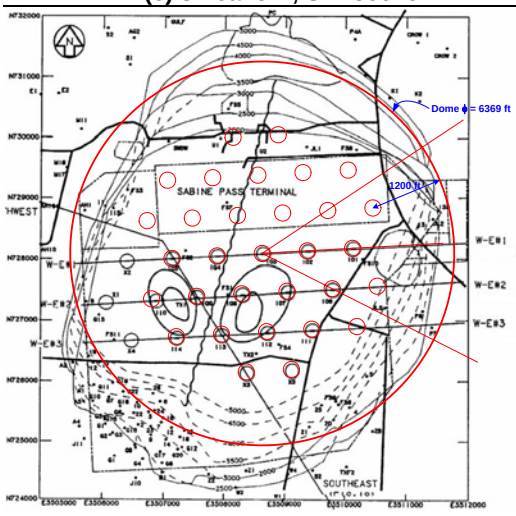

(e) 31-cavern, SD=1200ft

Figure 49: 19-cavern layout and 31-cavern layouts with SD

9.3 Model History

As mentioned in 3.2.2, the caverns undergo workover every five years and not all caverns are in workover mode at the same time. The central cavern is the first cavern in the workover sequence starting at one year after initial cavern leaching and continuing every 5 years until the end of the simulations. The next cavern to undergo workover is Cavern 2 (Figure 48). Because of mesh symmetry, workover pressures must be applied to this entire second set of caverns at the same time. This results in 6 caverns at low pressure starting one year after each workover of the Cavern 1. The workover sequence continues with the third set of caverns consisting of Caverns 3 and 4 (Figure 48) being subject to workover pressures one year after the second set. The last set of caverns to undergo workover, in the fourth year of the cycle, is that set which includes Cavern 5 (Figure 48). The difference from the 19-cavern model is that Cavern 4 is regarded as being in the third set of caverns with Cavern 3 and Cavern 5 is regarded as being in the fourth set.

9.4 Mesh

Figure 50 shows the mesh and boundary condition for the 31-cavern, 5-leach model. The model simulates 31 caverns in a systematic pattern with equal spacing and uniform cavern size and geometry. The 31-cavern model consists of 85,609 nodes and 78,068 elements for the 266 ft SD.

The thicknesses of each layer and the radius of the model are the same as those of the 19-cavern model. Five material blocks are used in the model for the overburden, caprock 1, caprock 2, salt dome, and the lithology surrounding the salt dome as the 19-cavern model. The structural integrity will be check by increasing the SD from 266 ft to 1200 ft.

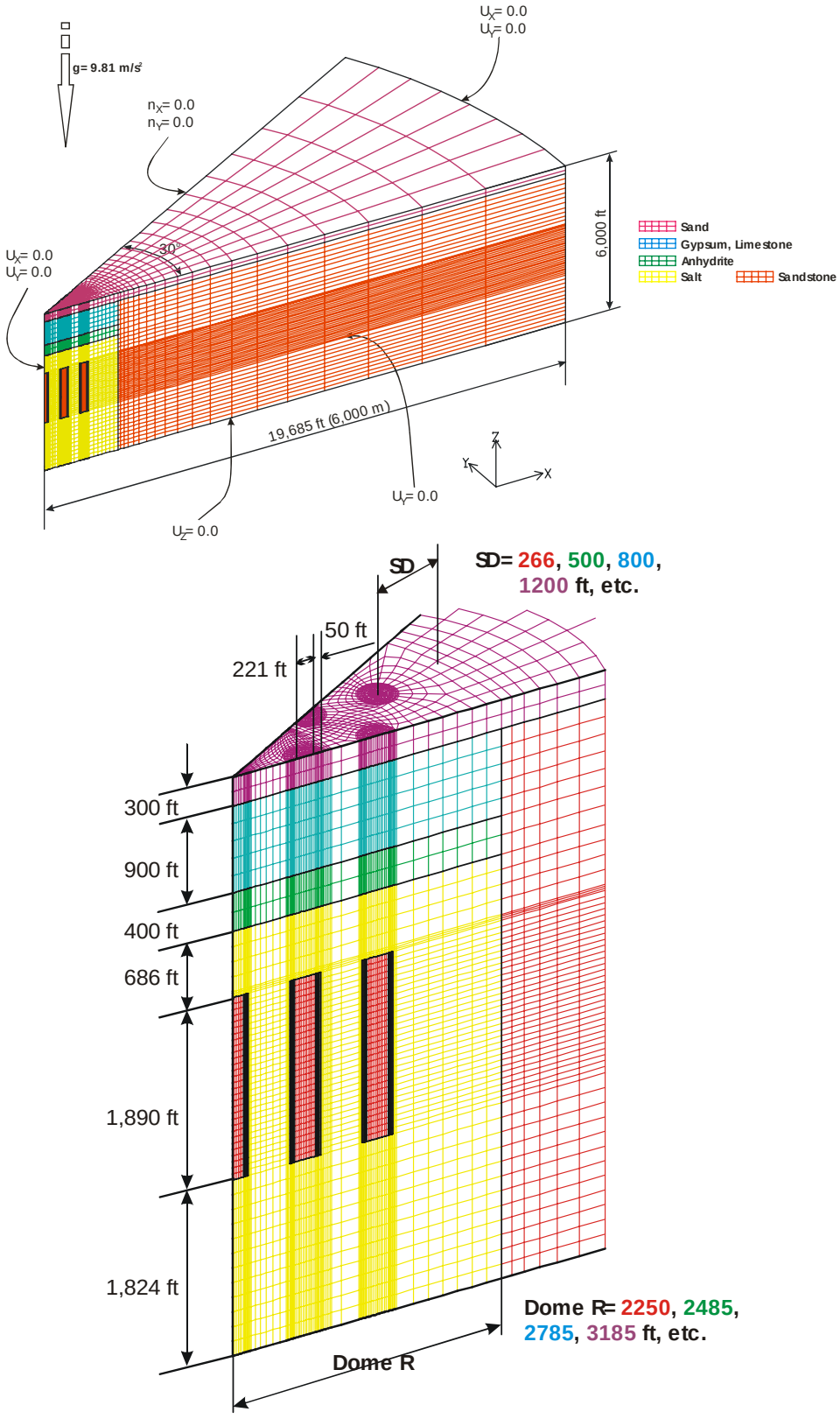

Figure 50: Mesh discretization and boundary conditions for 31 caverns and 5 leach simulation

9.5 Analysis Prediction

9.5.1 Storage loss

Figure 51 shows the decrease in storage volume of the cavern field over time with SD. A shorter SD yields smaller decrease in storage volume. The surrounding lithology contributes to reduce the creep closure because the surrounding rock behaves as a rigid cylindrical frame.

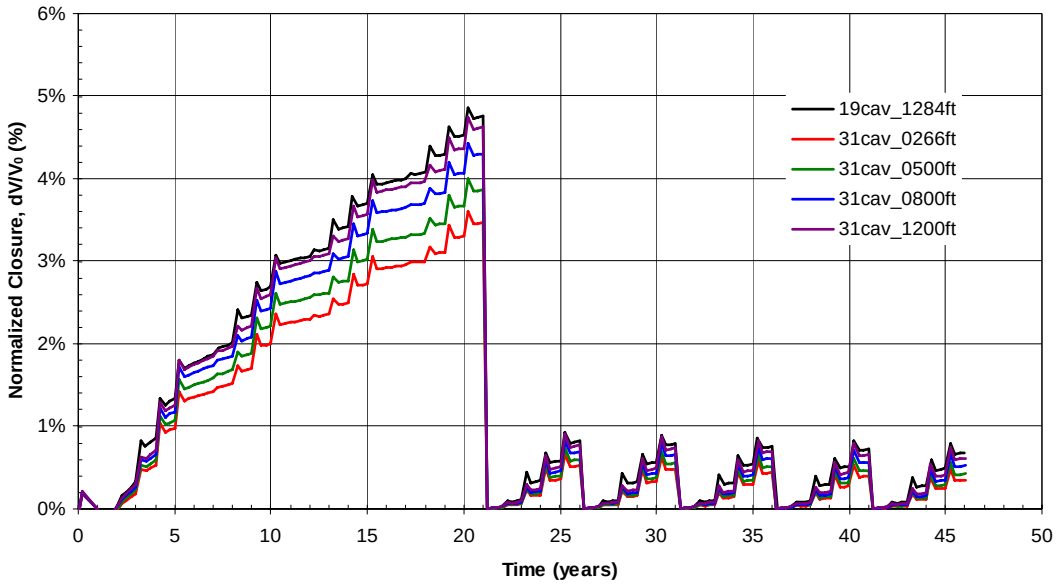

Figure 51: Normalized volumetric closure with standoff distance

9.5.2 Subsidence

Figure 52 and Figure 53 show the predicted surface subsidence troughs with SD as a function of distance from the center of the dome at 5 years and 10 years, respectively. A larger SD yields a larger subsidence. In the case of 800 ft SD, the size of dome is the same as 19-cavern model. However subsidence is much larger than the case of 19-cavern model because subsidence is a function of the number of caverns underground.

Figure 54 shows the average predicted subsidence histories at the surface above each cavern with SD. The subsidence at the surface above Cavern 5 is not included so as to facilitate comparison with 19-cavern model. Again, a larger SD also yields a larger subsidence with time.

The calculated surface strains at 46 years for each SD are shown in Figure 55. In comparison to the allowable 1 millistrain discussed in Section 6.2, the accumulated strain is below the limit and thus structural damage on surface should not occur.

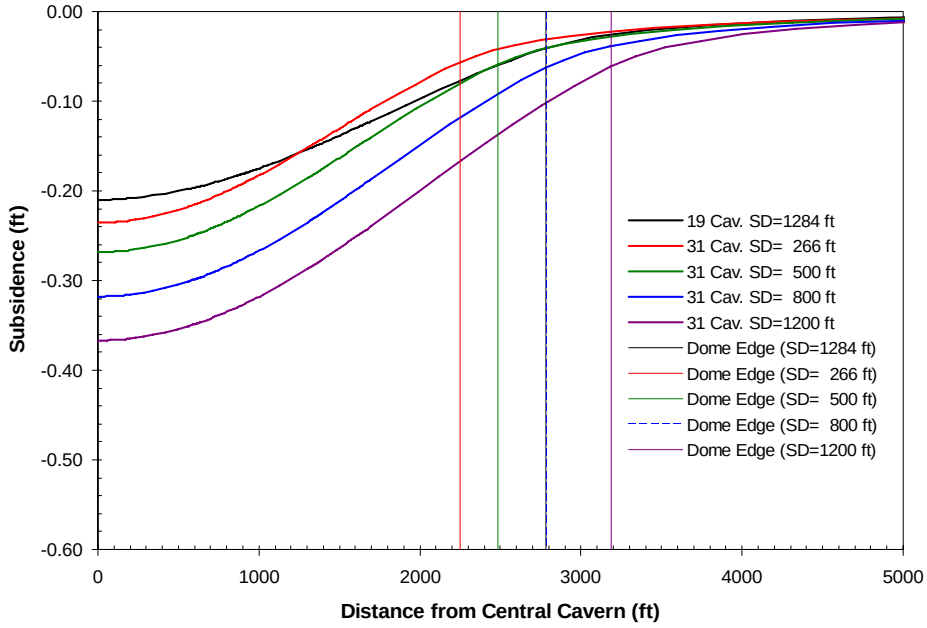

Figure 52: Predicted surface subsidence as a function of distance from the center of dome at 5 years with SD

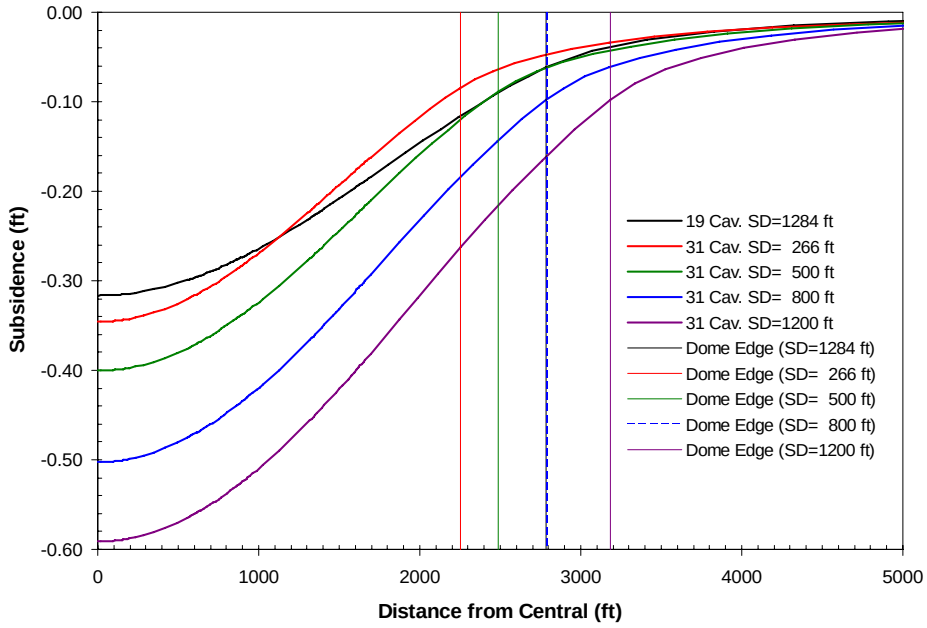

Figure 53: Predicted surface subsidence as a function of distance from the center of dome at 10 years with SD

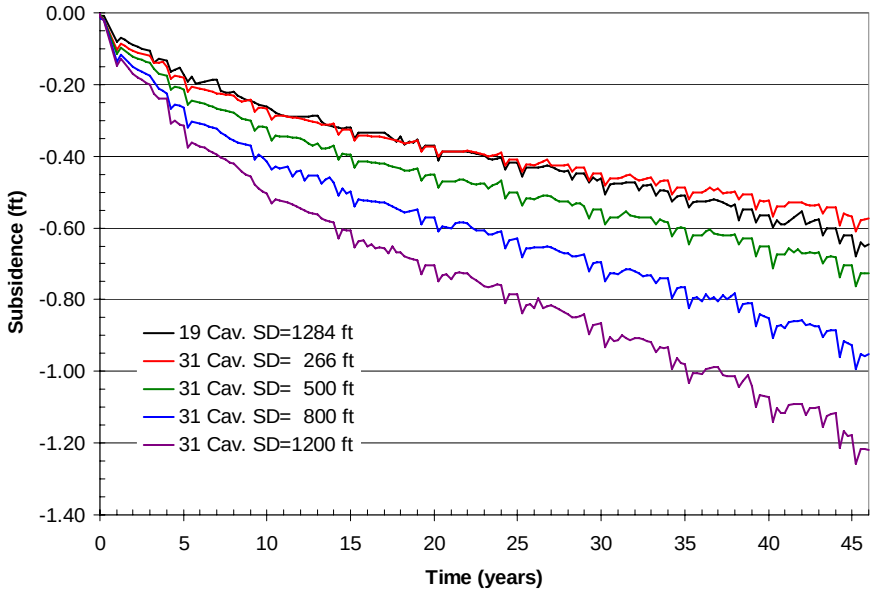

Figure 54: Average predicted subsidence at the surface above each cavern with SD

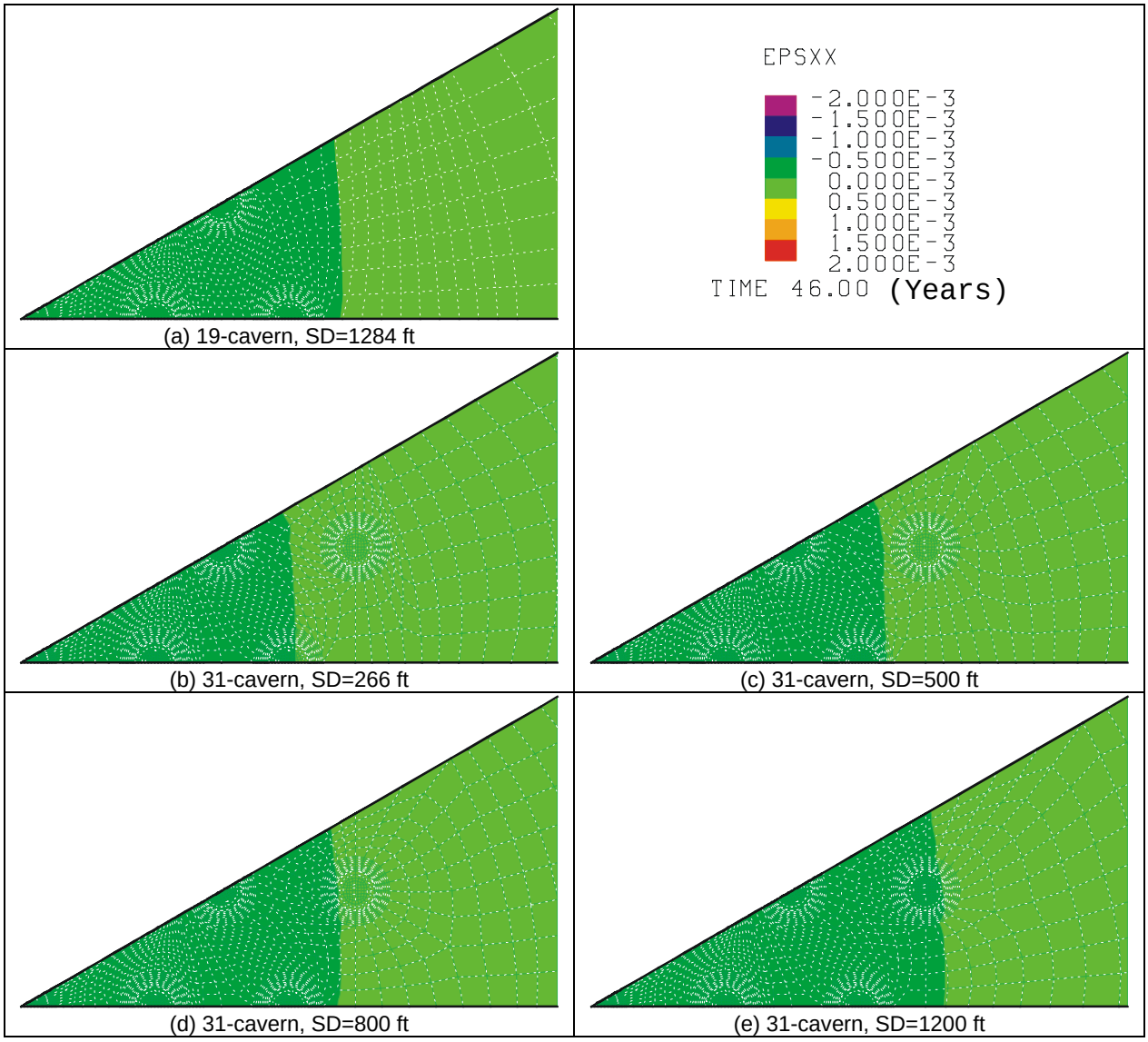

(a) 19-cavern, SD=1284 ft

(b) 31-cavern, SD=266 ft

(c) 31-cavern, SD=500 ft

(d) 31-cavern, SD=800 ft

(e) 31-cavern, SD=1200 ft

Figure 55: Predicted radial surface strains after the 5th leaching with SD

9.5.3 Cavern wells

Figure 56 shows the vertical ground strains near cavern wells after the 5th leach for each SD. As discussed in Section 6.2, yield is predicted after 2 millistrain. All cases show yielding occurring at the tops of the caverns. In the case of the shortest SD (266 ft), the yield zone is wider than other cases.

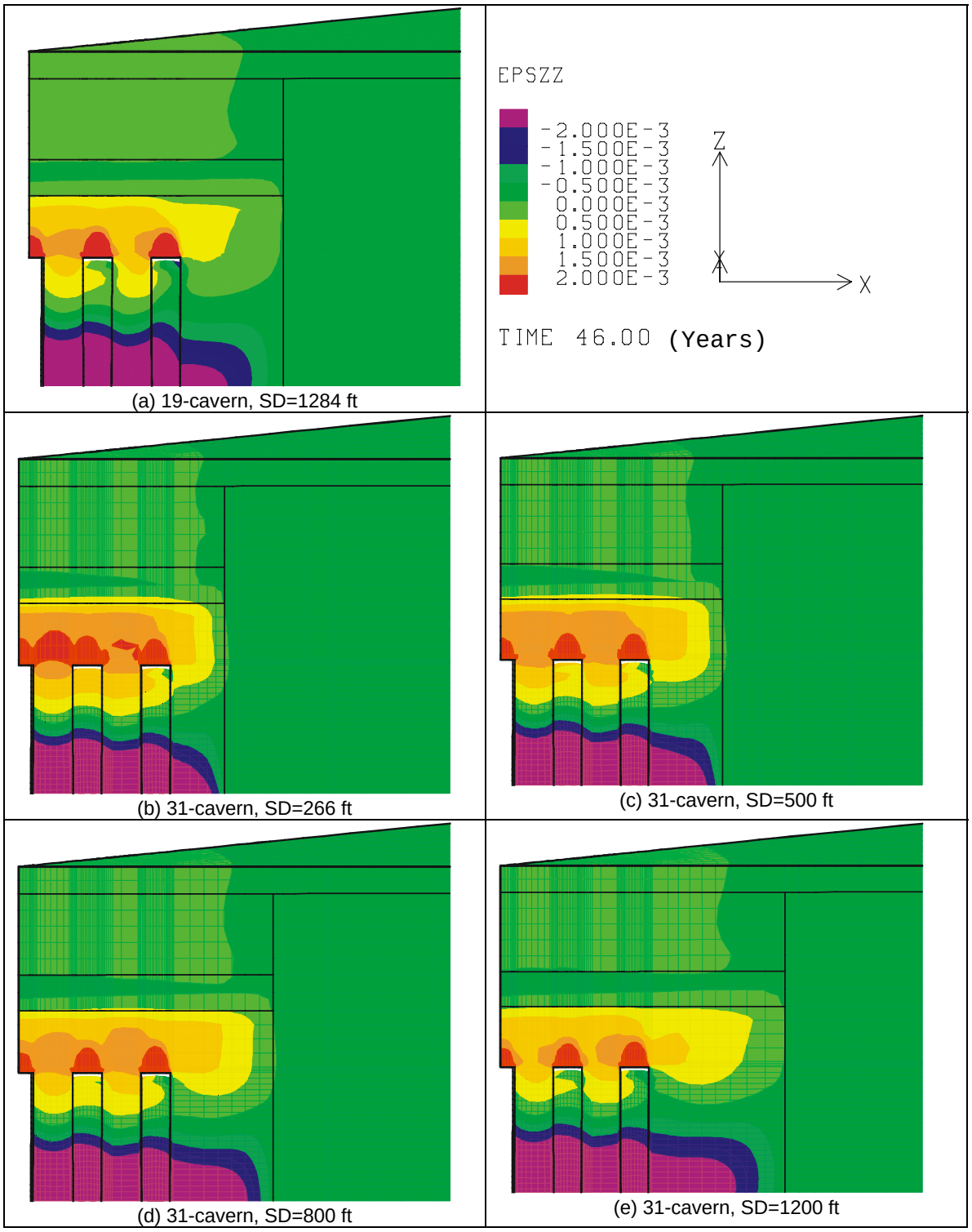

(a) 19-cavern, SD=1284 ft

(b) 31-cavern, SD=266 ft

(c) 31-cavern, SD=500 ft

(d) 31-cavern, SD=800 ft

(e) 31-cavern, SD=1200 ft

Figure 56: Vertical ground strains near cavern wells after 5th leaching with SD

9.6 Standoff Distance Effect on Cavern Stability

9.6.1 Minimum compressive stress

Figure 57 shows the minimum compressive stress as a function of time with various SDs. The minimum compressive stresses are approximately 5 MPa for all cases. The caverns are, therefore, stable against tensile failure for all SDs over time. This implies SD has little effect on the formation of tensile stresses. Shorter SDs yield smaller minimum compressive stresses when a workover is not in progress.

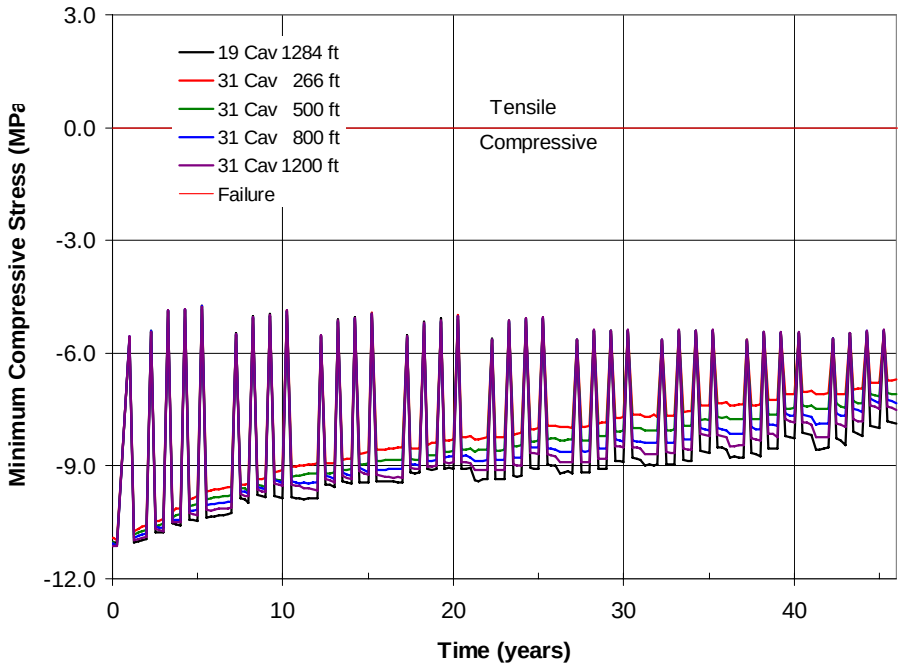

Figure 57: Minimum compressive stress histories with SDs.

9.6.2 Minimum safety factor against dilatant damage

Figure 58 shows the minimum safety factor for dilatancy using the conventional criterion, Equation (7), as a function of time with various SDs. The SD does not affect the dilatancy factor significantly, but a shorter SD tends to make the safety factor lower when a workover is not in progress.

Figure 59 show the minimum safety factor for dilatancy using Lee's criterion, Equation (8), as a function of time with SDs. In a manner similar to the curves by the conventional criterion, the standoff distance does not have much influence on the dilatancy factor, but a shorter SD yields a higher safety factor when a workover is not occurring.

Figure 60 and Figure 61 show the safety factor contours against dilation damage during workover of Cavern 3 for different SDs by the conventional criterion and Lee's criterion,

respectively. Figure 62 shows the safety factor contours against dilatant damage during workover of 5th cavern with SDs by conventional criterion. The section for plan view is cut at the level of the caverns' roofs which is the location of the minimum safety factor as shown in Figure 60. Figure 63 shows the safety factor contours by Lee's criterion. The section is cut at -3,734 ft, which is the level of the minimum safety factor as shown in Figure 61.

As mentioned in Section 8.5.3, the safety factor contour area by Lee's criterion appears broader than that produced by the conventional analysis. In the case of SD is 266 ft, the web between the outmost cavern and the edge of the dome has a relatively low safety factor, which means the salt wall is structurally weaker than at other location. However, the safety factor is beyond both failure criteria. Thus, the caverns should be stable against dilatancy damage.

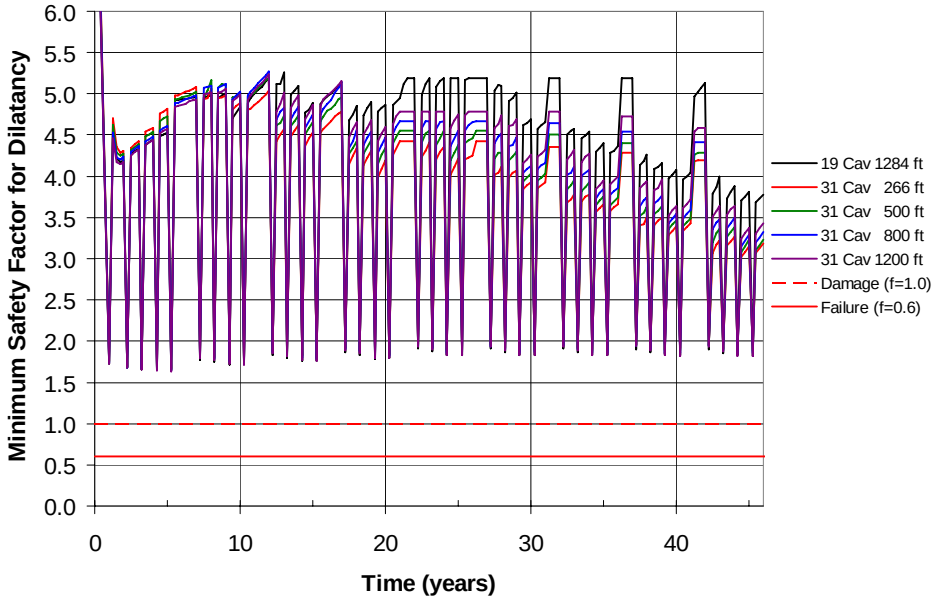

Figure 58: Minimum safety factor histories against dilatant damage with SDs by conventional criterion

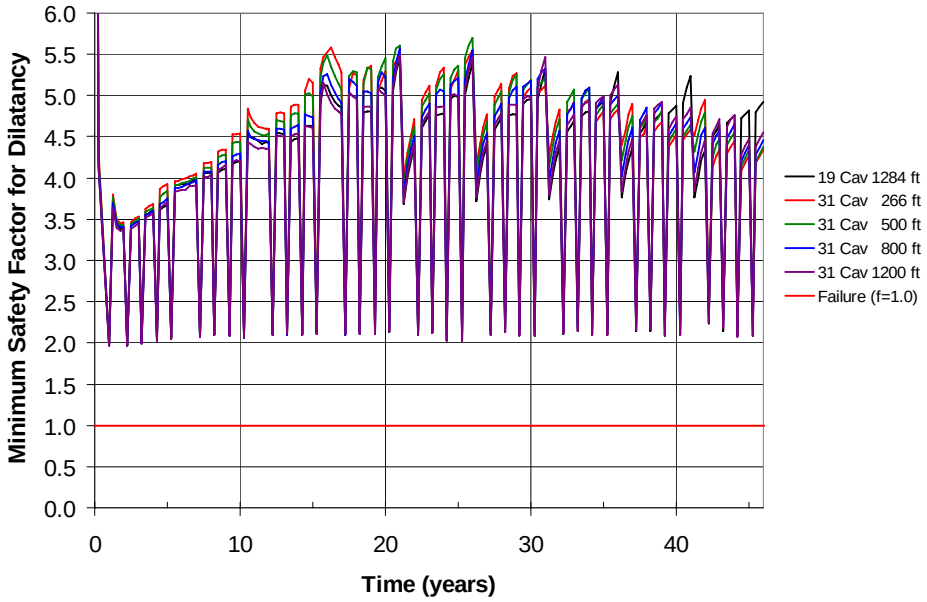

Figure 59: Minimum safety factor histories against dilatant damage with SDs by Lee's criterion

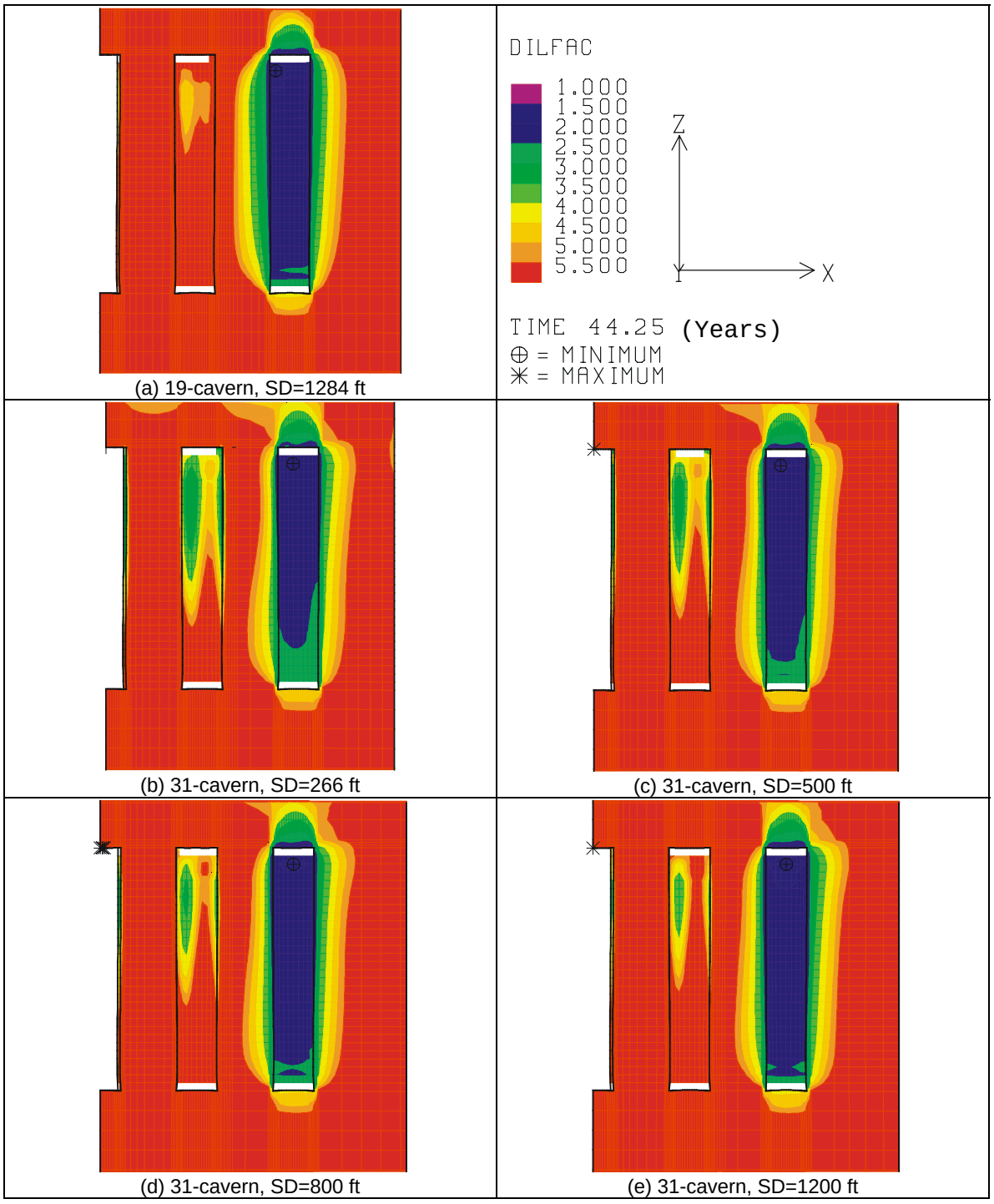

(a) 19-cavern, SD=1284 ft

(b) 31-cavern, SD=266 ft

(c) 31-cavern, SD=500 ft

(d) 31-cavern, SD=800 ft

(e) 31-cavern, SD=1200 ft

Figure 60: Safety factor contours against dilation damage during workover of Cavern 3 with SD by conventional criteria

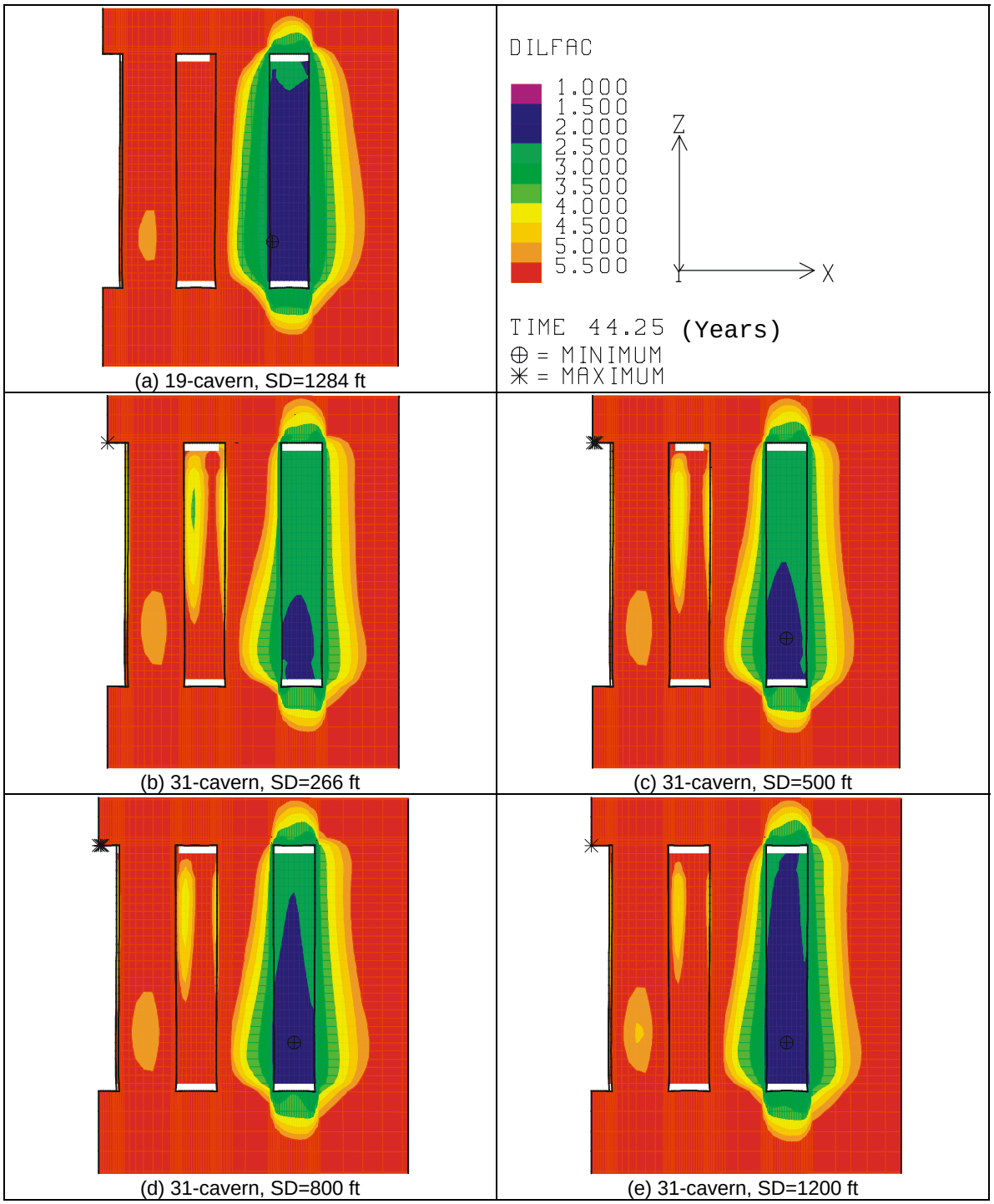

(a) 19-cavern, SD=1284 ft

(b) 31-cavern, SD=266 ft

(c) 31-cavern, SD=500 ft

(d) 31-cavern, SD=800 ft

(e) 31-cavern, SD=1200 ft

Figure 61: Safety factor contours against dilation damage during workover of Cavern 3 with SD by Lee's criteria

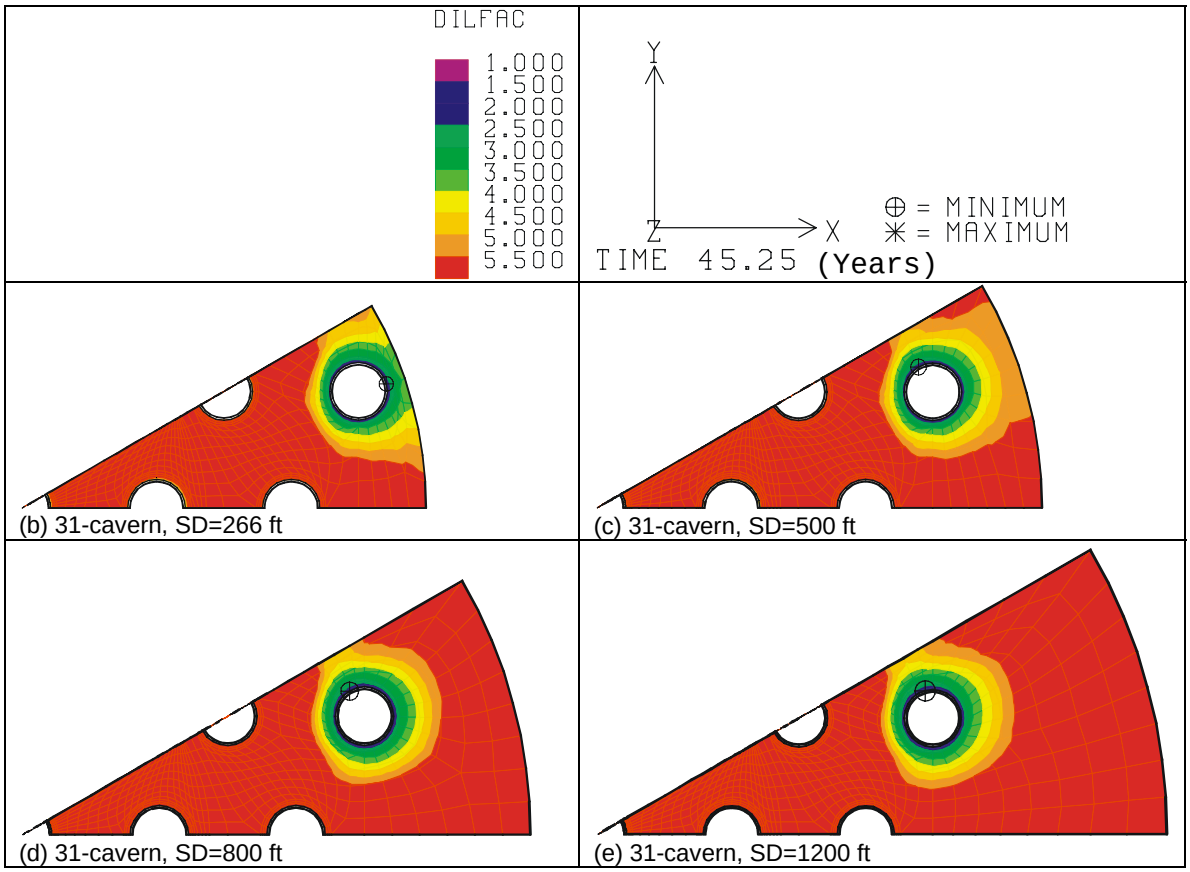

Figure 62: Safety factor contours against dilatant damage during workover of 5th cavern with SD by conventional criterion (Plan view at the level of cavern roof)

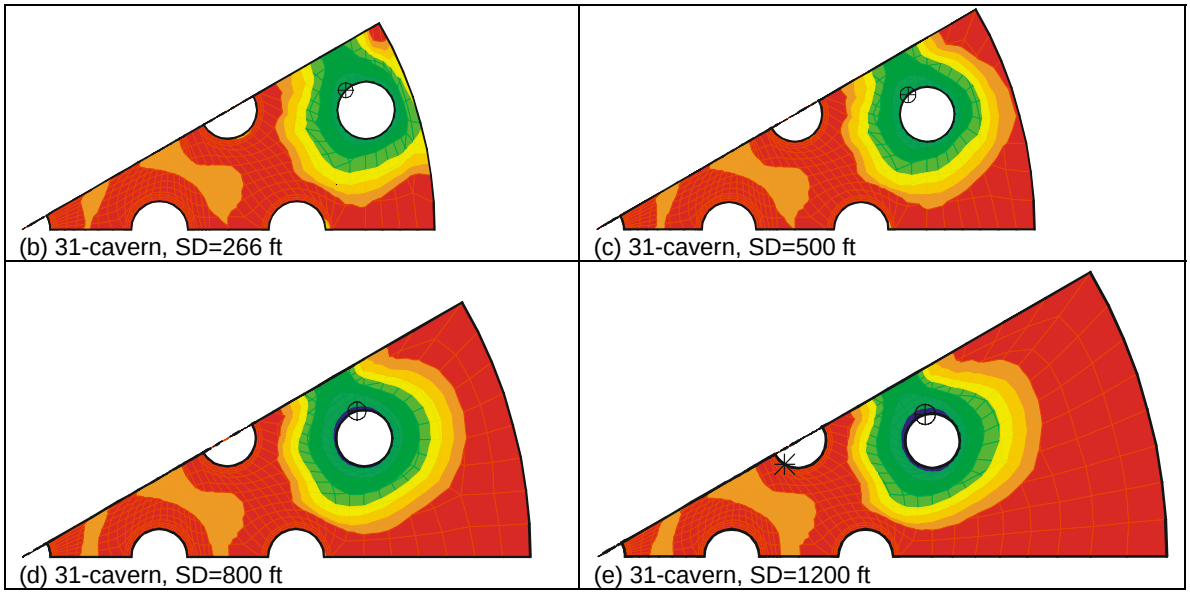

Figure 63: Safety factor contours against dilatant damage during workover of 5th cavern with SD by Lee's criterion (Plan view at the level of minimum SF, -3734 ft. Contour intervals are the same as Figure 62)

10 DISCUSSION AND CONCLUDING REMARKS

The construction of more caverns in a field increases the amount of salt mined from a dome and changes the stress distribution to some degree, particularly for caverns placed close to the edge of the dome. The analyses conducted in this report were able to estimate the impact of adding new caverns to the existing Big Hill cavern field and evaluate the mechanical integrity of the remaining web of salt between the edge of the cavern field and the dome edge. The analyses included the recently derived dilatancy criterion obtained from testing of Big Hill salt core.

The results show that from a structural view point, many additional caverns can be safely added to Big Hill. Models containing 19 and 31 caverns, with encroachments as close as 266 ft as measured from the center of the outermost cavern to the dome edge were considered. In all cases, the caverns were found to be structurally stable. The large caprock at Big Hill mitigated the predicted subsidence rates and damage to surface structures is not expected to occur.

11 REFERENCES

Ballard, S. and Ehgartner, B.L., 2000, *CAVEMAN Version 3.0: System for SPR Cavern Pressure Analysis,* SAND2000-1751, Sandia National Laboratories, Albuquerque, NM 87185-0750.

Blandford, M.L., 1988. JAS3D- A Multi-Strategy Iterative Code for Solid Mechanics Analysis: User's Instructions, Release 1.6, Sandia National Laboratories, Albuquerque, New Mexico.

Butcher, B.M. 1997, *A Summary of the Sources of Input Parameter Values for the WIPP Final Porosity Surface Calculations,* SAND97-0796, Albuquerque, NM: Sandia National Laboratories.

Carmichael, R.S., 1984. *CRC handbook of Physical Properties of Rocks,* CRC (Chemical Rubber Company) Press, Inc. Boca Raton, Fl.

Ehgartner, B.L., 2004a, *Cavern Diameters,* E-mail to B.Y. Park, Sandia National Laboratories, Carlsbad, NM, dated June 29, 2004.

Ehgartner, B.L., 2004b, *Model Pressure,* E-mail to B.Y. Park, Sandia National Laboratories, Carlsbad, NM, dated July 8, 2004.

Ehgartner, B.L., 2004c, *Subsidence Data,* E-mail to B.Y. Park, Sandia National Laboratories, Carlsbad, NM, dated July 8, 2004.

Ehgartner, B.L., 2004d, *Cavern Volume,* E-mail to B.Y. Park, Sandia National Laboratories, Carlsbad, NM, dated August 9, 2004.

Ehgartner, B.L. and Bauer, S., 2004, *Large Scale Salt Deformation: Comments on Subsidence using thermal, creep and Dissolution modeling to assess volumetric strain,* SAND2004-0095C, Sandia National Laboratories, Albuquerque, NM 87185.

Ehgartner, B.L. and Sobolik, S.R., 2002. *3-D cavern Enlargement Analyses,* SAND2002-0526, Sandia National Laboratories, Albuquerque, NM 87185-0706.

Fung, Y.C., 1965, *Foundations of Solid Mechanics,* Englewood Cliffs: NJ. Prentice Hall Inc.

Hart, R.J., T.S. Ortiz, and T.R. Magorian, 1981. *Strategic Petroleum Reserve (SPR) Geological Site Characterization Report: Big Hill Salt Dome,* SAND81-1045, Sandia National Laboratories, Albuquerque, NM.

Hoffman, E.L., 1992, *Investigation of Analysis Assumptions for SPR Calculations,* memo to J. K. Linn, Sandia National Laboratories, Albuquerque, New Mexico, February 7, 1992.

Hoffman, E.L. and Ehgartner, B.L., 1992, *Evaluating the Effects of the Number of Caverns on the Performance of Underground Oil Storage Facilities*, SAND92-2183C, Sandia National Laboratories, Albuquerque, New Mexico.

Hunsche, U.E., 1992. *Failure Behavior of Rock Salt Around Underground Cavities*, 7th International Symposium on Salt.

Krieg, R.D., 1984, *Reference Stratigraphy and Rock Properties for the Waste Isolation Pilot Plant (WIPP) Project*, SAND83-1908, Sandia National Laboratories, Albuquerque, NM 87185.

Lama, R.D. and V.S. Vutukuri, 1978, *Handbook on Mechanical Properties of Rocks – Testing Techniques and Results*, Series on Rock and Soil Mechanics, Vol. 3, No.2, Trans Tech Publications.

Lee, M.Y., Ehgartner, B.L., and Bronowski, D.R., 2004, Laboratory Evaluation of Damage Criteria and Permeability of Big Hill Salt, SAND2004-6004, Sandia National Laboratories, Albuquerque, NM 87185.

Magorian, T.R., and Krieg, R.D., 1990. Investigation of an Empirical Creep Law for Rock Salt that Uses Reduced Elastic Moduli. Rroc. 31st U.S. Sumposum on Rock Mechanics, June 18-20, 1990.

Magorian, T.R, and Neal, J.T., 1988. *Strategic Petroleum Reserve (SPR) Addition Geological Site Characterization Studies Big Hill Salt Dome, Texas*, SAND88-2267**,** Albuquerque, NM: Sandia National Laboratories.

McHenry, J., G. Osborne, and J. Farquhar, 2003. *Quarterly Cavern Integrity and Brine Disposal Well Report*, Period ending September 30, 2003.

Munson, D.E., 1998. *Analysis of Multistage and Other Creep Data for Domal Salts*, SAND98-2276**,** Albuquerque, NM: Sandia National Laboratories.

Munson, D.E., 2004, *Opinion on using E/12.5*, Memo to B.L. Ehgartner, Sandia National Laboratories, Albuquerque, NM, dated June 28, 2004.

Peng, S.S., 1985. *Coal Mine Ground Control*, 2nd Ed., John Wiley and Sons, New York NY.

Neal, J.T., T.R Magorian, W.J. Autin, R. P. McCulloh, S. Denzler, and K.O. Byrne, 1993, *Anomalous Zones in Gulf Coast Salt Domes with Special Reference to Big Hill*, TX, and Weeks Island, LA, SAND92-2283, Sandia National Laboratories, Albuquerque, NM.

Rautman, C., and Ehgartner, B.L., 2004. *Pillar to Diameter Ratios for Big Hill*, Letter from C. Rautman and B. Ehgartner to R.E. Myers, DOE SPR PMO dated February 23, 2004.

Rautman, C., et al., 2005. *An Updated Three-Dimensional Site Characterization Model of the Big Hill Strategic Petroleum Reserve Site, Texas*, Sandia National Laboratories, Albuquerque, NM, Draft of SAND report dated January 5, 2005.

Speirs, C.J., C. J. Peach, R.H. Brzesowsky, P.M.T.M. Schutjens, J. L. Liezenberg, and H.J. Zwart, 1988. *Long Term Rheological and Transport Properties of Dry and Wet Rocks*, EUR 11848, prepared for Commission of the European Communities, by University of Utrecht, Utrecht, The Netherlands.

Stein, J.S. and C.A. Rautman, 2004. *Conversion of the Big Hill Geological Site Characterization Report to a Three-Dimensional Model*, SAND2003-3554, Sandia National Laboratories, Albuquerque, NM.

Tavares, M.P., 1994. Dilatancy *and Failure Criteria for SPR Rock Salt*, Internal Report to J.K. Linn, Sandia National Laboratories, Albuquerque, NM, August 9.

Thorton, C.H. and I.P. Lew, 1983. *Concrete and Design Construction*, Standard Handbook for Civil Engineers, Chapter 8, 3rd ed., F.S. Merritt, editor, McGraw-Hill, NY.

Touloukian, Y.S. and C.Y. Ho, 1981. *Physical Properties of Rocks and Minerals*. McGraw Hill, Vol 2.

Van Sambeek, L., J. Ratigan, and F. Hansen, 1993. *Dilatancy of Rock Salt in Laboratory Tests*, Proc. 34th U.S. Symposium on Rock Mechanics, p.245-248.

Wawersik, W.R. and Zeuch, D.H., 1984, Creep and Creep Modeling of Three Domal Salts – A Comprehensive Update, SAND84-0568, Sandia National Laboratories, Albuquerque, NM.

APPENDIX A: AN EXAMPLE OF FASTQ INPUT FILE

```
TITLE
SPR Big Hill simulations - 19 cavern facility (Distance=1284 ft)

{include("19cav5l_1284.pts")}

nodebc 1 500 4 6 8 10 12 14 16 18 19 20 21 22 23 24 25 26 27 28 29 30 31 32 33 *
    34 36 37 38 39 40 41 42 43 44 45 46 47 48 49 50 51 52
$ nodebc 1 - X-axis boundary of mesh - zero disp. B.C.
nodebc 2   501 5 7 9 11 13 15 17 35 55 56 57 58 59 60 61 62 63 64 65 66 67 68 69 70
$ nodebc 2 - angled boundary of mesh - zero displ. B.C.
nodebc 3   100                 $ Far field boundary of mesh - zero displ. B.C.
poinbc 5   1                   $ Node point BC along well 1 axis
elembc 10  104                 $ Side set BC inside well 1 (center)
elembc 12  106                 $ Side set BC inside well 1 (1st leach)
elembc 13  108                 $ Side set BC inside well 1 (2nd leach)
elembc 14  110                 $ Side set BC inside well 1 (3rd leach)
elembc 15  112                 $ Side set BC inside well 1 (4th leach)
elembc 16  114                 $ Side set BC inside well 1 (5th leach)
elembc 20  127                 $ Side set BC inside well 2 (7-cav sim.)
elembc 22  128                 $ Side set BC inside well 2 (1st leach)
elembc 23  129                 $ Side set BC inside well 2 (2nd leach)
elembc 24  130                 $ Side set BC inside well 2 (3rd leach)
elembc 25  131                 $ Side set BC inside well 2 (4th leach)
elembc 26  132                 $ Side set BC inside well 2 (5th leach)
elembc 30  145                 $ Side set BC inside well 3 (19-cav sim.)
elembc 32  146                 $ Side set BC inside well 3 (1st leach)
elembc 33  147                 $ Side set BC inside well 3 (2nd leach)
elembc 34  148                 $ Side set BC inside well 3 (3rd leach)
elembc 35  149                 $ Side set BC inside well 3 (4th leach)
elembc 36  150                 $ Side set BC inside well 3 (5th leach)
elembc 40  163                 $ Side set BC inside well 4 (19-cav sim.)
elembc 42  164                 $ Side set BC inside well 4 (1st leach)
elembc 43  165                 $ Side set BC inside well 4 (2nd leach)
elembc 44  166                 $ Side set BC inside well 4 (3rd leach)
elembc 45  167                 $ Side set BC inside well 4 (4th leach)
elembc 46  168                 $ Side set BC inside well 4 (5th leach)

$ Well 1 - well material is mat. 11
region  11 11 -1 -500 -104 -501 -3
$ In situ rock near Well 1 (Salt is mat. 1; caprock mat. 2; overburden mat. 3)
region  12 12 -4 -106 -5 -104
region  13 13 -6 -108 -7 -106
region  14 14 -8 -110 -9 -108
region  15 15 -10 -112 -11 -110
region  16 16 -12 -114 -13 -112
region  17 1 -14 -116 -15 -114
$ Well 2
region  21 11 -127 -25 -26
$ In situ rock near Well 2 (Salt is mat. 1; caprock mat. 2; overburden mat. 3)
region  22 12 -24 -127 -27 -128
region  23 13 -23 -128 -28 -129
region  24 14 -22 -129 -29 -130
region  25 15 -21 -130 -30 -131
region  26 16 -20 -131 -31 -132
region  27 1 -19 -132 -32 -133
$ Well 3
region  31 11 -145 -43 -44
$ In situ rock near Well 2 (Salt is mat. 1; caprock mat. 2; overburden mat. 3)
region  32 12 -42 -145 -45 -146
region  33 13 -41 -146 -46 -147
region  34 14 -40 -147 -47 -148
region  35 15 -39 -148 -48 -149
region  36 16 -38 -149 -49 -150
region  37 1 -37 -150 -50 -151
$ Well 4
region  41 11 -163 -61 -62
$ In situ rock near Well 2 (Salt is mat. 1; caprock mat. 2; overburden mat. 3)
region  42 12 -60 -163 -63 -164
region  43 13 -59 -164 -64 -165
region  44 14 -58 -165 -65 -166
region  45 15 -57 -166 -66 -167
region  46 16 -56 -167 -67 -168
region  47 1 -55 -168 -68 -169
$rock out to far field boundary
$region  1  5 -70 -503 -100 -502 -52 -152  $ Rock surrounding Salt Dome mat. 5
region  2  1 -34 -36 -151 -51 -152 -69 -169 -35 -134
```

```
region  3  1 -16 -18 -133 -33 -134 -17 -116

scheme 1 m
scheme 2 u6s $u6s
scheme 3 u6s $u6s
scheme 11 t6s
scheme 12 m
scheme 13 m
scheme 14 m
scheme 15 m
scheme 16 m
scheme 17 m
scheme 21 c6s
scheme 22 m
scheme 23 m
scheme 24 m
scheme 25 m
scheme 26 m
scheme 27 m
scheme 31 c6s
scheme 32 m
scheme 33 m
scheme 34 m
scheme 35 m
scheme 36 m
scheme 37 m
scheme 41 c6s
scheme 42 m
scheme 43 m
scheme 44 m
scheme 45 m
scheme 46 m
scheme 47 m

body 2 3 11 12 13 14 15 16 17 21 22 23 24 25 26 27 31 32 33 34 35 36 37 41 42 43 44 45 46
47
$body 2

exit


$ properties of mesh
$ Wedge angle in degress = {wedge=30.} {th=30*RAD}
$ Far field boundary, m  {rmax=6000}
$ Initial well diameter, m  {d0=67.47}  {r0=d0/2.}
$ Initial well spacing, center-to-center, m {dcen=228.6}
$ Increase volume of well by 16% for each leaching by changing radius
$  {r1=r0*sqrt(1.16)} {r2=r1*sqrt(1.16)} {r3=r2*sqrt(1.16)}
$  {r4=r3*sqrt(1.16)} {r5=r4*sqrt(1.16)} {dr5=r5-r4}
$  {rout=5080.}
$ Distance between Well 3 and the salt dome boundary, m {dis=1284.313*0.3048}
$ Salt Dome Boundary, m {domebc=2.*dcen+dis}


$ Primary boundaries of mesh
point    1    {0.}     {0.}
point    2    {rmax}   {0.}
point    3    {rmax*cos(th)}    {rmax*sin(th)}
point  502    {rout}   {0.}
point  503    {rout*cos(th)}    {rout*sin(th)}
$ Points for initial center cavern
point  500    {r0/6.}  {0.}
point  501    {r0*cos(th)/6.}    {r0*sin(th)/6.}
point    4    {r0}   {0.}
point    5    {r0*cos(th)}    {r0*sin(th)}
point    6    {r1}   {0.}
point    7    {r1*cos(th)}    {r1*sin(th)}
point    8    {r2}   {0.}
point    9    {r2*cos(th)}    {r2*sin(th)}
point   10    {r3}   {0.}
point   11    {r3*cos(th)}    {r3*sin(th)}
point   12    {r4}   {0.}
point   13    {r4*cos(th)}    {r4*sin(th)}
point   14    {r5}   {0.}
point   15    {r5*cos(th)}    {r5*sin(th)}
point   16    {r5+3.*dr5}   {0.}
point   17    {(r5+3.*dr5)*cos(th)}    {(r5+3.*dr5)*sin(th)}
$ Point halfway between well 1 and well 2 (7-cavern well)
point   18    {5.*dcen/9.}     {0.}
$ Points surrounding well 2
point   19    {dcen-r5-3.*dr5}   {0.}
```

```
point   20    {dcen-r5}     {0.}
point   21    {dcen-r4}     {0.}
point   22    {dcen-r3}     {0.}
point   23    {dcen-r2}     {0.}
point   24    {dcen-r1}     {0.}
point   25    {dcen-r0}     {0.}
point   26    {dcen}        {0.}
point   27    {dcen+r0}     {0.}
point   28    {dcen+r1}     {0.}
point   29    {dcen+r2}     {0.}
point   30    {dcen+r3}     {0.}
point   31    {dcen+r4}     {0.}
point   32    {dcen+r5}     {0.}
point   33    {dcen+r5+3.*dr5}  {0.}
point   34    {rr2=dcen+r5+10.*dr5} {0.}

point   35    {rr2*cos(th)} {rr2*sin(th)}
$ Point halfway between well 2 and well 3 (19-cavern well)
point   36    {3.*dcen/2.}     {0.}
$ Points surrounding well 3
point   37    {2.*dcen-r5-3.*dr5}   {0.}
point   38    {2.*dcen-r5}     {0.}
point   39    {2.*dcen-r4}     {0.}
point   40    {2.*dcen-r3}     {0.}
point   41    {2.*dcen-r2}     {0.}
point   42    {2.*dcen-r1}     {0.}
point   43    {2.*dcen-r0}     {0.}
point   44    {2.*dcen}        {0.}
point   45    {2.*dcen+r0}     {0.}
point   46    {2.*dcen+r1}     {0.}
point   47    {2.*dcen+r2}     {0.}
point   48    {2.*dcen+r3}     {0.}
point   49    {2.*dcen+r4}     {0.}
point   50    {2.*dcen+r5}     {0.}
point   51    {2.*dcen+r5+3.*dr5}  {0.}
point   52    {domebc}              {0.}

$ {d19=2.*dcen*cos(th)}
$ Point halfway between well 1 and well 4 (19-cavern well)
point   54    {d19/2.*cos(th)}     {d19/2.*sin(th)}
$ Points surrounding well 4
point   55    {(d19-r5-3.*dr5)*cos(th)}   {(d19-r5-3.*dr5)*sin(th)}
point   56    {(d19-r5)*cos(th)}     {(d19-r5)*sin(th)}
point   57    {(d19-r4)*cos(th)}     {(d19-r4)*sin(th)}
point   58    {(d19-r3)*cos(th)}     {(d19-r3)*sin(th)}
point   59    {(d19-r2)*cos(th)}     {(d19-r2)*sin(th)}
point   60    {(d19-r1)*cos(th)}     {(d19-r1)*sin(th)}
point   61    {(d19-r0)*cos(th)}     {(d19-r0)*sin(th)}
point   62    {(d19)*cos(th)}        {(d19)*sin(th)}
point   63    {(d19+r0)*cos(th)}     {(d19+r0)*sin(th)}
point   64    {(d19+r1)*cos(th)}     {(d19+r1)*sin(th)}
point   65    {(d19+r2)*cos(th)}     {(d19+r2)*sin(th)}
point   66    {(d19+r3)*cos(th)}     {(d19+r3)*sin(th)}
point   67    {(d19+r4)*cos(th)}     {(d19+r4)*sin(th)}
point   68    {(d19+r5)*cos(th)}     {(d19+r5)*sin(th)}
point   69    {(d19+r5+3.*dr5)*cos(th)}  {(d19+r5+3.*dr5)*sin(th)}
point   70    {domebc*cos(th)}       {domebc*sin(th)}


$ Mesh boundaries - x-axis symmetry plane
line   1 str   1 500   0  1 1.0
line 500 str 500   4   0  5 1.0
line   4 str   4   6   0  1 1.0
line   6 str   6   8   0  1 1.0
line   8 str   8  10   0  1 1.0
line  10 str  10  12   0  1 1.0
line  12 str  12  14   0  1 1.0
line  14 str  14  16   0  3 1.0
line  16 str  16  18   0  4 1.2
line  18 str  18  19   0  2 {1./1.2}
line  19 str  19  20   0  3 1.0
line  20 str  20  21   0  1 1.0
line  21 str  21  22   0  1 1.0
line  22 str  22  23   0  1 1.0
line  23 str  23  24   0  1 1.0
line  24 str  24  25   0  1 1.0
line  25 str  25  26   0  6 1.0
line  26 str  26  27   0  6 1.0
line  27 str  27  28   0  1 1.0
line  28 str  28  29   0  1 1.0
```

```
line  29 str  29  30   0  1 1.0
line  30 str  30  31   0  1 1.0
line  31 str  31  32   0  1 1.0
line  32 str  32  33   0  3 1.0
line  33 str  33  34   0  4 1.0
line  34 str  34  36   0  3 1.2
line  36 str  36  37   0  3 {1./1.2}
line  37 str  37  38   0  3 1.0
line  38 str  38  39   0  1 1.0
line  39 str  39  40   0  1 1.0
line  40 str  40  41   0  1 1.0
line  41 str  41  42   0  1 1.0
line  42 str  42  43   0  1 1.0
line  43 str  43  44   0  6 1.0
line  44 str  44  45   0  6 1.0
line  45 str  45  46   0  1 1.0
line  46 str  46  47   0  1 1.0
line  47 str  47  48   0  1 1.0
line  48 str  48  49   0  1 1.0
line  49 str  49  50   0  1 1.0
line  50 str  50  51   0  3 1.0
line  51 str  51  52   0 10 1.0
line  52 str  52 502   0 13 1.2
line 502 str 502   2   0  1  1.0
$ Mesh boundaries - angled symmetry plane
line   3 str   1 501   0  1 1.0
line 501 str 501   5   0  5 1.0
line   5 str   5   7   0  1 1.0
line   7 str   7   9   0  1 1.0
line   9 str   9  11   0  1 1.0
line  11 str  11  13   0  1 1.0
line  13 str  13  15   0  1 1.0
line  15 str  15  17   0  3 1.0
line  17 str  17  35   0 20 0.85
line  35 str  35  55   0  3 1.0
line  55 str  55  56   0  3 1.0
line  56 str  56  57   0  1 1.0
line  57 str  57  58   0  1 1.0
line  58 str  58  59   0  1 1.0
line  59 str  59  60   0  1 1.0
line  60 str  60  61   0  1 1.0
line  61 str  61  62   0  6 1.0
line  62 str  62  63   0  6 1.0
line  63 str  63  64   0  1 1.0
line  64 str  64  65   0  1 1.0
line  65 str  65  66   0  1 1.0
line  66 str  66  67   0  1 1.0
line  67 str  67  68   0  1 1.0
line  68 str  68  69   0  3 1.0
line  69 str  69  70   0 15 0.95
line  70 str  70 503   0 13 1.2
line 503 str 503   3   0  1  1.0
$ Mesh boundaries - far field
$ nth = {nth = 8}   dth = {dth = 1.0}
line  100 circ   2   3  1 {nth} {dth}
line  134 circ  34  35  1 {nth} {dth}
line  152 circ  52  70  1 {nth} {dth}
$Arcs connecting symmetry planes - well 1 region
line  104 circ   4   5  1 {nth} {dth}
line  106 circ   6   7  1 {nth} {dth}
line  108 circ   8   9  1 {nth} {dth}
line  110 circ  10  11  1 {nth} {dth}
line  112 circ  12  13  1 {nth} {dth}
line  114 circ  14  15  1 {nth} {dth}
line  116 circ  16  17  1 {nth} {dth}

$Arcs for the well 2 region
line  133 circ  33  19 26 {1.5*nth} {dth}
line  132 circ  32  20 26 {1.5*nth} {dth}
line  131 circ  31  21 26 {1.5*nth} {dth}
line  130 circ  30  22 26 {1.5*nth} {dth}
line  129 circ  29  23 26 {1.5*nth} {dth}
line  128 circ  28  24 26 {1.5*nth} {dth}
line  127 circ  27  25 26 {1.5*nth} {dth}

$Arcs for the well 3 region
line  151 circ  51  37 44 {1.5*nth} {dth}
line  150 circ  50  38 44 {1.5*nth} {dth}
line  149 circ  49  39 44 {1.5*nth} {dth}
line  148 circ  48  40 44 {1.5*nth} {dth}
line  147 circ  47  41 44 {1.5*nth} {dth}
```

```
line  146 circ  46  42 44 {1.5*nth} {dth}
line  145 circ  45  43 44 {1.5*nth} {dth}

$Arcs for the well 4 region
line  169 circ  55  69 62 {1.5*nth} {dth}
line  168 circ  56  68 62 {1.5*nth} {dth}
line  167 circ  57  67 62 {1.5*nth} {dth}
line  166 circ  58  66 62 {1.5*nth} {dth}
line  165 circ  59  65 62 {1.5*nth} {dth}
line  164 circ  60  64 62 {1.5*nth} {dth}
line  163 circ  61  63 62 {1.5*nth} {dth}
```

APPENDIX B: AN EXAMPLE OF JAS3D INPUT FILE

```
title
SPR Big Hill 19cav5l, (dis=1284ft,WH salt,SF={SFMF=1.5},CE={E2=21e9},SE={E5=70e9},WHP=905psi)

$Material Properties
$Salt (Material 1):
$ Young's Modulus={E1=31.0E9}(Krieg, 1984)
$ Density={rho1=2300.},Poisson's Ratio={nu1=0.25}(Krieg, 1984)
$ Bulk Modulus={K1=E1/(3.*(1.-2.*nu1))},Shear Modulus={mu1=E1/(2.*(1.+nu1))}
$ Creep Constant={A=5.79e-36},Stress Exponent={n=4.9},Thermal Constant={Q=12.0E3}(Krieg,
1984)
$ Salt Reduction Factor={RF=12.5} (Morgan and Krieg, 1988)
$ Structure Factor Multiplication Factor={SFMF}(Adjusted by SF CE SE)
$ Thermal Constant Multiplication Factor={TCMF=0.503}(Ehgartner and Sobolik, 2002)
$Caprock 1 (Material 2):
$ Young's Modulus={E2}(Adjusted by SF CE SE)
$ Density={rho2=2500.},Poisson's Ratio={nu2=0.29}(Hoffman and Ehgartner, 1993)
$Overburden (Material 3):
$ Young's Modulus={E3=0.1E9}(Hoffman and Ehgartner, 1993)
$ Density={rho3=1874.},$ Poisson's Ratio={nu3=0.33}(Hoffman and Ehgartner, 1993)
$Caprock 2 (Material 4):
$ Young's Modulus={E4=75.1E9}(Krieg, 1984)
$ Density={rho4=2300.},Poisson's Ratio={nu4=0.35}(Krieg, 1984)
$ Bulk Modulus={K4=E4/(3.*(1.-2.*nu4))},Shear Modulus={mu4=E4/(2.*(1.+nu4))}
$ Constants: {A0=2.338e6},{A1=2.338},{A2=0.} (Butcher, 1997)
$Surrounding Rock (Material 5):
$ Young's Modulus={E5}(Adjusted by SF CE SE)
$ Density={rho5=2500.},Poisson's Ratio={nu5=0.33}(Lama and Vutukuri, 1978)

$read restart, 0.02
$ {daysec = 86400.} {dayyr=365.}
start time 0.0
  ITERATION PRINT, 20
  MAXIMUM ITERATIONS, 40000
  TARGET TOLERANCE, .00005
  ACCEPTABLE TOLERANCE .00001
$  predictor scale factor, 0.0,0.0
  time steps 1
  PLOT every, 1
  print every, 1
next time {daysec*1.} $ 1 day - transition to freshwater in well
$  predictor scale factor, 1.0,0.0
  time steps 9
  PLOT every, 9
  print every, 9
next time {daysec*10.} $
  time steps 4
  PLOT every, 4
  print every, 1
  write restart every 0
next time {daysec*30.} $
  time steps, 12
  PLOT every, 12
  print every, 12
  write restart every, 0
next time {daysec*90.} $ 90 days
  time steps, 9
  print every, 9
  PLOT every, 9
  write restart every, 0
next time {daysec*dayyr} $ 1 year - change to oil/brine in well
  time steps 540
  write restart every, 0
  PLOT every, 3
  print every, 30
end time  {daysec*dayyr*46.} $ 46 years - all of this to setup up initial
$                               stress/strain state

thermal stress external, tmpnod
plot state, EqCS, temp
plot nodal, displacement, tmpnod
plot element, sig, vonmis, eps, pressure

NO DISPLACEMENT Z 4 $ bottom of mesh
no displacement x 3 $ far-field boundary
no displacement y 3 $ far-field boundary
no displacement x 5 $ vertical axis at origin (well 1)
no displacement y 5 $ vertical axis at origin (well 1)
no displacement y 1 $ x-axis boundary of mesh
```

```
prescribed displacement normal, 2, 1, 0.0, 0,0,0, {-sin(30*RAD)},{cos(30*RAD)},0 $ wedge
boundary of mesh

$ These pressures are from the Hoffman-Ehgartner SPR report
$pressure 7 2 1.e3   $ atmospheric pressure on surface
$ Pressures 10, 20, 30, & 40 are for the initial well pressure
pressure 10 user 1. $ pressure in well 1
pressure 20 user 1. $ pressure in well 2
pressure 30 user 1. $ pressure in well 3
pressure 40 user 1. $ pressure in well 4

$ Pressures 12, 22, 32, & 42 are the pressures after the 1st drawdown
pressure 12 user 1. $ pressure in well 1
pressure 22 user 1. $ pressure in well 2
pressure 32 user 1. $ pressure in well 3
pressure 42 user 1. $ pressure in well 4

$ Pressures 13, 23, 33, & 43 are the pressures after the 2nd drawdown
pressure 13 user 1. $ pressure in well 1
pressure 23 user 1. $ pressure in well 2
pressure 33 user 1. $ pressure in well 3
pressure 43 user 1. $ pressure in well 4

$ Pressures 14, 24, 34, & 44 are the pressures after the 3rd drawdown
pressure 14 user 1. $ pressure in well 1
pressure 24 user 1. $ pressure in well 2
pressure 34 user 1. $ pressure in well 3
pressure 44 user 1. $ pressure in well 4

$ Pressures 15, 25, 35, & 45 are the pressures after the 4th drawdown
pressure 15 user 1. $ pressure in well 1
pressure 25 user 1. $ pressure in well 2
pressure 35 user 1. $ pressure in well 3
pressure 45 user 1. $ pressure in well 4

$ Pressures 16, 26, 36, & 46 are the pressures after the 5th drawdown
pressure 16 user 1. $ pressure in well 1
pressure 26 user 1. $ pressure in well 2
pressure 36 user 1. $ pressure in well 3
pressure 46 user 1. $ pressure in well 4


function 1 $ normal displacement function
0.0 1.0
1.e30 1.0
end

function 2 $ pressure function
0.0 0.0
100. 1.0
1.e30 1.0
end

gravity
  gravitational constant = 9.81
  direction 0. 0. -1.
end gravity

material 1, power law creep, {rho1}    $ Salt, West Hackberry
 bulk modulus = {K1/RF}
 two mu = {2*mu1/RF}
 creep constant = {SFMF*A}
 stress exponent = {n}
 thermal constant = {TCMF*Q}
END
$ {thick1=4400.*.3048}

active limits, 11, 0.0,0.01   $ Initial leaching of cavern
material 11, power law creep, {rho1} $ Salt
 bulk modulus = {K1/RF}
 two mu = {2*mu1/RF}
 creep constant = {SFMF*A}
 stress exponent = {n}
 thermal constant = {TCMF*Q}
END

active limits, 12, 0.0,{daysec*dayyr*21.}    $ First drawdown at 20 years
material 12, power law creep, {rho1} $ Salt
 bulk modulus = {K1/RF}
 two mu = {2*mu1/RF}
 creep constant = {SFMF*A}
```

```
 stress exponent = {n}
 thermal constant = {TCMF*Q}
END

active limits, 13, 0.0,{daysec*dayyr*26.}    $ Second drawdown at 25 years
material 13, power law creep, {rho1} $ Salt
 bulk modulus = {K1/RF}
 two mu = {2*mu1/RF}
 creep constant = {SFMF*A}
 stress exponent = {n}
 thermal constant = {TCMF*Q}
END

active limits, 14, 0.0,{daysec*dayyr*31.}    $ Third drawdown at 30 years
material 14, power law creep, {rho1} $ Salt
 bulk modulus = {K1/RF}
 two mu = {2*mu1/RF}
 creep constant = {SFMF*A}
 stress exponent = {n}
 thermal constant = {TCMF*Q}
END

active limits, 15, 0.0,{daysec*dayyr*36.}    $ Fourth drawdown at 35 years
material 15, power law creep, {rho1} $ Salt
 bulk modulus = {K1/RF}
 two mu = {2*mu1/RF}
 creep constant = {SFMF*A}
 stress exponent = {n}
 thermal constant = {TCMF*Q}
END

active limits, 16, 0.0,{daysec*dayyr*41.}    $ Fifth drawdown at 40 years
material 16, power law creep, {rho1} $ Salt
 bulk modulus = {K1/RF}
 two mu = {2*mu1/RF}
 creep constant = {SFMF*A}
 stress exponent = {n}
 thermal constant = {TCMF*Q}
END

material 2, elastic, {rho2}    $ Caprock 1 (Gypsum and Limestone)
 youngs modulus = {E2}
 poissons ratio = {nu2}
end
$ {thick2=900.*.3048}

material 3, elastic, {rho3}    $ Overburden (sand)
$ Rock properties taken from Hoffman and Ehgartner, 1993
 youngs modulus = {E3}
 poissons ratio = {nu3}
end
$ {thick3=300.*.3048}

material 4, SOIL N FOAMS, {rho4} $ Caprock 2 (ANHYDRITE)
TWO MU = {2.*mu4}
BULK MODULUS = {K4}
A0 = {A0}
A1 = {A1}
A2 = {A2}
PRESSURE CUTOFF = 0.0
FUNCTION ID = 0
end
$ {thick4=400.*.3048}

material 5, elastic, {rho5}    $ Rock surrounding salt dome (sandstone)
 youngs modulus = {E5}
 poissons ratio = {nu5}
end
$ {thick5= 5700.*.3048}

initial value USIGZZ=Function Z 3, 1., material 3
initial value USIGXX=Function Z 3, {nu3/(1.-nu3)}, material 3
initial value USIGYY=Function Z 3, {nu3/(1.-nu3)}, material 3
initial value USIGZZ=Function Z 4, 1., material 2
initial value USIGXX=Function Z 4, {nu2/(1.-nu2)}, material 2
initial value USIGYY=Function Z 4, {nu2/(1.-nu2)}, material 2
initial value USIGZZ=Function Z 7, 1., material 4
initial value USIGXX=Function Z 7, {nu4/(1.-nu4)}, material 4
initial value USIGYY=Function Z 7, {nu4/(1.-nu4)}, material 4
initial value USIGZZ=Function Z 6, 1., material 5
initial value USIGXX=Function Z 6, {nu5/(1.-nu5)}, material 5
```

```
initial value USIGYY=Function Z 6, {nu5/(1.-nu5)}, material 5
initial value USIGZZ=Function Z 5, 1., material 1
initial value USIGXX=Function Z 5, 1., material 1
initial value USIGYY=Function Z 5, 1., material 1
initial value USIGZZ=Function Z 5, 1., material 11
initial value USIGXX=Function Z 5, 1., material 11
initial value USIGYY=Function Z 5, 1., material 11
initial value USIGZZ=Function Z 5, 1., material 12
initial value USIGXX=Function Z 5, 1., material 12
initial value USIGYY=Function Z 5, 1., material 12
initial value USIGZZ=Function Z 5, 1., material 13
initial value USIGXX=Function Z 5, 1., material 13
initial value USIGYY=Function Z 5, 1., material 13
initial value USIGZZ=Function Z 5, 1., material 14
initial value USIGXX=Function Z 5, 1., material 14
initial value USIGYY=Function Z 5, 1., material 14
initial value USIGZZ=Function Z 5, 1., material 15
initial value USIGXX=Function Z 5, 1., material 15
initial value USIGYY=Function Z 5, 1., material 15
initial value USIGZZ=Function Z 5, 1., material 16
initial value USIGXX=Function Z 5, 1., material 16
initial value USIGYY=Function Z 5, 1., material 16

function 3 polynomial $ initial stress function for overburden (mat. 3)
  {a0_3=0.} $ a0
  {a1_3=rho3*9.81} $a1
end

function 4 polynomial $ initial stress function for caprock 1 (mat. 2)
  {a0_2=rho2*9.81*thick3-a1_3*thick3}         $a0
  {a1_2=rho2*9.81}    $a1
end

function 7 polynomial $ initial stress function for caprock 2 (mat. 4)
  {a0_4=rho4*9.81*(thick3+thick2)-a1_3*thick3-a1_2*thick2}         $a0
  {a1_4=rho4*9.81}    $a1
end

function 5 polynomial $ initial stress function for salt (mat. 1, 11~16)
  {a0_1=rho1*9.81*(thick2+thick3+thick4)-a1_2*thick2-a1_3*thick3-a1_4*thick4} $a0
  {a1_1=rho1*9.81}    $a1
end

function 6 polynomial $ initial stress function for rock surrounding dome (mat. 5)
  {a0_6=rho5*9.81*thick3-a1_3*thick3}         $a0
  {a1_6=rho5*9.81}    $a1
end


exit
```

APPENDIX C: AN EAXMPLE OF USER SUBROUTINES

```
C $Id: usrpbc.f,v 5.0 1998/08/07 21:42:02 mlblanf Exp $
      SUBROUTINE USRPBC( FAC,CORDES,KSFLG,SCALE,NE,TIME,NESNS,NEBLK,
     *  NSPC )
C
C ***********************************************************************
C
C   DESCRIPTION:
C     This routine provides pressure boundary conditions to JAS3D
C
C   FORMAL PARAMETERS:
C     FAC      REAL        Array which must be returned
C                          with the required face pressure
C     CORDES   REAL        Nodal coordinate array
C     KSFLG    INTEGER     Side set ID for this pressure BC
C     SCALE    REAL        Pressure scale factor from input record
C     NE       INTEGER     Number of faces having this pressure BC
C     TIME     REAL        Problem time
C     NESNS    INTEGER     Number of Element Side Nodes
C     NEBLK    INTEGER     Number of Elements per Vector Block
C     NSPC     INTEGER     Number of Spatial Coordinate Components
C
C   CALLED BY: EXLOAD, called once per iteration for each user-defined
C                      pressure BC
C
C ***********************************************************************
C
      INCLUDE 'precision.blk'
      INCLUDE 'rcdata.blk'
      INCLUDE 'numbers.blk'
C
C declare logical variables for drawdown flags
C
      LOGICAL FINIT,F1ST,F2ND,F3RD,F4TH,F5TH,WO1,WO2,WO3,WO4
C
      DIMENSION FAC(NEBLK),CORDES(NESNS,NEBLK,NSPC)

C
C initialize the drawdown flags
C
      FINIT = .FALSE.
      F1ST  = .FALSE.
      F2ND  = .FALSE.
      F3RD  = .FALSE.
      F4TH  = .FALSE.
      F5TH  = .FALSE.
      WO1   = .FALSE.
      WO2   = .FALSE.
      WO3   = .FALSE.
      WO4   = .FALSE.
c
c --- for this simulation, the well is formed from 0 to 1 year using freshwater,
c --- translating linearly in time from lithostatic pressure with salt to
c --- hydrostatic pressure with water. Then from 1 year to 31 years, the
c --- oil/brine setup is held in place using the corresponding hydrostatic
c --- pressure
c
c rho-g factors for oil, fresh water, brine in Pa/m
c  in psi/ft, brine=0.52, oil=0.37, fresh water=0.43
c  convert with 1psi=6894.757 Pa, 1 ft=.3048 m
      RGOIL=8369.62
      RGH2O=9726.86
      RGBRINE=11762.7
      RGSALT=22563.
      RGOVR=18383.94
      RGCAP1=24525.
      RGCAP2=22563.
c z-locations for layer interfaces, cavern ceiling and floor, m
      ZSURF=0.
      ZOVR=-300.*.3048
      ZCAP1=-1200.*.3048
      ZCAP2=-1600.*.3048
      ZCEIL=-2286.*.3048
      ZFLOOR=-4176.*.3048
c positive pressure on brine line to maintain well integrity, in Pa
c use estimate of 300 psi
C      PBRINE=300.*6894.757
```

```
c      PBRINE=0.
c Use a well head pressure of 905 psi.  BE 7.8.2004
       PHEAD=905.0*6894.757
C      PHEAD  = (RGBRINE-RGOIL)*(ZSURF-ZFLOOR)+PBRINE
C other important constants
       SECDAY=86400.
       DAYYR=365.
       SECYR=SECDAY*DAYYR
       DEADLOAD=RGOVR*(ZSURF-ZOVR)+RGCAP1*(ZOVR-ZCAP1)
      * +RGCAP2*(ZCAP1-ZCAP2)
       TIMEYR=TIME/SECYR
       A1=AINT(TIMEYR)
       A2=AINT(A1/5.)
       A3=A2*5.+1.
       A4=TIMEYR-A3
       if (a1.ge.5.and.a4.le.0.) a4=a4+5.
C
C
       DO 1000 I = 1,NE
C
C Coordinates of the center of the face
C
          XFAC = PFORTH*(CORDES(1,I,1) + CORDES(2,I,1) +
     *                   CORDES(3,I,1) + CORDES(4,I,1))
          YFAC = PFORTH*(CORDES(1,I,2) + CORDES(2,I,2) +
     *                   CORDES(3,I,2) + CORDES(4,I,2))
          ZFAC = PFORTH*(CORDES(1,I,3) + CORDES(2,I,3) +
     *                   CORDES(3,I,3) + CORDES(4,I,3))
c
          PLITHO = DEADLOAD + RGSALT*(ZCAP2-ZFAC)
c Revised pressure calculation of leach water and oil.  RPJ 10.26.2000
          PH2OPH = RGH2O*(ZSURF-ZFAC)
          POBPH  = RGOIL*(ZSURF-ZFAC)+PHEAD
c
          IF (TIME.LE.(SECYR+SECDAY)) THEN
            PWELL=(PH2OPH-PLITHO)*TIME/SECYR + PLITHO
          ELSE
            PWELL=POBPH
          ENDIF
C
C determine which drawdown the simulation is at
C (modified for adding 5th well by B.Y.Park at 5/22/2004)
C
       IF ((KSFLG.EQ.10) .OR. (KSFLG.EQ.20) .OR. (KSFLG.EQ.30) .OR.
      *                       (KSFLG.EQ.40) .oR. (KSFLG.EQ.50)) THEN
         FINIT = .TRUE.
       ELSEIF ((KSFLG.EQ.12) .OR. (KSFLG.EQ.22) .OR. (KSFLG.EQ.32)
      *                      .OR. (KSFLG.EQ.42) .oR. (KSFLG.EQ.52)) THEN
         F1ST = .TRUE.
       ELSEIF ((KSFLG.EQ.13) .OR. (KSFLG.EQ.23) .OR. (KSFLG.EQ.33)
      *                      .OR. (KSFLG.EQ.43) .oR. (KSFLG.EQ.53)) THEN
         F2ND = .TRUE.
       ELSEIF ((KSFLG.EQ.14) .OR. (KSFLG.EQ.24) .OR. (KSFLG.EQ.34)
      *                      .OR. (KSFLG.EQ.44) .oR. (KSFLG.EQ.54)) THEN
         F3RD = .TRUE.
       ELSEIF ((KSFLG.EQ.15) .OR. (KSFLG.EQ.25) .OR. (KSFLG.EQ.35)
      *                      .OR. (KSFLG.EQ.45) .oR. (KSFLG.EQ.55)) THEN
         F4TH = .TRUE.
       ELSEIF ((KSFLG.EQ.16) .OR. (KSFLG.EQ.26) .OR. (KSFLG.EQ.36)
      *                      .OR. (KSFLG.EQ.46) .oR. (KSFLG.EQ.56)) THEN
         F5TH = .TRUE.
       ENDIF
c
c  determine if well is down for workover (zero pressure for 3 months)
c  Well 1 is regarded as 1st ring, well 2 is regarded as 2nd ring
C
       S1=SCALE
       IF (TIME.GT.(SECYR+SECDAY)) THEN
       IF ((A4.GE.1.0001.AND.A4.LE.1.2501).AND.
      1    (KSFLG.GE.10.AND.KSFLG.LE.19))  PWELL=PWELL-PHEAD
       IF ((A4.GE.2.0001.AND.A4.LE.2.2501).AND.
      1    (KSFLG.GE.20.AND.KSFLG.LE.29))  PWELL=PWELL-PHEAD
C modifid by B.Y.Park at 11/29/04
C Well 3 and well 4 are regarded as 3rd ring
       IF ((A4.GE.3.0001.AND.A4.LE.3.2501).AND.
      1    (KSFLG.GE.30.AND.KSFLG.LE.39))  PWELL=PWELL-PHEAD
       IF ((A4.GE.3.0001.AND.A4.LE.3.2501).AND.
      1    (KSFLG.GE.40.AND.KSFLG.LE.49))  PWELL=PWELL-PHEAD
C add 5/22/2004 by B.Y.Park: Well 5 are regarded as 4th ring
       IF ((A4.GE.4.0001.AND.A4.LE.4.2501).AND.
      1    (KSFLG.GE.50.AND.KSFLG.LE.59))  PWELL=PWELL-PHEAD
```

```
C
      ENDIF
c
      IF (TIME .LE. (SECYR*21.).and.FINIT) THEN
        FAC(I) = S1 * PWELL
      ELSEIF ((TIME.GT.(SECYR*21.).AND.TIME.LE.(SECYR*26.))
     1  .and.F1ST) THEN
        FAC(I) = S1 * PWELL
      ELSEIF ((TIME.GT.(SECYR*26.).AND.TIME.LE.(SECYR*31.))
     1  .and.F2ND) THEN
        FAC(I) = S1 * PWELL
      ELSEIF ((TIME.GT.(SECYR*31.).AND.TIME.LE.(SECYR*36.))
     1  .and.F3RD) THEN
        FAC(I) = S1 * PWELL
      ELSEIF ((TIME.GT.(SECYR*36.).AND.TIME.LE.(SECYR*41.))
     1  .and.F4TH) THEN
        FAC(I) = S1 * PWELL
      ELSEIF ((TIME.GT.(SECYR*41.))
     1  .and.F5TH) THEN
        FAC(I) = S1 * PWELL
      ELSE
        FAC(I) = 0.0
      ENDIF
C
 1000 CONTINUE
c      if (time.ge.t21yr.and.time.le.t215yr)
c     1     write(*,*) phead,plitho,ph2oph,pobph,pwell,fac(ne)
      RETURN
      END
```

APPENDIX D: COMPARISON OF DIFFERENT DAMAGE STRENGTH CRITERIA

$$\sqrt{J_2} = a + b \cdot e^{n \cdot I_1}$$

$x := 0 \cdot psi, 100 psi .. 20000 psi$

$a := 1746 psi$ $\quad a = 1.204 \times 10^{7}\ Pa$

$b := -1320 psi$ $\quad b = -9.101 \times 10^{6}\ Pa$

$n := -0.00034 \frac{1}{psi}$ $\quad n = -4.931 \times 10^{-8} \frac{1}{Pa}$

$f(x) := a + b \cdot e^{n \cdot x}$ (Lee's Failure Criterion of Big Hill Salt)

$g(x) := 0.27x$ (Typical Salt Strength)

$h(x) := 0.417x$ (Failure: SPR rock mechanics test data)

$i(x) := 0.25x$ (Damage: SPR rock mechanics test data)

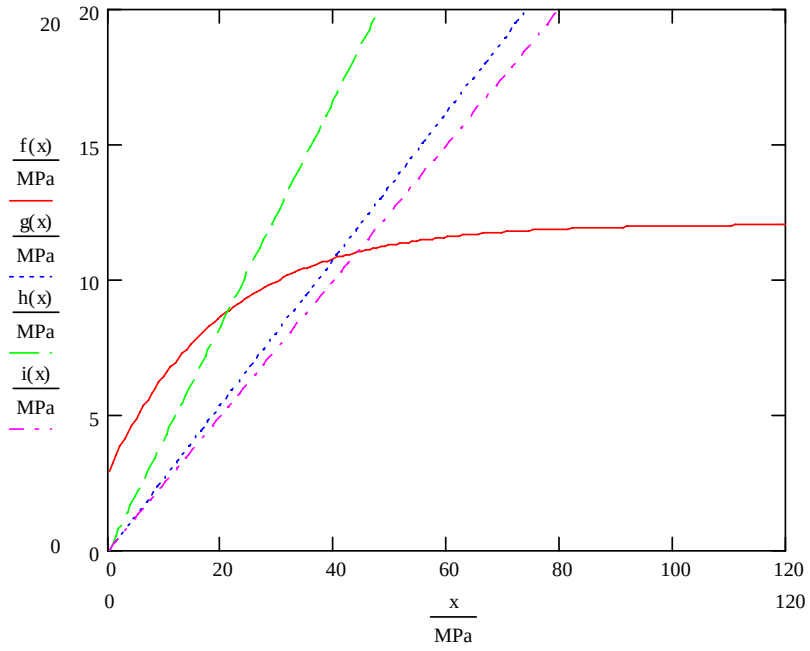

Figure D-1: Comparison of damage strength criteria

APPENDIX E: AN EXAMPLE OF ALGEBRA FILE

```
$
$ Subsidence, Principal Stress and Dilation Criteria
$ coded by B.Y.Park on June 30, 2004
$
ALLTIMES
tmin 86400
save displx disply displz VONMISES status epsxx epsyy epszz sigxx sigyy sigzz
$
$ Difference from displacement at 1st time step
$ Unit conversion of m to ft
$
dx=(displx-displx:1)/0.3048
dy=(disply-disply:1)/0.3048
dz=(displz-displz:1)/0.3048
$
$ Compute Maximum Principal Strain
$
emax=pmax(epsxx,epsyy,epszz,epsxy,epsyz,epszx)
emaxmx=smax(emax)
$
$ Select Salt Dome
$
blocks 1 11 12 13 14 15 16
$
$ Compute Maximum Principal Stresses (Pa)
$
smax=pmax(sigxx,sigyy,sigzz,sigxy,sigyz,sigzx)
smaxmx=smax(smax)
$
$ Compute Sqrt(J2) and I1
$
PRE=-(SIGXX+SIGYY+SIGZZ)/3.0
PRE1=ABS(PRE)-1.0e-6
PRE2=IFGZ(PRE1,PRE1,1.0e-6)
SJ2=VONMISES/SQRT(3.0)
I1=3.*ABS(PRE2)
$
$ Compute Maximum Squr(J2) and I1 (Pa)
$
SJ2MAX=smax(SJ2)
I1MAX=smax(I1)
$
$ Compute Maximum
$ Dilation Criterion (SPR rock mechanics test data)
$
FX=0.25*I1
DPOT=SJ2/FX
CUT=0.01
RATIO=DPOT-CUT
DIL=IFLZ(RATIO,CUT,RATIO+CUT)
DILFAC=1/DIL
mindil=smin(dilfac)
$
$ Dilation Criterion (Lee's test data for Big Hill salt)
$
m1=12.04E6
m2=9.107E6
m3=-0.049344E-6
GX=m1-m2*EXP(m3*I1)
DPOTL=SJ2/GX
RATIOL=DPOTL-CUT
DILL=IFLZ(RATIOL,CUT,RATIOL+CUT)
DILFACL=1/DILL
mindill=smin(DILFACL)
$
maxsj2=smax(sj2)
minfx=smin(fx)
mingx=smin(gx)
$
$ Define time in terms of years
$
TIME=TIME/3.1536e7
$
$ Delete unneeded variables
$
delete PRE PRE1 PRE2 SJ2 I1 RATIO DIL RATIOL DILL FX GX
delete M1 M2 M3 CUT
```

DISTRIBUTION LIST

Federal Agencies

U.S. DOE SPR PMO (8)
900 Commerce Road East
New Orleans, LA 70123
Attn: W.C. Gibson, FE 44
W.S. Elias, FE 4431 (4)
R.E. Myers, FE 4421
TDCS (2)

U.S. Department of Energy
Strategic Petroleum Reserve
1000 Independence Avenue SW
Washington, D.C. 20585
Attn: D. Johnson, FE 421

US Department of Energy
Office of Civilian Radioactive Waste Mgmt.
Forrestal Building
Washington, DC 20585
Attn: Deputy Director, RW-2

DynMcDermott (2)
850 South Clearview Parkway
New Orleans, LA 70123
Attn: J.A. Farquhar, DM 21
J.M. HcHenry, DM 21

Foreign Address

Korea Atomic Energy Research Institute (4)
150 Duckjin-dong, Yusong-ku, Taejon, 305-600,
Republic of KOREA
Attn: Dr. In-Soon Chang
Dr. Hyun-Soo Park
Dr. Pil-Soo Hahn
Dr. Chunsoo Kim

Seoul National University
Department of Nuclear Engineering
Shillim-dong, Kwanak-gu, Seoul, 151-742
Republic of KOREA
Attn: Prof. Chang-Sun Kang

Seoul National University (2)
School of Civil, Urban and Geosystem
Engineering
Shillim-dong, Kwanak-gu, Seoul, 151-742
Republic of KOREA
Attn: Prof. Chung-In Lee
Prof. Myung-Mo Kim

Kyung Hee University
College of Advanced Technology
Dept. of Nuclear Engineering
1, Seochun-Ri, Kihung-Eup, Yongin-City,
Gyeonggi-Do, 449-701,
Republic of KOREA
Attn: Prof. Jooho Whang, Ph.D.

Sandia Internal

MS	Org.	
0701	6100	P. B. Davies
0701	6102	J. A. Merson
0706	6113	D. J. Borns
0706	6113	B. L. Ehgartner (10)
0706	6113	D. L. Lord
0706	6113	D. E. Monson
0706	6113	C. C. Rautman
0706	6113	A. R. Sattler
0735	6115	R. E. Finley
0741	6200	M. L. Tatro
0750	6118	T. E. Hinkebein
0751	6117	L. S. Costin
0751	6117	T. W. Pfeifle
0751	6117	M. Y. Lee (5)
0751	6117	S. R. Sobolik (5)
0771	6800	S. A. Orell
0771	6853	F. D. Hansen
0776	6852	M. K. Knowles
0776	6852	J. S. Stein
1031	6117	D. R. Bronowski
1089	6101	F. B. Nimick
1395	6821	D. S. Kessel
1395	6822	M. J. Rigali
1395	6822	L. H. Brush
1395	6822	C. G. Herrick
1395	6821	B. Y. Park (10)
9018	8945-1	Central Technical Files
0899	9616	Technical Library
0731	6850	823 Library
1395	6820	WIPP Library (2)